Politecnico di Torino

ScuDo
Scuola di Dottorato ~ Doctoral School
WHAT YOU ARE, TAKES YOU FAR

Doctoral Dissertation
Doctoral Program in Metrology (XXXVIII cycle)

Color centers in diamond from single-photon emission to sensing applications

By

Claudia Stella

******

Supervisor(s):
Dr. Paolo Traina
Academic Supervisor: Dr. Marco Genovese

Doctoral Examination Committee:
Prof. Stefano Olivares, Università degli Studi di Milano
Prof. Alberto Bramati, Sorbonne Université
Prof. Sabrina Grassini, Politecnico di Torino
Dr. Alice Meda, Istituto Nazionale di Ricerca Metrologica

Politecnico di Torino
2026

Declaration

I hereby declare that, the contents and organization of this dissertation constitute my own original work and does not compromise in any way the rights of third parties, including those relating to the security of personal data.

Claudia Stella
2026

* This dissertation is presented in partial fulfillment of the requirements for **Ph.D. degree** in the Graduate School of Politecnico di Torino (ScuDo).

I would like to dedicate this thesis to my parents, that support me since day 0

Acknowledgements

I would like to thank all the people who supported me during this PhD journey.

First of all, I'm very grateful to the Quantum Optics Group at the National Institute of Metrological Research (INRiM). Working with this team over the years has been a great opportunity for me to learn, grow, and face many challenges in a supportive and collaborative environment.

A special thank you goes to Dr. Paolo Traina, my supervisor, for guiding me through this work and always being available with advice and encouragement.

I also want to thank Dr. Marco Genovese, Dr. Elena Losero, Dr. Ekaterina Moreva, Dr. Hoda Shirzad, and Dr. Ettore Bernardi for the helpful discussions and ideas.

I'm very thankful to the Neuroscience Group, especially Prof. Valentina Carabelli, Dr. Giulia Tomagra, Dr. Chiara Cambini and Dr. Claudio Franchino for their support in the biological part of this research and for providing the cell samples.

Many thanks also to Klaudia Kvakova and Peter Cigler from the Institute of Organic Chemistry and Biochemistry of the Czech Academy of Sciences for the nanodiamond samples.

I also want to thank all the fellow PhD students I met along the way. Sharing coffee breaks, lunch hours, and even ping pong match made everyday life at the lab lighter and more enjoyable. Those small moments of fun and support meant a lot and created a sense of community I will always remember.

Finally, I want to thank my family and my boyfriend for always being by my side, through both the good times and the difficult ones. Their love, patience, and constant encouragement have been a source of strength throughout this entire journey. They believed in me even when I doubted myself, and their support gave me the motivation to keep going, especially in the most challenging moments. I truly could not have

reached this point without them, and I will always be grateful for their presence in my life.

Abstract

Quantum metrology is one of the foundational element of emerging quantum technologies, playing a central role in applications ranging from secure communication to high-precision sensing. Among these, quantum sensing is rapidly gaining attention due to its ability to exploit quantum coherence and entanglement to achieve sensitivities beyond classical limits. One particularly promising platform for quantum sensing is based on nitrogen-vacancy (NV) centers in diamond, which offer a unique combination of quantum coherence, optical addressability, and biocompatibility. This thesis explores the potential of quantum sensing using NV centers in nanodiamond (ND) for nanoscale thermometry in biological systems with a particular focus on probing temperature at the intracellular level. Understanding temperature dynamics inside living cells is a fundamental challenge in modern biology and medicine, as thermal processes are closely related to cellular functions, metabolic activity, and pathological states. However, conventional thermometry techniques struggle to provide the spatial and temporal resolution needed in such complex environments, such as the single cell interior.

NV centers, exhibit spin-dependent photoluminescence that is sensitive to temperature, even at the nanoscale. By embedding these quantum sensors in NDs, and developing experimental protocols for their optical interrogation, we investigate the feasibility of performing localized temperature measurements in biologically relevant environments.

While significant challenges remain, our work demonstrates key steps toward the realization of intracellular quantum thermometry. In particular, we highlight the robustness and biocompatibility of ND-based sensors, and their potential for mapping thermal variations with high spatial resolution.

Moreover, the prospect of functionalizing NDs to target specific organelles or cellular structures adds an exciting dimension to future developments, potentially

enabling organelle-specific thermometry. Even though this kind of advancement is still a future perspective, these possibilities suggest that quantum sensing tools could be useful in many areas of life sciences, justifying the potential interest in the investigation described in this thesis.

In addition to biological thermometry, this thesis also addresses some other experimental directions. The first concerns the optimization of ND processing through oxidation and irradiation-based treatments, aimed at enhancing the properties of NV ensembles while reducing NDs size. These improvements are essential to increase sensitivity and reduce variability in sensing applications. The second direction focuses on the comparative study of germanium-vacancy (GeV) color centers under different post-annealing conditions. By analyzing the fluorescence lifetime, saturation power, and excitation efficiency of individual GeV emitters, I provide quantitative metrics for assessing their performance as alternative quantum probes. Moreover, Chapter 8 reports on a joint collaboration with the Czech Metrology Institute, presenting the characterization of a custom calibrated detector developed for the mesoscopic regime.

In summary, this thesis reports on my research activity during my PhD at Istituto Nazionale di Ricerca Metrologica (INRiM), ranging from material optimization to integrated bio-sensing applications. The results contribute to the growing intersection between quantum metrology and biophysics, offering practical insights into how diamond-based quantum sensors can be engineered, calibrated, and deployed for probing nanoscale temperature variations in living systems.

Structure and content of the thesis

This thesis moves from the material background to methods, instrumentation, and experiments on quantum thermometry using NV centers in NDs for biological application.

Chapter 1 — Diamond as a platform. The first chapter introduces diamond as a solid-state material suitable for hosting optically active point defects. The discussion begins with its crystal structure and intrinsic properties, including wide band gap, high thermal conductivity, and chemical robustness, which make it an

exceptional host for quantum emitters. The main growth techniques, High Pressure High Temperature (HPHT) and Chemical Vapor Deposition (CVD), are reviewed together with the differences in crystal quality, impurity levels, and resulting color center properties. The chapter concludes with an overview of NDs, discussing how particle size, morphology, and surface chemistry influence photoluminescence stability, charge state conversion, and spin coherence, which are key parameters for sensing.

Chapter 2 — Color centers as single–photon sources. The second chapter places diamond color centers within the framework of quantum optics and single-photon emission. The criteria used to identify single emitters are introduced through the second-order correlation function $g^{(2)}(0)$, and simple rate-equation models are presented to describe the population dynamics of the excited and metastable states. From these models, quantities such as fluorescence lifetime, saturation power, and brightness are extracted. The discussion highlights the link between these optical properties and their relevance for quantum metrology, especially in terms of photon efficiency and spin readout fidelity.

Chapter 3 — NV centers and ODMR. This chapter focuses on the negatively charged NV center, which represents the most established platform for diamond-based quantum sensing. The electronic structure, charge states, and spin Hamiltonian of the NV center are introduced to explain the optical and magnetic interactions governing its behavior. The principles of optically detected magnetic resonance (ODMR) are presented in both continuous-wave and pulsed configurations, along with practical schemes for spin initialization and readout. The dependence of the zero-field splitting on temperature is described, showing how it can be exploited for nanoscale thermometry.

Chapter 4 — Quantum biosensing. The fourth chapter explores the application of quantum sensing in biological systems, with emphasis on thermal and magnetic readout using diamond color centers. The specific advantages of NV-based sensors, such as their optical addressability, room-temperature operation, and biocompatibility, are compared with conventional fluorescence-based probes. The chapter reviews the main advances in intracellular NV thermometry, emphasizing the importance of

calibration, nanoparticle internalization, and the control of excitation power in live samples. It also highlights the current challenges in quantum biosensing, including the trade-off between signal stability, spatial resolution, and measurement invasiveness, outlining the potential of NDs for long-term temperature monitoring in living cells.

Chapter 5 — Experimental setup. Chapter five details the optical and microwave setup used throughout the work. The configuration of the confocal microscope is described, including excitation and collection optics, spectral filters, and single-photon detection modules. The integration of the optical path with a multielectrode array (MEA) platform is presented, enabling simultaneous optical thermometry and electrophysiological recordings on neuronal cultures. The addition of a fast steering mirror (FSM) within a $4f$ relay is explained as a means to achieve real-time tracking and photoluminescence mapping.

Chapters 6/7/8 — Experimental results. These chapters present the main experimental outcomes of the thesis.

Chapter 6 focuses on the optimization of ND sensors through thermal oxidation and proton irradiation, aimed at improving brightness and spin contrast. It also includes the study of GeV centers, where HPHT post-treatment is shown to enhance optical efficiency and reduce saturation power.

Chapter 7 describes the integration of NV thermometry with primary neuronal cultures. The optical path was combined with MEA to enable simultaneous electrical and thermal readout. Extensive viability tests confirmed that none of the experimental variables (laser, microwaves, or ND) alter neuronal firing. A simulated ODMR protocol demonstrated the feasibility of real-time, biocompatible thermometric acquisition under experimental conditions.

Chapter 8 reports on the characterization of a custom calibrated detector, carried out in collaboration with the Czech Metrology Institute. The study details the detector's design, metrological calibration, and performance in the mesoscopic optical regime. Although complementary to the main body of this thesis, this work shows the broader applicability of the developed experimental methods to precision measurement and optical metrology.

Chapter 9 — Conclusions and outlook. The final chapter summarizes the key results obtained in the experimental areas explored in this thesis: ND optimization, GeV emitter engineering, NV-based quantum thermometry in neurons, and characterization of a custom calibrated photodetector. Each section contributes to advancing the applicability of diamond color centers in real-world scenarios, from improving material performance to validating measurement protocols in biological environments.

The chapter also outlines future directions aimed at developing increasingly robust and versatile quantum sensing platforms.

Contents

List of figures

List of tables

List of Abbreviations

INRiM Istituto Nazionale di Ricerca Metrologica

NV Nitrogen–Vacancy

GeV Germanium–Vacancy

SiV Silicon–Vacancy

HPHT High-Pressure High-Temperature

CVD Chemical Vapor Deposition

ND Nanodiamond

MEA Multi-Electrode Array

FSM Fast Steering Mirror

ODMR Optically Detected Magnetic Resonance

FCC Face-Centered Cubic

SPS Single-Photon Source

ZPL Zero-Phonon Line

HBT Hanbury Brown and Twiss

CW Continuous Wave

SPDC Spontaneous Parametric Down-Conversion

QIP Quantum Information Processing

QKD Quantum Key Distribution

QBER Quantum Bit Error Rate

PNS Photon-Number Splitting

SI International System of Units

PL Photoluminescence

ISC Intersystem Crossing

MW Microwave

FWHM Full Width at Half Maximum

SET Single Electron Transistor

AP Action potential

MEG Magnetoencephalography

SPAD Single-Photon Avalanche Diode

PSF Point Spread Function

DLS Dynamic Light Scattering

DRIFT Diffuse Reflectance Infrared Fourier Transform

AFM Atomic Force Microscopy

NA Numerical Aperture

PBS phosphate-buffered saline

DMSO Dimethyl Sulfoxide

TTX Tetrodotoxin

CMI Czech Metrology Institute

SIA switched-integrator amplifier

Chapter 1

Diamond

Diamond [10] is a widely recognized material, admired not only for its brilliance in the jewellery industry, but also for its exceptional physical properties, which make it highly valuable in scientific and technological fields. Composed entirely of carbon atoms, a group IV element known for its abundance and versatility, diamond showcases the remarkable bonding capabilities of carbon.

In this chapter, we will describe diamond in terms of allotropic forms, crystal structure, and physical properties, then we will outline the main production routes and the resulting material classification. The chapter concludes with an introduction to nanodiamonds as a promising platform for quantum sensing applications.

1.1 Allotropic Forms

Carbon's ability to form various types of chemical bonds, both with itself and with other elements, results in several well-defined allotropes, each with distinct structures and interatomic bonding characteristics. In diamonds, each carbon atom is bonded to four others in a tetrahedral arrangement, creating a rigid three-dimensional network that gives the crystal its outstanding hardness. This tetrahedral coordination arises from sp^3 hybridization and a bond angle close to 109.5°, which maximizes packing efficiency and mechanical rigidity.

In contrast, other carbon allotropes like graphite and fullerenes, have each carbon atom bonded to only three others, forming planar structures. Additionally, there are

nanometer-scale cylindrical structures known as carbon nanotubes, which can be visualized as rolled-up sheets of graphene (Fig. 1.1). Lonsdaleite (hexagonal diamond) also exists and shares similar local bonding but a different stacking sequence, leading to distinct mechanical responses under extreme conditions.

As a result of its peculiar crystalline structure, diamond is the most stable allotropic form of carbon.

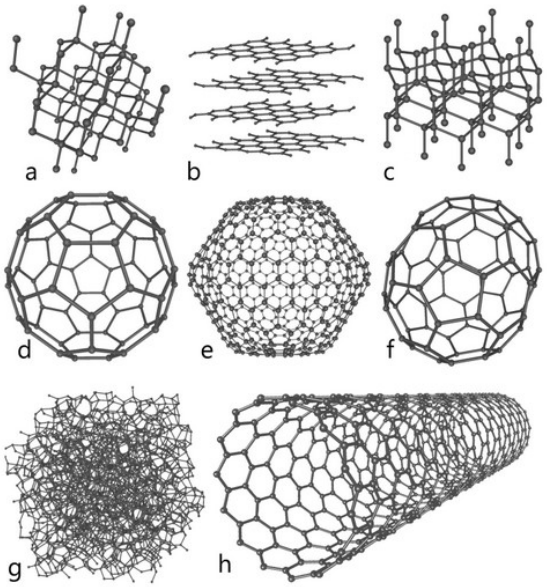

Fig. 1.1 Representation of the different allotropic forms of carbon: (a) diamond, (b) graphite, (c) lonsdaleite, (d) Buckminsterfullerene, (e) C540 fullerene, (f) C70 fullerene, (g) amorphous carbon, and (h) nanotube. The figure [1] illustrates the structural diversity of carbon allotropes and their characteristic bonding geometries.

1.2 Crystal structure

As mentioned, diamond is one of the allotropic forms of carbon, characterized by its tetrahedral coordination of carbon atoms through sp^3 hybridization. This results in a face-centered cubic (FCC) lattice with a two-atom basis. The carbon atoms occupy positions (0, 0, 0) and (¼, ¼, ¼), forming a rigid, three-dimensional crystal structure (Fig. 1.2). The lattice constant is approximately 0.357 nm, while the atomic bond length is about 0.154 nm. The mass density of diamond is 3.54 g/cm^3, and the atomic density reaches 1.77×10^{23} atoms/cm^3. The diamond structure can be viewed as two

interpenetrating FCC sub lattices displaced by $(\frac{1}{4}, \frac{1}{4}, \frac{1}{4})$. Its space group is $Fd\bar{3}m$ (No. 227), with high symmetry that favors the formation of optically active point defects.

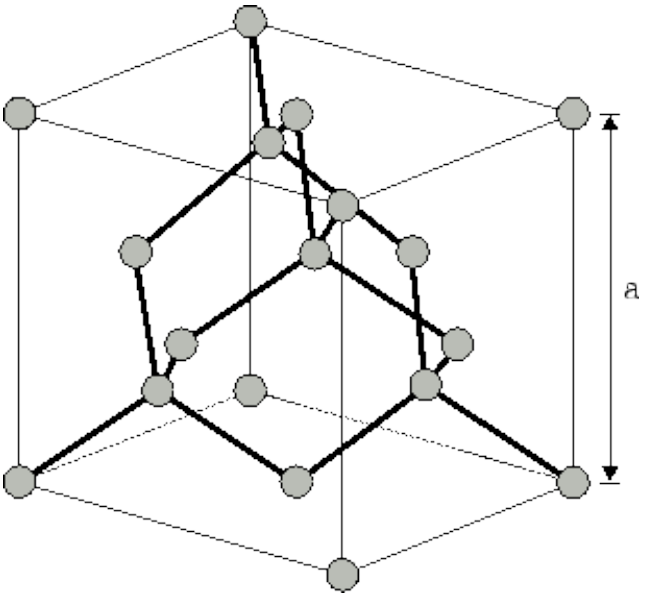

Fig. 1.2 Diamond lattice unit cell. The atomic arrangement highlights the tetrahedral coordination of carbon atoms and the cubic symmetry of the diamond crystal structure.

Thanks to its structure diamond presents exceptional hardness and stability, making it the hardest naturally occurring material. Despite graphite being the thermodynamically favoured phase under standard conditions, as shown in Fig. 1.3, diamond remains metastable due to the significant activation energy (~2 eV) required for conversion to graphite. The metastability is technologically relevant, as it allows diamond to keep its properties at ambient pressure and temperature over geological timescales, while enabling controlled phase engineering only under extreme processing conditions.

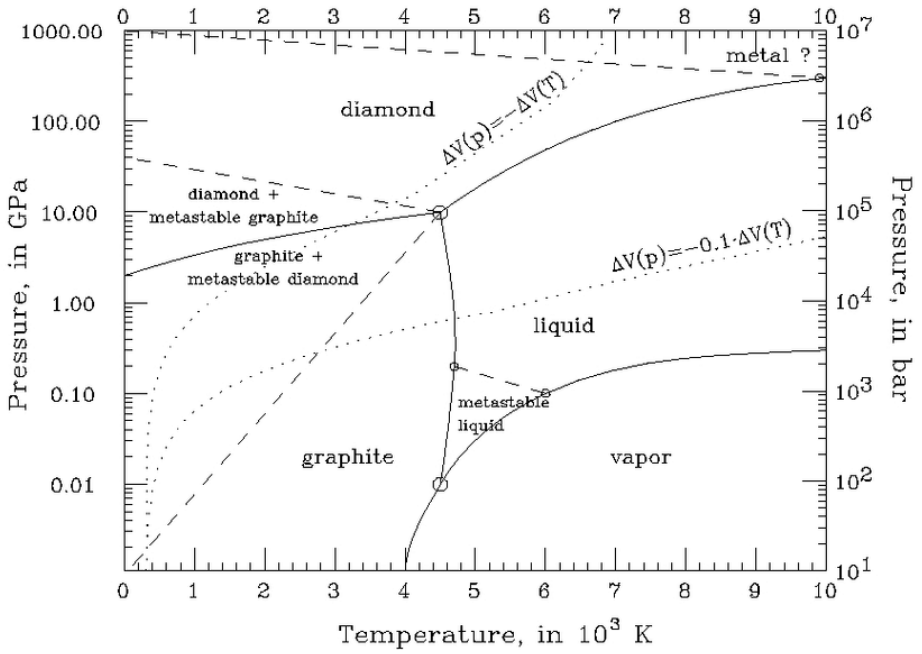

Fig. 1.3 Carbon phase diagram [2]. The diagram shows the stability regions of graphite and diamond as a function of pressure and temperature, illustrating the high-pressure, high-temperature conditions required for diamond formation.

1.3 Advantages of diamond in quantum metrology

In diamond, optically active point defects, known as color centers, create localized electronic states within the wide band gap and, under optical excitation, emit light with stable, well-defined spectra [11, 12]. Thanks to these defects, diamond has proven to be a promising platform for quantum metrology, and in general for quantum technologies, ranging from the implementation of single-photon sources (SPS), emitters that release light one photon at a time, to quantum sensing. In the latter, quantum states in solids, such as the electron spins of point defects, act as local probes that are sensitive to magnetic and electric fields, temperature, and strain.

The following are some of the features justifying the widespread use of diamond in quantum photonics and for quantum metrology in applications ranging from cryogenic to room temperature conditions:

- **Stable emitters.** There are several color centers in diamond that shows little blinking (random intensity interruptions) and bleaching (permanent signal loss), so they provide reliable single-photon emission [12];
- **Room-temperature operation.** The wide band gap (∼5.5 eV) and strong sp^3 bonds isolate defect states and suppress non-radiative losses, enabling bright photoluminescence at ambient conditions;
- Some color centers provide **optical access to spins**. For instance, NV center, in its negatively charged state (NV^-), has a spin-triplet ground state and spin-dependent photoluminescence, enabling spin readout and nanoscale sensing. Spin readout is commonly performed via ODMR;
- **Material control.** CVD growth, ion implantation, and annealing let us set the depth, orientation, and density of emitters. Nanofabrication (e.g., nanopillars, solid-immersion lenses, photonic crystals) improves light collection and coupling;
- **Robust and biocompatible.** High thermal conductivity limits laser heating, chemical stability allows operation in harsh media. In nanodiamond form, surface chemistry enables functionalization and cellular internalization.

1.4 Physical properties

Diamond exhibits a wide array of extreme properties, both in mechanical and physical domains. Its high bond energy (~7.73 eV) and dense atomic packing yield remarkable hardness (10 on the Mohs scale) and a very high Young's modulus (~1220 GPa). Chemically, it is inert, strongly hinting at the material biocompatibility, with surface degradation occurring only under strong oxidizing conditions at elevated temperatures. Low friction coefficients and chemical stability enable harsh-environment applications ranging from cutting tools to radiation-hard photonics.

Electrically, diamond is an insulator at room temperature due to its wide band gap (~5.5 eV). This also renders it transparent across a broad electromagnetic spectrum, from near-UV to far-infrared. The refractive index is approximately 2.42, which leads to significant internal reflection, a relevant factor in optoelectronic and photonic applications. Its Debye temperature, around 2200 K, implies a low

phonon population at room temperature, contributing to high thermal conductivity and minimized phonon-induced decoherence. A sharp first-order Raman line at 1332 cm^{-1} serves as a fingerprint of crystal quality and stress state.

Diamond's optical behavior is further influenced by point defects in the lattice, such as color centers [12]. These optically active centers, often introduced via doping or ion implantation, alter the band structure by embedding localized states within the gap. Depending on the nature of the defect and the excitation pathway, emission may arise either through zero-phonon lines (ZPLs),i.e narrow lines from purely electronic transitions without phonons, or phonon sidebands, which are broadened by lattice vibrations. Prototypical examples include the NV (ZPL at 637 nm) and group-IV centers such as Silicon-Vacancy (SiV, ZPL at 737 nm) and Germanium-Vacancy (GeV, ZPL at 602 nm), which differ in symmetry and spectral stability. These features, together with the above-mentioned inertness, highlight the diamond as promising candidate for a new generation of biosensors as will be extensively detailed in the following of this thesis.

Color centers will be discussed in Chap. 2.

1.4.1 Optically active defects in diamond

Optically active point defects in diamond introduce energy levels within the band gap and emit in visible range, for this reason these defects are called **color centers**. A widely used example is the NV center, formed by a substitutional nitrogen atom adjacent to a lattice vacancy.

This defects can form naturally during growth, or be engineered by introducing controlled defects into the diamond lattice [13].

They are commonly classified as:

- **Interstitial defects**, where foreign atoms are inserted between lattice sites;
- **Substitutional defects**, where an impurity atom replaces a carbon atom at a lattice position;
- **Vacancies**, corresponding to missing carbon atoms at lattice sites;
- **Complex defects**, which combine different types of atomic rearrangements, such as the NV center, which is the primary subject of this discussion [14, 11].

Techniques such as CVD, ion implantation, and annealing are commonly used to introduce and manipulate defect configurations with high spatial precision. From a metrological standpoint, this level of control supports reproducibility: the same growth and processing steps can be repeated to obtain emitters with comparable spectra, brightness and spin response [15].

1.4.1.1 Optical and radiative properties

The electronic transitions of color centers can be excited through optical stimulation, typically using laser light with sufficient photon energy to promote the system to the excited state, or through electrical injection [16]. Once excited, the system may decay via several relaxation mechanisms:

- **Radiative decay** directly to the ground state, emitting a photon corresponding to the ZPL;
- **Phonon-assisted radiative decay**, where the system relaxes to vibrational sublevels of the ground state, resulting in emission of photons with longer wavelengths (forming the phonon sidebands);
- **Non-radiative decay**, involving energy dissipation through lattice vibrations or interaction with nearby defects.

In metrology, these processes are relevant because they set how "clean" and "predictable" the emission is. The quantum efficiency (ratio of radiative to total decay rate) impacts the reliability of photon counting, while the ZPL position and linewidth determine how well the source can be used as a spectral reference.

Single photon application of color centers will be discussed in detail in Chap. 2. For the moment let us anticipate that single-photon behavior is commonly verified in a Hanbury Brown–Twiss (HBT) [17, 18] setup by measuring the second-order correlation function $g^{(2)}(0)$. A value of $g^{(2)}(0) < 0.5$ operatively indicates antibunching and identifies a single-photon emitter.

For centers with spin-dependent photoluminescence (notably NV^-), ODMR offers an optical tool for detection of spin transitions. In continuous-wave (CW) ODMR, a small change in fluorescence appears when the microwave frequency matches the spin resonance. The sharpness and depth of this feature, together with

the detected photon rate, determine how small a physical change can be resolved in a given time. Although detailed formulas are not required here, it is useful to keep in mind that narrower resonances, higher contrast and higher count rates lead to better (lower) detection limits. ODMR technique will be described in Chap. 3.

Linking the Raman reference to the ZPL position and to the ODMR frequency scale helps keep optical and microwave measurements on a common, traceable footing during long experimental runs.

1.5 Material production process and classification

Natural diamonds are formed deep within the Earth's mantle under high pressure and temperature, conditions that are not easily replicable or controllable. Therefore, synthetic diamond production techniques have been developed [19].

1.5.1 Material production process

High Pressure High Temperature (HPHT) This technique [20, 21] begins with a small diamond crystal known as a "seed," which is surrounded by carbon, typically in the form of graphite. The seed and carbon are placed in a metal solvent containing catalysts such as iron (Fe), cobalt (Co), or titanium (Ti), which accelerate the crystal growth process. The system is subjected to extreme pressures, around 10 GPa, and high temperatures of approximately 1770 K. These conditions mimic those found deep beneath the Earth's crust where natural diamonds form. Under such circumstances, graphite moves to the more stable diamond structure.

Although the HPHT method is reasonably low-cost, it often results in diamonds with significant impurities in the crystal lattice, limiting their use primarily to industrial applications. However, process refinement can reduce these impurities, particularly nitrogen, which is commonly present. By incorporating additional elements like titanium, aluminum, or zirconium as catalysts, these impurities can be chemically bound and prevented from entering the diamond lattice, improving the crystal quality. Further engineering (irradiation + annealing) enables controlled creation of color centers such as NV by vacancy formation and diffusion towards substitutional nitrogen.

Chemical Vapor Deposition (CVD) This process [22, 23] involves growing diamond layers atom by atom on a carefully selected substrate. The choice of substrate is critical to minimize lattice mismatch and mechanical strain. Ideally, a single-crystal diamond substrate is used to achieve homoepitaxial growth. Alternatively, substrates with similar crystal structures can be employed for heteroepitaxial growth.

During deposition, the substrate is maintained at a temperature of around 1000 K and under a low-pressure environment. A plasma, activated using microwaves at a frequency of 2.45–2.46 GHz, is generated from a gas mixture of carbon and hydrogen. This plasma facilitates the formation of carbon atoms in both sp^2 (graphite) and sp^3 (diamond) bonding configurations. However, the hydrogen in the plasma selectively removes sp^2-bonded carbon, favoring the deposition of pure diamond.

Additionally, gases such as nitrogen or boron may be introduced into the plasma during growth to intentionally introduce luminescent defects or to dope the diamond for specific electronic properties. While the CVD method is more expensive and time-consuming compared to HPHT, it enables the production of high-purity monocrystalline diamonds with costumized physical or optical characteristics. Patterned growth and post-growth nanofabrication allow for photonic structures (e.g., nanopillars, photonic-crystal cavities) that enhance collection efficiency and light–matter interaction.

1.5.2 Classification

Diamonds are categorized based on the type and concentration of impurities [24], particularly nitrogen and boron:

- **Type Ia**: Contain aggregated nitrogen atoms (typically 100–1000 ppm, IR–measurable), common in natural diamonds, typically used in mechanical-grade applications;
- **Type Ib**: Contain isolated nitrogen atoms (around $\sim$500 ppm, still IR–measurable), common in HPHT-grown diamonds, typically exhibit yellow coloration due to visible light absorption;
- **Type IIa**: Contain minimal nitrogen ($<$ 10 ppm, hard to measure with standard technique), resulting in high optical transparency, usually produced via CVD;

- **Type IIb**: Contain boron impurities that introduce p-type conductivity, nitrogen is typically even lower than in Type IIa (often $\lesssim$1–10 ppm, while boron is present at ppm levels sufficient to activate acceptor behavior;
- **Quantum Grade**: Achieved through isotopic purification (reducing the natural ^{13}C fraction of $\sim$1.1% to $\lesssim$0.1% or lower), which minimizes magnetic noise and optimizes performance for quantum technologies.

1.6 Nanodiamonds

NDs are diamond particles with typical sizes ranging from a few nanometers up to $\sim$200 nm. NDs can be synthesized via top-down methods (milling of HPHT or CVD crystals) or bottom-up approaches (e.g., detonation synthesis), achieving sub-10 nm dimensions [25]. Their extremely small size makes nanodiamonds especially promising for biological applications, including in vivo experiments, due to their biocompatibility and potential for cellular internalization [26]. This same nanoscale, however, introduces limitations such as an increased sensitivity of defect spins to environmental noise.

In bulk diamond, the spin coherence time of color centers, often quantified by T_2^* and T_2 (where T_2^*, the inhomogeneous dephasing time, is the free-precession coherence time observed without refocusing and is dominated by static or slowly varying inhomogeneities, while T_2, the dephasing time, is the longer echo-limited coherence time measured with refocusing pulses that cancel quasi-static disorder), is mostly limited by nearby electronic and nuclear spins [27]. In NDs, the much larger surface-to-volume ratio introduces additional decoherence from surface spins and charge fluctuations, which results in the reduction of T_2^* and must be considered when estimating the sensitivity of ND-based sensors. Surface termination (e.g., H-, O-, or F-terminated) and near-surface charge traps influence the NV^-/NV^0 ratio and thus photostability and spin-readout contrast. Customized chemical treatments and oxidation can partially mitigate these effects.

Despite these drawbacks, nanodiamonds have attracted growing interest in biomedicine, not only as non-toxic alternatives to quantum dots for imaging, but also as platforms for magnetic and thermal sensing and as drug-delivery carriers. Their

surface can be chemically modified thanks to the versatility of carbon's covalent bonds, enabling functionalization for a wide range of applications.

This broad potential is driving research into new manufacturing techniques, even though existing methods already offer high-purity nanodiamonds with tunable surface properties at relatively low cost. NDs are commonly produced by milling larger CVD or HPHT-grown crystals, typically yielding particles between 20 and 200 nm [28]. To obtain even smaller sizes, desirable for cellular uptake, detonation synthesis is used [29, 30], which starts from solid carbon-rich precursors and can produce NDs just a few nanometers in diameter.

Chapter 2

Color centers in diamond as single photon sources for metrologilcal applications

In this chapter, I will introduce diamond color centers as SPS. First, we will expose the main SPS properties, then we will briefly review the main application area, in particular, quantum computing, quantum cryptography, and metrology, and explain how single emitters are identified via the second-order correlation function. The final part develops two, and three-level models to extract key figures of merit: lifetime, saturation power, and saturated count rate.

2.1 SPS properties

An ideal SPS should satisfy:

- **Single-photon purity.** Each trigger produces one and only one photon (no multi-photon events);
- **Deterministic emission.** The emission probability per trigger is unity (≈ 1), avoiding pulses (no vacuum component);

- **High brightness.** Large detected count rate, combining a high repetition rate and efficient extraction into the measured mode together with good detection efficiency;
- **Indistinguishability.** Successive photons are identical in spectrum, temporal profile, and polarization, so they interfere reliably in photonic circuits.

These represent an idealized target. Real SPS platforms approach them only approximately: background light, spectral diffusion, phonon coupling, and finite extraction reduce purity, introduce empty pulses, or limit indistinguishability.

State-of-the-art single photons in many laboratories still come from spontaneous parametric down-conversion (SPDC) [31]. In SPDC a pump photon in a $\chi^{(2)}$ nonlinear crystal splits probabilistically into a lower energy pair, called signal and idler, because of energy and momentum conservation. Detection of the idler heralds the presence of the signal photon and yields high purity single photon streams at the cost of probabilistic emission. Increasing the pump increases brightness but also the rate of multi pair events. For scalable quantum technologies it is therefore preferable to have on demand sources in which a trigger deterministically produces one photon. Beyond SPDC, other platforms offer complementary strengths for generating single photons (summarized in Tab. 2.1). In integrated photonics, four-wave mixing in nonlinear waveguides produces chip-scale and telecom-friendly sources at room temperature, but this process remains probabilistic and Raman noise must be controlled. Semiconductor quantum dots, when driven resonantly, can emit nearly deterministic and highly indistinguishable photons, but this process requires cryogenic conditions. Single organic molecules provide bright emission with narrow spectral lines, but this process requires low temperatures. Trapped atoms and ions generate deterministic and highly coherent photons, but this approach requires comparatively bulky apparatus. To move in the direction of an SPS with deterministic emission, near-unity probability per trigger, and operation at room temperature, attention has shifted to solid state defects.

Table 2.1 Representative single-photon platforms. The table compares typical solid-state and atomic systems used for single-photon generation, emphasizing their emission wavelengths, operational conditions, and advantages for quantum technologies.

Platform	**Pros**	**Cons**
SPDC	Mature and widely used; operates at room temperature; tunable emission from 600–1700 nm; good entanglement fidelity	Probabilistic photon generation; multi-pair events increase with pump power; limited on-demand capability
Atoms and Ions	Deterministic emission; highly coherent and narrow linewidth photons; excellent quantum memory compatibility	Requires complex and bulky setups; limited scalability and repetition rate; often cryogenic or cavity operation needed
Quantum Dots	Near-deterministic emission; high efficiency ($> 90\%$) and indistinguishability with cavities; telecom range operation possible	Requires cryogenic temperatures; sensitive to charge noise and nanofabrication imperfections
Four-Wave Mixing	CMOS-compatible and chip-scale integration; telecom-band operation; room-temperature compatible	Probabilistic generation; Raman noise; filtering needed for high purity
Color Centers in Diamond	Solid-state operation; room-temperature capable; stable emission; potential for spin–photon entanglement	Low collection efficiency; spectral diffusion; limited brightness and indistinguishability

Diamond color centers move in this direction, providing triggered emission at (or near) ambient conditions and compatibility with integrated photonics [12, 15]. In practice, purity is checked with HBT test (will be extensively discussed in the next sections) [18], while brightness and overall efficiency come from saturation curves and detected count rates. Beyond these device metrics, diamond's wide band gap, strong sp^3 bonds, and excellent thermal/chemical stability isolate defect states and yield stable optical transitions with clear ZPLs and phonon sidebands. In this

framework, color centers, luminescent point defects in the lattice, serve as reliable single-photon sources for metrology, communication, and sensing [32, 11, 14].

The introduction of defect states within diamond crystal modifies its electronic structure by creating localized energy levels inside its wide bandgap ($\sim$ 5.5 eV). This large bandgap plays a crucial role in isolating the defect states from both the conduction and valence bands, effectively shielding them from environmental perturbations. As a result, color centers in diamond exhibit highly stable and coherent optical transitions with well-defined ZPL and phonon sidebands, a feature that is particularly valuable when measurements must be repeatable and traceable [11].

From a metrological viewpoint, the usefulness of diamond color centers is dual:

- On the photonics side, they provide streams of single photons with predictable statistics and stable spectra, so that quantities such as ZPL, photon rate and timing can be compared over time and between instruments;
- On the sensing side, some centers also offer optical access to spin states, as a consequence small shifts in the resonance can be read optically and converted into calibrated values of magnetic field, temperature or strain. .

In practice, this means that the same physical system can serve both as a source of well-characterized photons and as a primary element in a quantitative sensor

In particular, the NV center has emerged as a leading platform for quantum-enabled metrology. Its controllable optical properties, high quantum efficiency, and operational stability under ambient conditions make it an ideal candidate for developing standardized SPS [33, 34]. At the same time, its spin-dependent photoluminescence enables ODMR, which will be discussed in Chap. 3. These characteristics bridge fundamental quantum studies with practical metrological applications.

2.2 Application

Diamond color centers applications range from quantum computation to quantum cryptography and metrology. Their strengths are room-temperature operation, photostability, and the possibility to integrate emitters in nanophotonic devices [12, 15, 35].

2.2.1 Quantum computation

Quantum computing exploits two key quantum features, superposition and entanglement, to gain speedups for specific kinds of tasks respect to classical computing. In this paradigm, information is encoded in quantum bits (qubits) rather than classical bits. Quantum information processing (QIP) investigates physical systems where qubits can be created, controlled, and read out with high fidelity [35, 36].

Many platforms are under active study: trapped atoms[37] and ions [38], photons[39], nuclear spins in molecules[40], superconducting circuits[41], semiconductor quantum dots[42], and point defects in solids[43]. For a technology to be viable it should meet the standard set of requirements often summarized as the DiVincenzo criteria (for computation) [44]:

- Scalability and well-defined qubits;
- Initialization: reliable preparation of the qubit state;
- Long coherence: T_2 much longer than single–gate times;
- Universal control: availability of a universal set of quantum gates;
- Readout: selective, high-fidelity measurement of individual qubits[35, 36].

the NV center looks to be very promising since it matches these needs in a good way. The NV^- electronic spin offers millisecond-scale coherence times under optimized conditions (much longer than typical microwave gate durations), and it can be optically initialized and read out because the spin sublevels have different photoluminescence brightness. In zero-field condition, the ground-state triplet can be well approximated as a two-level system formed by $|m_s = 0\rangle$ and one of $|m_s = \pm 1\rangle$, this effective qubit can be driven by resonant microwaves. Moreover, NV electronic spins can be coupled to nearby nuclear spins, enabling small multi-qubit registers and basic error-correction or memory functions within the same diamond lattice [45–47].

2.2.2 Quantum key distribution

Classical cryptography protects messages by making them unreadable to unauthorized parties. Since the rise of digital communications, public-key methods have

relied on problems that are believed to be hard for ordinary (“classical”) computers, for example integer factorization. This works today because even powerful machines need an impractically long time to solve them. However, large-scale quantum computers could break many of these schemes in the future. Quantum key distribution (QKD) offers a complementary path: it uses quantum physics to let two users establish a shared secret key with security based on physical laws rather than on computational assumptions.

A standard protocol is BB84 [48] (Fig. 2.1). The sender (Alice) encodes each bit in the polarization of a single photon, choosing at random between two bases: horizontal/vertical (H/V) or diagonal ($\pm 45^\circ$). The receiver (Bob) also chooses a measurement basis at random. After transmission, they reveal over a public channel only the sequence of bases, not the bit values, and they keep the events where the bases match. These outcomes form the sifted key. Because the choices are independent and uniform, the probability of using the same basis is $1/2$, so about half of the detected photons contribute to the sifted key. Security relies on two physical facts. First, a quantum measurement projects the state and, if done in the wrong basis, disturbs it. Second, the no-cloning theorem forbids exact copies of unknown quantum states. In a simple intercept–resend attack, an eavesdropper (Eve) measures each photon in a random basis and sends a new one. Conditioned on the kept events, the quantum bit error rate (QBER, i.e., the fraction of mismatched bits between Alice and Bob) rises to about 25% in the ideal, noiseless case. In practice, Alice and Bob reveal a random sample to estimate the QBER, if it is above a chosen threshold they abort, otherwise they run error correction and privacy amplification.

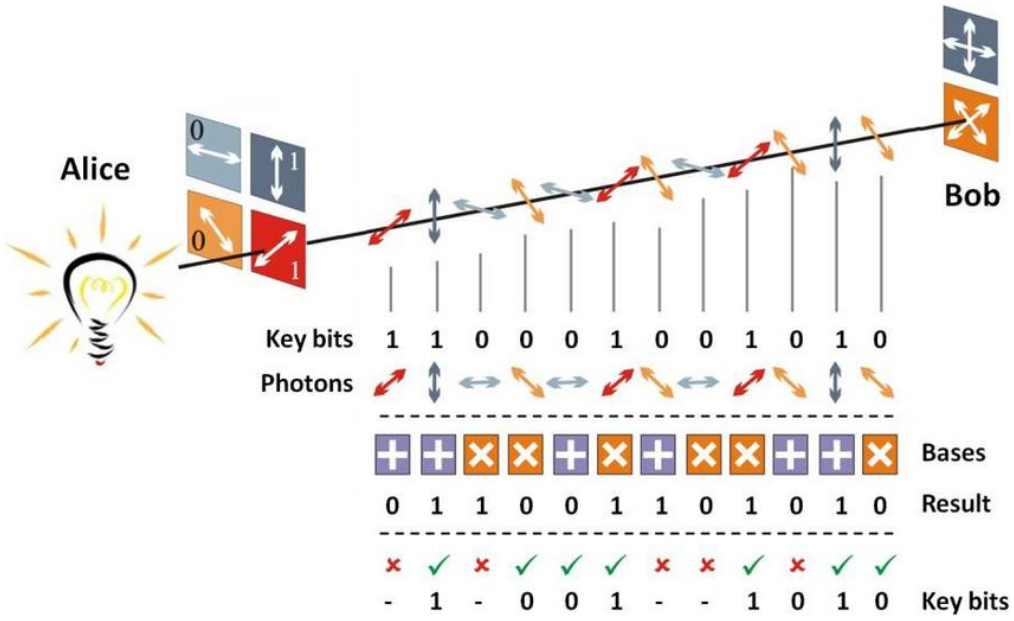

Fig. 2.1 BB84 workflow [3]. Alice encodes bits on single-photon polarizations in two random bases (H/V and $\pm 45^{\circ}$), while Bob measures in random bases. The protocol keeps only matching bases to form the raw key, demonstrating the fundamental principle of quantum key distribution.

The physical source matters. Attenuated lasers (weak coherent pulses) do not emit true single photons: their photon number follows a Poisson distribution with a non-negligible multi-photon component at typical mean intensities. This enables the photon-number-splitting (PNS) attack: Eve can split off one photon from a multi-photon pulse, store it, and measure it later in the correct basis after the bases are revealed. In this way she may learn the bit without necessarily increasing the QBER. Channel losses can hide the missing photons and make the attack difficult to detect. There are two common countermeasures. One is the decoy-state method, which varies the mean photon number to detect signatures of PNS. The other is to use true SPS that strongly suppress multi-photon emission. Solid-state emitters based on diamond color centers, such as NV centers, are promising: they work at room temperature, can be integrated in fiber or free-space links, and have shown single-photon behavior in early proof-of-principle experiments.

In summary, QKD turns measurement disturbance and the no-cloning principle into operational checks: when bases match, Alice and Bob get the same bits (up to noise), while eavesdropping or technical imperfections appear as an increased QBER. Using true single-photon emission, ideally from robust solid-state SPS, closes the

multi-photon loophole of weak coherent pulses and improves the practical security of QKD systems.

2.2.3 Metrology

Metrology is the science of measurement, it encompasses a wide range of activities that can be grouped in three main areas: definition of International System Units (SI), realization of them as primary standards, transfer of them through calibration chains. A goal of metrology is also to quantify uncertainty so that measurement results are comparable and traceable across instruments, laboratories, and time.

Metrolgy has at its core the seven SI base units which are:

- the second (s) as unit of time;
- the meter (m) as unit of lenght;
- the kilogram (kg) as unit of mass;
- the ampere (A) as unit of electric current;
- the kelvin (K) as unit of temperature;
- the mole (mol) as unit of amount of substance;
- the candela (cd) as unit of luminous intensity.

The last (cd) is the unit more relevant for the rest of this discussion, since it is focused on quantum optical sensors.

At very low optical flux, classical radiometers face practical limits, SPS offer a complementary, quantum-based route by counting individual quanta of light and relating optical quantities to fundamental constants.

This section first outlines a photon-counting view of the candela, then gives a short overview of quantum sensing with diamond color centers (treated in depth later in the thesis).

2.2.3.1 Radiometry and the candela with SPS

In the SI, the unit of luminous intensity is defined by taking the fixed numerical value of the luminous efficacy of monochromatic radiation of frequency 540×10^{12} Hz, K_{cd}, to be 683 when expressed in the unit $\mathrm{lm/W}$, which is equal to $\mathrm{cd\,sr/W}$, or $\mathrm{cd\,sr\,s^3/kg\,m^2}$, where the kilogram, metre and second are defined in terms of h, c and $\Delta\nu_{\mathrm{Cs}}$. At very low light levels, SPS suggest a simpler, photon-counting view. Each photon of frequency ν carries energy $h\nu$, so counting photons per second gives the optical power directly. With a known collection geometry (solid angle), this becomes a radiant intensity, which can then be converted into luminous intensity using the photopic efficacy ($683\,\mathrm{lm\,W^{-1}}$) and the eye-sensitivity curve $V(\lambda)$.

In this way, a calibrated SPS can realize the candela by counting photons rather than comparing thermal power. This is especially useful at ultra-low flux and benefits from SPS features such as antibunching and spectral stability, which help reduce uncertainty in radiometric and photometric calibration [12].

2.2.3.2 Quantum sensing

Quantum sensing exploits quantum states of matter to probe physical quantities with high precision. In diamond, several color centers allow optical preparation and readout of an electronic spin, which acts as a local probe for magnetic and electric fields, temperature, and strain [49–51, 7].

Since quantum sensing with NV centers is a main topic of this thesis, the topic will be deeply discussed in Chap. 3. Here I will just anticipate two key ingredients on NV-based quantum sensing:

- **Spin addressability at room temperature.** The ground-state spin triplet of $\mathrm{NV^-}$ is optically polarized and read out via spin-dependent fluorescence [11, 33];
- **Field dependent resonance.** Magnetic field, temperature, strain, and electric fields shift the resonance frequency through known couplings, allowing calibrated measurements [50, 51].

2.3 SPS identification theory

Although any optical field is made of photons, classical sources (lamps, lasers at high power) display statistics and correlations that differ from those of truly quantum sources. As we have briefly discussed, since photon states, or more in general, nonclassical states are now key resources for quantum technologies, it is important to have clear, quantitative tests to certify them.

2.3.1 Glauber function $g^{(2)}$

A widely adopted tool for the characterization of SPS is the second–order autocorrelation function $g^{(2)}(\tau)$ (Glauber function) [17, 18], where τ represents the time delay between two detection events, i.e., the difference in arrival times of photons at two detectors. By analyzing how the correlation changes as a function of τ, one can determine whether photons tend to arrive together (bunching) or are separated (antibunching). For light that can be modeled as classical random intensity one always has $g^{(2)}(0) \geq 1$: coherent light is Poissonian with $g^{(2)}(0) = 1$, while thermal (chaotic) light is super-Poissonian and shows bunching with $g^{(2)}(0) > 1$. In contrast, non-classical sub-Poissonian light exhibits antibunching with $g^{(2)}(0) < 1$, an ideal single-photon source reaches the limit $g^{(2)}(0) = 0$ (Fig. 2.2).

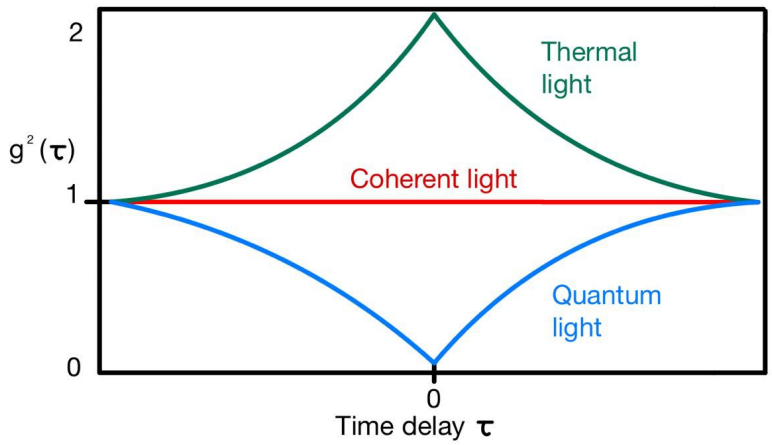

Fig. 2.2 Glauber function for different types of light. The plot compares classical, coherent, and antibunched photon statistics, showing how the second-order correlation distinguishes quantum from classical sources.

Experimentally, $g^{(2)}(\tau)$ is measured with a HBT setup (Fig. 2.3).

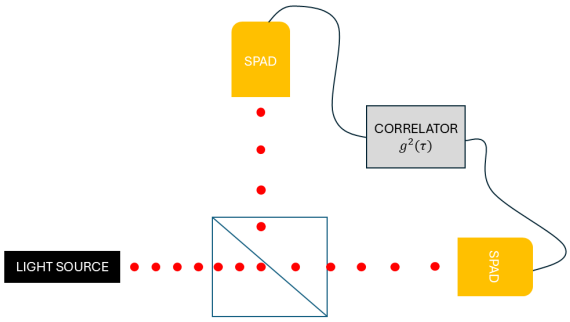

Fig. 2.3 Typical Hanbury Brown–Twiss setup. The schematic shows the main components: a 50:50 beam splitter that divides the incoming photons, two single-photon detectors that register the photons, and a correlator module that measures the time correlations between detection events.

The emitted signal is sent to a 50:50 beam splitter, the two outputs are detected by independent single-photon detectors. Each detection event is time-stamped,

and a correlator builds a histogram $C(\tau)$ of delays between clicks on different detectors. After normalization by the single count rates and the acquisition settings, this histogram gives a dimensionless trace that represents $g^{(2)}(\tau)$. In practice, a single-photon source shows an antibunching dip at $\tau = 0$ (Fig. 2.2), while background and detector effects only change the overall contrast if not corrected.

The mathematical definition is

$$g^{(2)}(\tau) = \frac{\langle I(t)\, I(t+\tau)\rangle}{\langle I(t)\rangle^2},$$

where $I(t)$ is the intensity of the light that could also be expressed by field operators $\hat{E}^{(\pm)}$, or equivalently the annihilation/creation operators $\hat{a}$ and $\hat{a}^\dagger$. Using the notation with $\hat{a}$ and $\hat{a}^\dagger$ and considering $t = 0$ (zero delay) the function results:

$$g^{(2)}(0) \;=\; \frac{\langle \hat{a}^\dagger \hat{a}^\dagger \hat{a}\hat{a}\rangle}{\langle \hat{a}^\dagger \hat{a}\rangle^2}. \tag{2.1}$$

We now exploit the canonical commutation relation

$$[\hat{a}, \hat{a}^\dagger] = 1\,, \tag{2.2}$$

and define the photon–number operator as $\hat{n} = \hat{a}^\dagger \hat{a}$. Then we can rewrite:

$$g^{(2)}(0) \;=\; \frac{\langle \hat{a}^\dagger(\hat{a}\hat{a}^\dagger - 1)\hat{a}\rangle}{\langle \hat{a}^\dagger \hat{a}\rangle^2} \;=\; \frac{\langle \hat{n}(\hat{n}-1)\rangle}{\langle \hat{n}\rangle^2}. \tag{2.3}$$

For an ideal one–photon SPS state, $n = 1$ with unit probability, resulting in $g^{(2)}(0) = 0$. If two independent identical emitters contribute equally, the minimum is $g^{(2)}(0) = 0.5$. Therefore, the practical criterion $g^{(2)}(0) < 0.5$ is commonly taken as evidence of the presence of a single photon emitter.

In real measurements, background photons and detector dark counts partially fill the antibunching dip, so the raw $g^{(2)}(0)$ appears higher than its true value. Background correction is therefore required before comparing sources, and methods for limiting the background must be identified.

2.4 SPS characterization theory

After identifying a SPS, its emission can be summarized by a few key parameters: the excited–state lifetime τ (average time spent in the excited level when the pump is off), the saturation power P_{sat}, and the saturated count rate I_∞. These quantities can be estimated with simple rate–equation models.

2.4.1 Two-level SPS model

Consider a two-level emitter with ground state (1) and excited state (2). A laser excites $1\to2$ at rate k_{12}, and radiative decay returns $2\to1$ at rate k_{21}. A sketch is shown in Fig. 2.4.

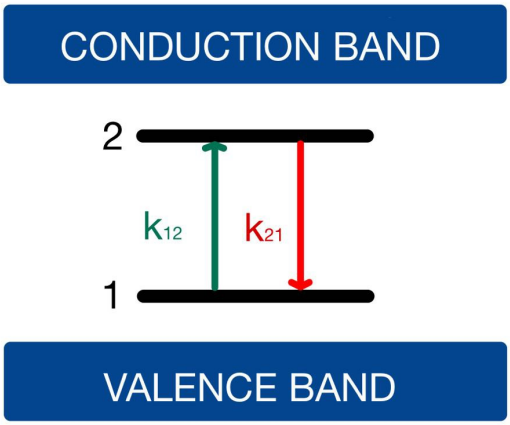

Fig. 2.4 Two-level energy diagram. The diagram represents the basic quantum system with ground and excited states, used to describe simple optical transitions.

Rate equations and steady state. Denoting by $n_1(t)$ and $n_2(t)$ the occupation probabilities of levels 1 and 2 (with $n_1+n_2=1$), their dynamics is

$$\begin{aligned} \dot{n}_1(t) &= -k_{12}\,n_1(t)+k_{21}\,n_2(t), \\ \dot{n}_2(t) &= \quad k_{12}\,n_1(t)-k_{21}\,n_2(t). \end{aligned} \tag{2.4}$$

At steady state,

$$n_2(\infty) = \frac{k_{12}}{k_{12}+k_{21}}. \tag{2.5}$$

Saturation curve. The detected fluorescence is proportional to the radiative return from level 2:

$$I \propto k_{21}\, n_2(\infty) = \frac{k_{21}\, k_{12}}{k_{12}+k_{21}}. \tag{2.6}$$

For continuous excitation the excitation rate is linearly proportional to the excitation power through a coefficient α, $k_{12} = \alpha P$, moreover it is convenient to define

$$I_\infty \propto k_{21}, \qquad P_{\text{sat}} = \frac{k_{21}}{\alpha}. \tag{2.7}$$

With these definitions the intensity follows the standard saturation law

$$I(P) = I_\infty \frac{P}{P+P_{\text{sat}}}. \tag{2.8}$$

In practice, after acquiring $I(P)$, Eq. (2.8) is fitted to extract P_{sat} and I_∞.

Antibunching and lifetime. A single emitter cannot emit two photons at the same time, so the second–order autocorrelation shows an antibunching dip at $\tau = 0$ (see Fig. 2.5). Immediately after a photon is emitted (at $t = 0$), the system is in the ground state, so $n_2(0) = 0$. Solving Eq. (2.4) gives

$$n_2(t) = n_2(\infty)\Big(1 - e^{-\lambda t}\Big), \qquad \lambda \equiv k_{12}+k_{21}. \tag{2.9}$$

Since $I(t) \propto k_{21} n_2(t)$, the normalized autocorrelation results:

$$g^{(2)}(\tau) = \frac{\langle I(0)\, I(\tau)\rangle}{\langle I\rangle^2} \simeq \frac{n_2(\tau)}{n_2(\infty)} = 1 - e^{-\lambda|\tau|}. \tag{2.10}$$

Measuring $g^{(2)}(\tau)$ at different laser powers yields $\lambda(P)$. With $k_{12} = \alpha P$ and $k_{21} = 1/\tau$:

$$\lambda(P) = \alpha P + \frac{1}{\tau}, \tag{2.11}$$

so a linear fit of λ vs. P gives the lifetime τ from the intercept.

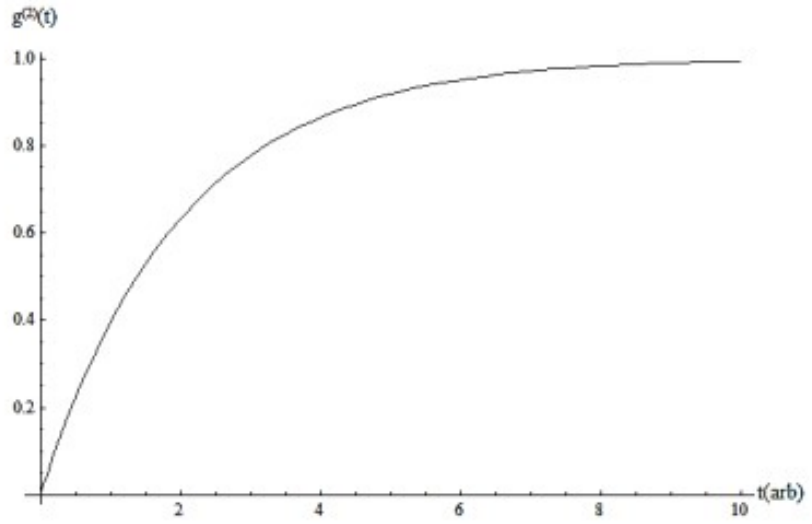

Fig. 2.5 Second-order autocorrelation function for a two-level system. The curve shows the antibunching dip characteristic of single-photon emission.

2.4.2 Three-level SPS model

In many solid–state emitters the optical cycle includes a long–lived, non-radiative metastable state (3). The emitter is pumped from the ground state (1) to the bright excited state (2), but can occasionally be “shelved” in state (3) before returning to (1). A sketch is shown in Fig. 2.6.

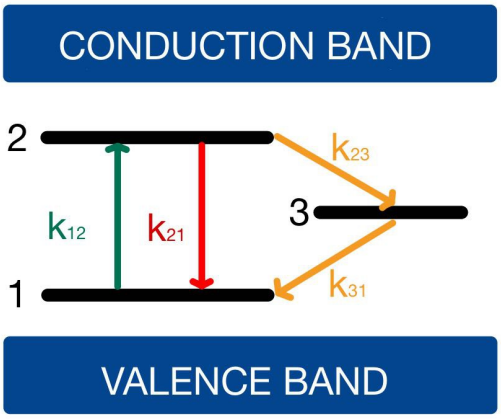

Fig. 2.6 Three-level energy diagram. The scheme introduces an additional metastable state to describe shelving effects and fluorescence intermittency.

Rate equations and steady state. The populations obey

$$\begin{aligned} \dot{n}_1 &= -k_{12}\,n_1 + k_{21}\,n_2 + k_{31}\,n_3, \\ \dot{n}_2 &= +k_{12}\,n_1 - (k_{21} + k_{23})\,n_2, \\ \dot{n}_3 &= +k_{23}\,n_2 - k_{31}\,n_3, \end{aligned} \tag{2.12}$$

with $n_1 + n_2 + n_3 = 1$ and $k_{12} = \alpha P$. In steady state the excited–state probability results:

$$n_2(\infty) \;=\; \frac{k_{12}\,k_{31}}{k_{31}(k_{12} + k_{21}) + k_{12}k_{23}}. \tag{2.13}$$

Saturation curve. The detected intensity is proportional to the radiative return from level (2):

$$I(P) \;\propto\; k_{21}\,n_2(\infty) \;=\; k_{21}\,\frac{k_{12}\,k_{31}}{k_{31}(k_{12} + k_{21}) + k_{12}k_{23}}. \tag{2.14}$$

With $k_{12} = \alpha P$, this can be written in the standard saturation form

$$I(P) \;=\; I_\infty \frac{P}{P + P_{\text{sat}}}, \tag{2.15}$$

where the effective parameters include the shelving dynamics:

$$I_\infty \propto \frac{k_{21}}{1+k_{23}/k_{31}}, \qquad P_{\text{sat}} = \frac{k_{21}+k_{23}}{\alpha\,(1+k_{23}/k_{31})}. \tag{2.16}$$

Intuitively, spending time in the dark state reduces the maximum brightness and shifts saturation to higher power.

Antibunching, bunching and lifetime. Because of occasional shelving, the second–order autocorrelation shows a fast antibunching dip plus a slower bunching shoulder (see Fig. 2.7):

$$g^{(2)}(\tau) = 1-(1+a)\,e^{-|\tau|/\tau_1}+a\,e^{-|\tau|/\tau_2}. \tag{2.17}$$

Here τ_1 is set by the bright 1–2 cycle (pump and radiative rates), τ_2 reflects the slow 2–3–1 pathway, and a sets the bunching amplitude. If k_{23}, k_{31} are negligible, Eq. (2.17) reduces to the two–level form $g^{(2)}(\tau) = 1 - e^{-|\tau|\lambda}$.

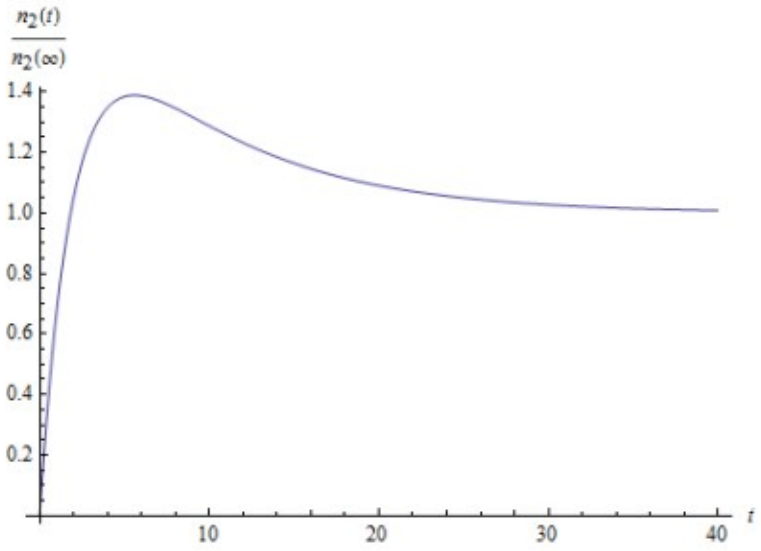

Fig. 2.7 Second-order autocorrelation function for a three-level system. The plot illustrates photon bunching and antibunching behavior as a result of transitions through the metastable state.

Chapter 3

Nitrogen-Vacancy Center and Optically Detected Magnetic Resonance

NV center has a prominent role in diamond-based quantum technology. This chapter introduces the NV center in diamond, from its atomic structure and charge states to the ground-state spin model used in experiments. It then connects this model to ODMR, going through continuous-wave operation, the differential method for fast tracking of resonance shifts, and the main pulsed sequences. The emphasis is on how the NV spin is prepared, driven, and read out, and on how external fields and temperature shift the resonance, tools that will be used later for quantitative sensing.

3.1 NV Center

NV center in diamond is a point defect composed of a substitutional nitrogen atom positioned next to a missing carbon atom (vacancy) along one of the four equivalent crystallographic axes [14, 34] (Fig. 3.1). While NV centers can occur naturally during diamond growth, they can also be created through ion implantation followed by thermal annealing [13, 52], which mobilizes vacancies and promotes their recombination with nitrogen impurities.

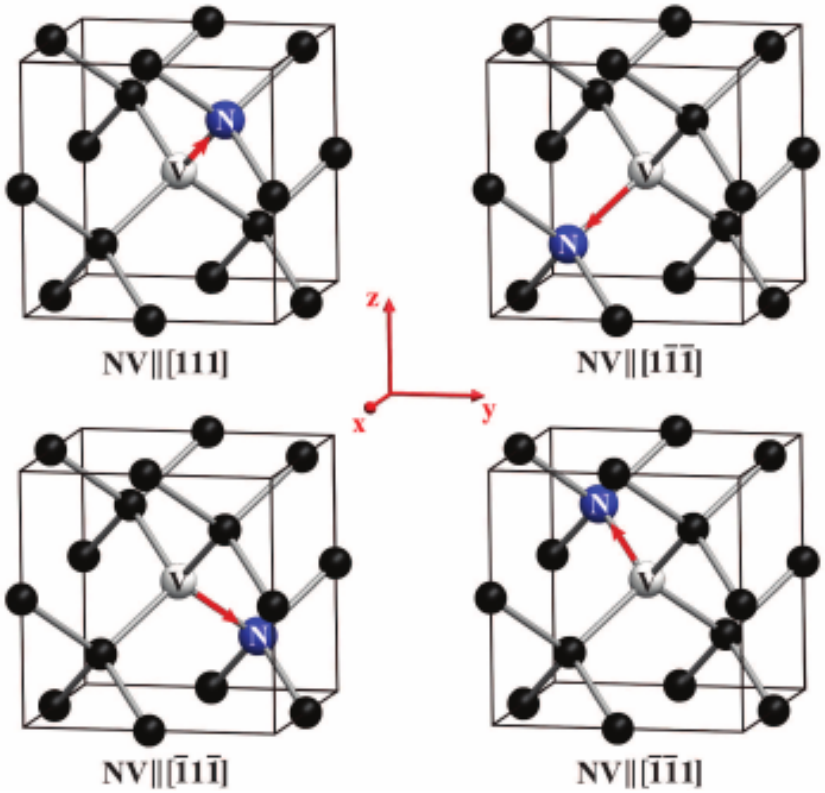

Fig. 3.1 Schematic representation of different orientations of the NV center within the diamond crystal lattice [4]. The illustration highlights the four possible [111] axes of alignment.

Two charge states are possible: the neutral NV^0 and the negatively charged NV^-. The NV^- state is of particular interest for quantum technologies due to its robust optical and spin properties at room temperature. In NV^-, six electrons occupy localized defect orbitals, five from the unpaired valence orbitals of the three nearest-neighbor carbons and the nitrogen atom, plus one additional electron donated by the lattice or nearby donors such as substitutional nitrogen.

The photoluminescence (PL) spectrum of NV centers shows a sharp ZPL and a broad phonon sideband (Fig. 3.2). The ZPL is located at 637 nm for NV^- and at 575 nm for NV^0 [11, 33]. These spectral features enable identification of the charge state in optical measurements. NV^- is especially relevant for quantum sensing and quantum information processing because it possesses an optically addressable spin-triplet ground state.

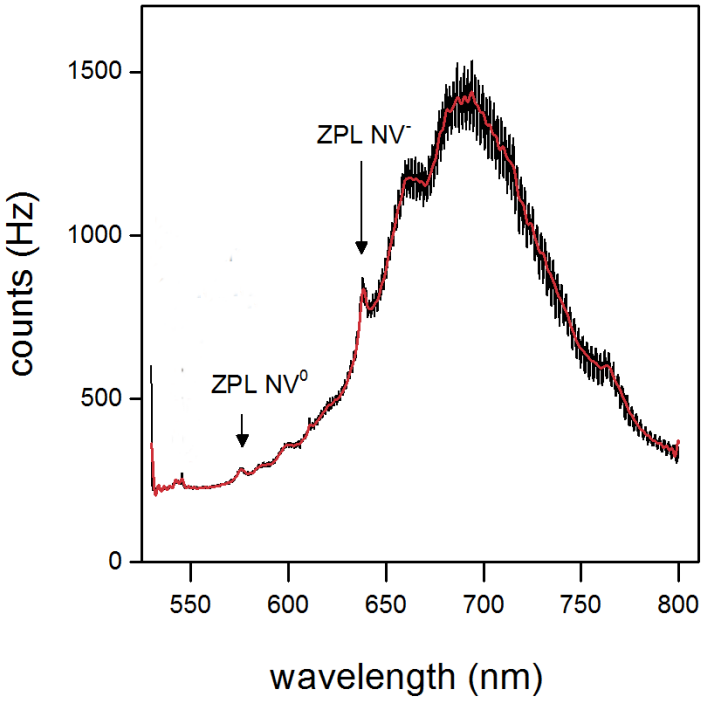

Fig. 3.2 Emission spectrum of NV centers showing the ZPLs for NV^0 and NV^-, along with the phonon sideband [5]. The spectrum reveals the optical signatures of the two charge states.

3.1.1 Atomic structure and ground-state model

In the NV^- configuration, the defect exhibits trigonal symmetry described by the C_{3v} point group, with the symmetry axis aligned along a $\langle 111 \rangle$ direction. In simple terms, C_{3v} is the set of symmetry operations that leave the NV center unchanged: a three-fold rotation about the NV axis and three vertical mirror planes. This symmetry fixes a unique axis for the defect and groups electronic states into non-degenerate (A) and doubly degenerate (E) types.

From an electronic perspective, the NV^- center can be modeled as a set of molecular-like defect orbitals [11, 49] (Fig. 3.3). The nitrogen atom and the three adjacent carbons contribute sp^3-hybridized orbitals, which combine to form localized states within the 5.5 eV band gap of diamond:

- a fully occupied, non-degenerate a_1 orbital;
- a doubly degenerate e orbital, partially filled in NV^-.

The labels a_1 and e correspond directly to the C_{3v} irreps: a_1 is an A-type (non-degenerate) level, while e is an E-type (doubly degenerate) pair. Thus, the observed one-level vs. two-level structure of the defect orbitals follows from the NV symmetry.

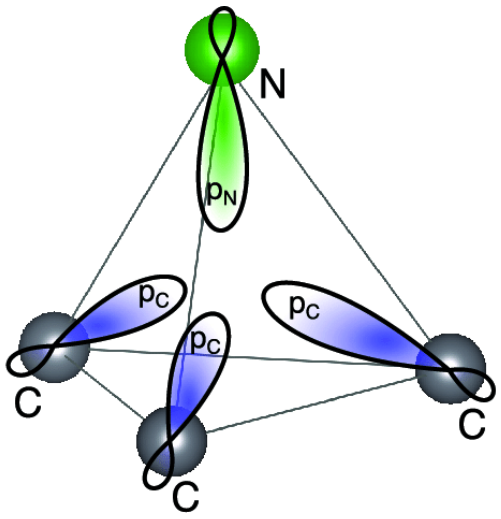

Fig. 3.3 Schematic of an NV center and its dangling p orbitals [6]. The model depicts the atomic configuration and the electronic structure responsible for optical transitions.

The six electrons in these defect orbitals, five from the nitrogen and adjacent carbons plus one extra electron, lead to a spin-triplet ground state ($S = 1$) denoted $^3A_2$, with a triplet excited state ^3E. Here the superscript ^{3} gives the spin multiplicity ($2S+1 = 3$). The letters A and E again refer to C_{3v}: $^3A_2$ is a non-degenerate triplet ground state and ^3E is a doubly degenerate triplet excited state. These symmetry labels also guide the allowed optical transitions between ground and excited states. Intermediate singlet states mediate a spin-dependent intersystem crossing (ISC) [11, 14]. In the excited triplet, $|m_s = \pm 1\rangle$ sublevels preferentially decay non-radiatively, whereas $|m_s = 0\rangle$ predominantly decays radiatively (Fig. 3.4). This difference enables optical spin readout, as $|m_s = 0\rangle$ appears brighter than $|m_s = \pm 1\rangle$.

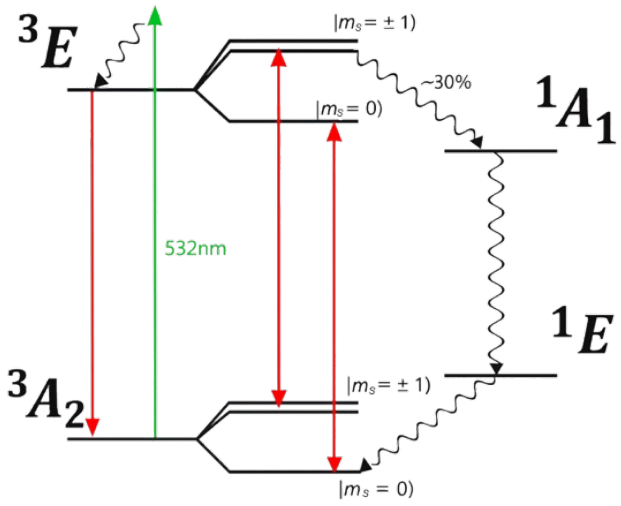

Fig. 3.4 Energy-level diagram of the NV center showing the triplet ground and excited states, singlet states, and typical optical transitions. The diagram summarizes the electronic pathways relevant for spin initialization and readout.

Continuous optical excitation drives the system through ISC and preferentially polarizes the spin into $|m_s = 0\rangle$ [53].

3.1.2 System Hamiltonian

To connect the NV energy levels with what is measured in ODMR, we use the standard ground-state spin Hamiltonian [11] in the NV crystal frame (with z along the NV axis):

$$\begin{aligned}\frac{\hat{H}_{\mathrm{gs}}}{h} &= D_{\mathrm{gs}}\left(\hat{S}_z^2 - \frac{S(S+1)}{3}\right) \\ &\quad + A_{\mathrm{gs}}^{\parallel}\hat{S}_z\hat{I}_z + A_{\mathrm{gs}}^{\perp}\left(\hat{S}_x\hat{I}_x + \hat{S}_y\hat{I}_y\right) \\ &\quad + P_{\mathrm{gs}}\left(\hat{I}_z^2 - \frac{I(I+1)}{3}\right) + \frac{\hat{V}_{\mathrm{env}}}{h},\end{aligned} \tag{3.1}$$

where hats denote quantum operators. Here, $\hat{S}_{x,y,z}$ are the electron-spin operators and $\hat{I}_{x,y,z}$ are the nuclear-spin operators of the nitrogen atom, with nuclear spin I = 1 for the native ^{14}N isotope (or I = 1/2 for ^{15}N). The zero-field splitting $D_{\mathrm{gs}} \approx 2.87\,\mathrm{GHz}$ sets the energy separation between the $|m_s = 0\rangle$ and $|m_s = \pm 1\rangle$ states, thereby fixing the central ODMR frequency at zero magnetic field. The axial

and transverse hyperfine coupling constants, $A_{\parallel}^{\mathrm{gs}}$ and $A_{\perp}^{\mathrm{gs}}$, give rise to the characteristic hyperfine multiplet structure observed in ODMR spectra. P_{gs} is the nuclear quadrupole parameter (for ^{14}N) and slightly refines these splittings.

Environmental perturbations (magnetic/electric fields and crystal strain) enter as

$$\begin{aligned}\frac{\hat{V}_{\mathrm{env}}}{h} &= \gamma_e\,\hat{\mathbf{S}}\cdot\mathbf{B} + \gamma_N\,\hat{\mathbf{I}}\cdot\mathbf{B} \\ &\quad + d_{\mathrm{gs}}^{\parallel}(E_z+\delta_z)\left(\hat{S}_z^2 - \tfrac{S(S+1)}{3}\right) \\ &\quad + d_{\mathrm{gs}}^{\perp}\Big[(E_x+\delta_x)(\hat{S}_y^2-\hat{S}_x^2) + (E_y+\delta_y)(\hat{S}_x\hat{S}_y+\hat{S}_y\hat{S}_x)\Big],\end{aligned} \tag{3.2}$$

where γ_e and γ_N are the electronic and nuclear gyromagnetic ratios, $\mathbf{B}$ is the magnetic field, (E_x, E_y, E_z) are the electric-field components, and $\delta = (\delta_x, \delta_y, \delta_z)$ is an effective electric field that models local crystal strain. The term $\gamma_e\,\hat{\mathbf{S}}\cdot\mathbf{B}$ is the electronic Zeeman interaction: it shifts and (for an axial field) splits the ODMR resonances. $\gamma_N\,\hat{\mathbf{I}}\cdot\mathbf{B}$ is the nuclear Zeeman term and gives small corrections to the hyperfine structure. $d_{\mathrm{gs}}^{\parallel}$ and $d_{\mathrm{gs}}^{\perp}$ quantify the ground-state Stark response: the longitudinal part $(E_z+\delta_z)$ shifts the overall splitting (an effective change in D_{gs}), while the transverse part $(E_{x,y}+\delta_{x,y})$ mixes and lifts the degeneracy of $|m_s=\pm1\rangle$ even at $B=0$, producing the small extra splitting often seen in ODMR spectra.

This compact model clarifies the ODMR phenomenology. The parameter D_{gs} is temperature dependent, so a small change ΔT produces a shift $\Delta D_{\mathrm{gs}} = (\partial D_{\mathrm{gs}}/\partial T)\Delta T$ (at room temperature $\partial D_{\mathrm{gs}}/\partial T$ is typically negative and of order 75 kHz/K). A magnetic field along the NV axis ($B_{\parallel}$) separates the $m_s=\pm1$ levels by $\approx 2\gamma_e B_{\parallel}$ (for small transverse mixing), while transverse fields/strain introduce a small offset and mixing. For many continuous CW-ODMR measurements on a single orientation and nearly axial field, the two principal resonances are well approximated by:

$$f_{\pm} \simeq D_{\mathrm{gs}}(T) \;\pm\; \sqrt{\left(\gamma_e B_{\parallel}\right)^2 + E_{\mathrm{eff}}^2}, \tag{3.3}$$

where E_{eff} summarizes the transverse Stark/strain mixing from Eq. (3.2). Together with the hyperfine triplet of ^{14}N, this minimal description captures the spectra used in practice to extract temperature, magnetic field, and local strain in a quantitative and calibratable way [11].

3.2 Optically Detected Magnetic Resonance

ODMR is a way to read out a spin resonance using light. Under green excitation, an NV^- center emits red PL, but the brightness depends on its spin state: $|m_s = 0\rangle$ state is relatively bright, while $|m_s = \pm 1\rangle$ are fainter because they may relax through non-radiative paths. If a microwave (MW) field is applied and its frequency matches the energy gap between these spin states, population is driven into the fainter states and the PL drops (Fig. 3.5a), resulting in a dip in the plot of PL vs MW frequency. This dip reveals the spin resonance. In a zero magnetic field it appears near D_{gs}. Magnetic fields split and shift it, while temperature, electric fields, and strain produce smaller shifts (Fig. 3.5(b,c)). By tracking the dip position and depth, one can measure these quantities quantitatively [11, 33, 34, 50, 51]. ODMR can be performed in continuous-wave mode or with pulsed sequences for higher precision.

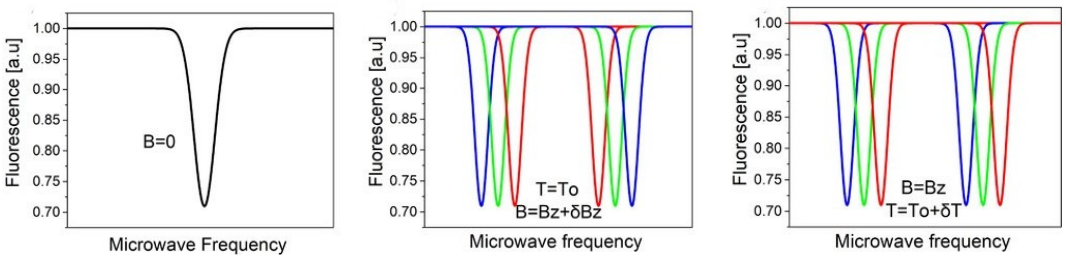

(a) B=0 (b) $T = T_0$, $B_z + \delta B_z$ (c) $B = B_z$, $T = T_0 + \delta T$

Fig. 3.5 ODMR and field-related effects [7]. The schematic shows the ODMR spectrum under different conditions: **panel (a)** shows the spectrum at zero magnetic field, **panel (b)** illustrates the splitting of the spin states induced by an applied magnetic field, and **panel (c)** shows the overall shift of the spectrum under different temperatures.

3.2.1 Continuous-Wave ODMR

One of the most useful features of NV^- is its spin-dependent fluorescence under optical excitation, arising from different ISC rates for $|m_s = 0\rangle$ and $|m_s = \pm 1\rangle$. In a CW-ODMR experiment, the diamond is illuminated with a non-resonant green laser (e.g., 532 nm) while a MW field is swept across the ground-state spin transition. When the MW frequency matches the $\sim$2.87 GHz zero-field splitting between $|m_s = 0\rangle$ and $|m_s = \pm 1\rangle$, population is transferred into the $|m_s = \pm 1\rangle$ states, reducing fluorescence due to enhanced ISC [11, 34]. This fluorescence profile as a function of MW frequency constitutes the ODMR spectrum (Fig. 3.6).

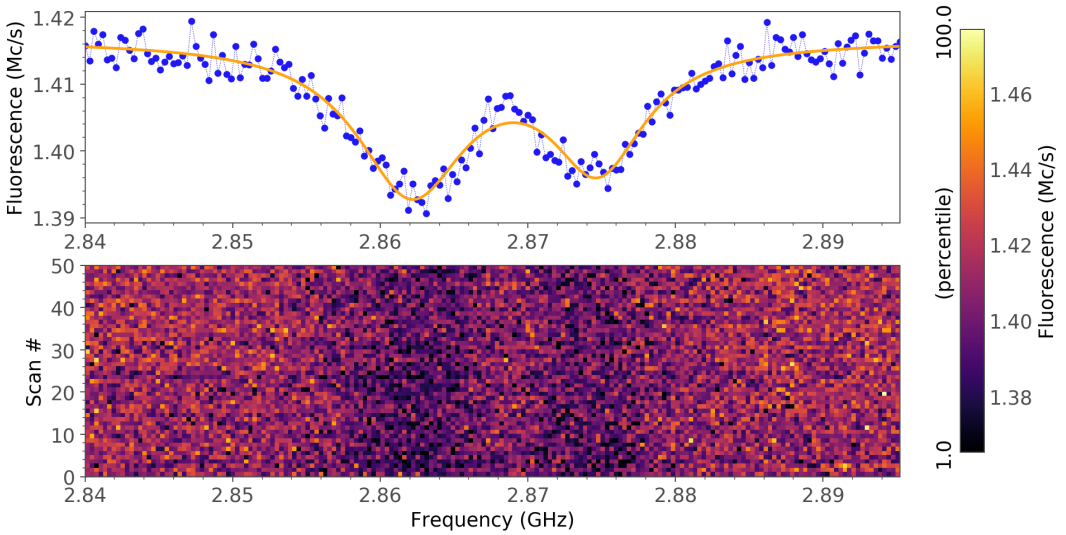

Fig. 3.6 Example of an ODMR spectrum. The figure shows typical fluorescence contrast dips at the resonance frequencies corresponding to NV spin transitions: **panel (a)** displays the spectrum averaged over the acquisition time, while **panel (b)** shows the matrix of individual scans.

The ODMR signal can be modeled as:

$$I(f) = R\left[1 - C \cdot \mathrm{f}\left(\frac{f - f_0}{\mathrm{FWHM}}\right)\right] \tag{3.4}$$

where $I(f)$ is the detected fluorescence, R the baseline count rate, C the contrast, f typically a Lorentzian-like function, f_0 the resonance frequency (equal to D_{gs} in zero field), and FWHM the full width at half maximum of the dips.

In our treatment we will focus on the temperature effect on ODMR.

A shift in the resonance frequency, ΔD_{gs}, can be related to a temperature change via

$$\Delta T = \frac{\Delta D_{\mathrm{gs}}}{\partial D_{\mathrm{gs}}/\partial T} \equiv \frac{\Delta D_{\mathrm{gs}}}{\gamma_T}, \tag{3.5}$$

while magnetic or electric field variations can be extracted by substituting the appropriate derivatives [49, 53, 8]. Accurate determination of D_{gs} requires fitting the ODMR data and often long acquisition times to improve the signal-to-noise ratio, limitations that motivate faster or differential ODMR schemes for dynamic measurements.

3.2.2 Differential ODMR technique

To overcome the limitations of long integration times in traditional ODMR, especially in biological applications, where phototoxicity must be minimized, a differential ODMR approach can be adopted. This method allows for faster estimation of small shifts in the resonance frequency D_{gs}, and hence in physical parameters like temperature or magnetic field [8].

The differential ODMR procedure consists of the following steps:

- Acquire a full ODMR spectrum once under well-defined reference conditions;
- In post-processing, construct a differential spectrum by computing the fluorescence difference between two frequencies around each point, separated by $\pm f_{\mathrm{dev}}$ (see Fig: 3.7):

$$D(f) = I(f + f_{\mathrm{dev}}) - I(f - f_{\mathrm{dev}})\,; \tag{3.6}$$

- The differential signal $D(f)$ becomes zero at the resonance $f = D_{\mathrm{gs}}$ and varies approximately linearly with small shifts ΔD_{gs} near that point (see Fig. 3.8):

$$\Delta D \approx \mathrm{m} \cdot \Delta D_{\mathrm{gs}}\,; \tag{3.7}$$

- Once the slope (m) is known (from the differential spectrum), one can monitor D at a single frequency within the linear region, enabling real-time sensing:

$$\Delta T = \frac{\Delta D}{\mathrm{m} \cdot \partial D_{\mathrm{gs}}/\partial T} = \frac{\Delta D}{\mathrm{m} \cdot \gamma_T}\,. \tag{3.8}$$

Figure 3.7 illustrates the principle of the differential spectrum: while the standard ODMR dip provides a minimum, the differential version offers a zero crossing and a linear response to frequency shifts, allowing for more robust and rapid estimations.

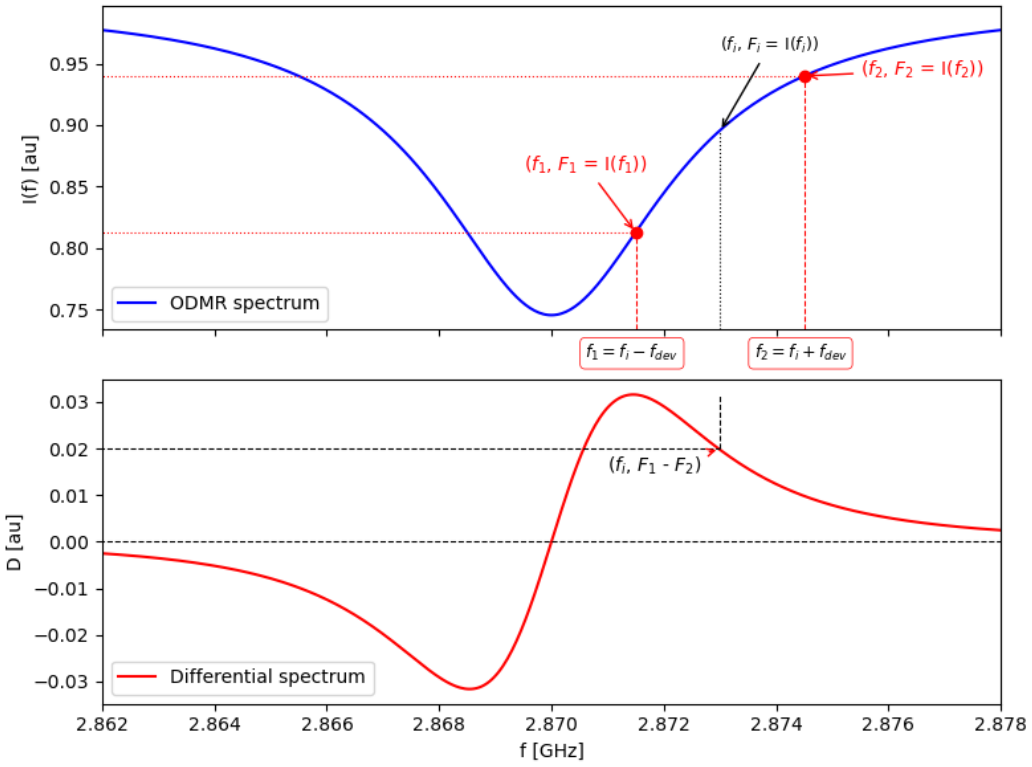

Fig. 3.7 Sketch of the differential measurement. The differential spectrum (bottom) is obtained from the ODMR spectrum (top) by computing, for each microwave frequency, the fluorescence difference between two points separated by a fixed deviation. The linear region around the resonance is used to estimate frequency shifts.

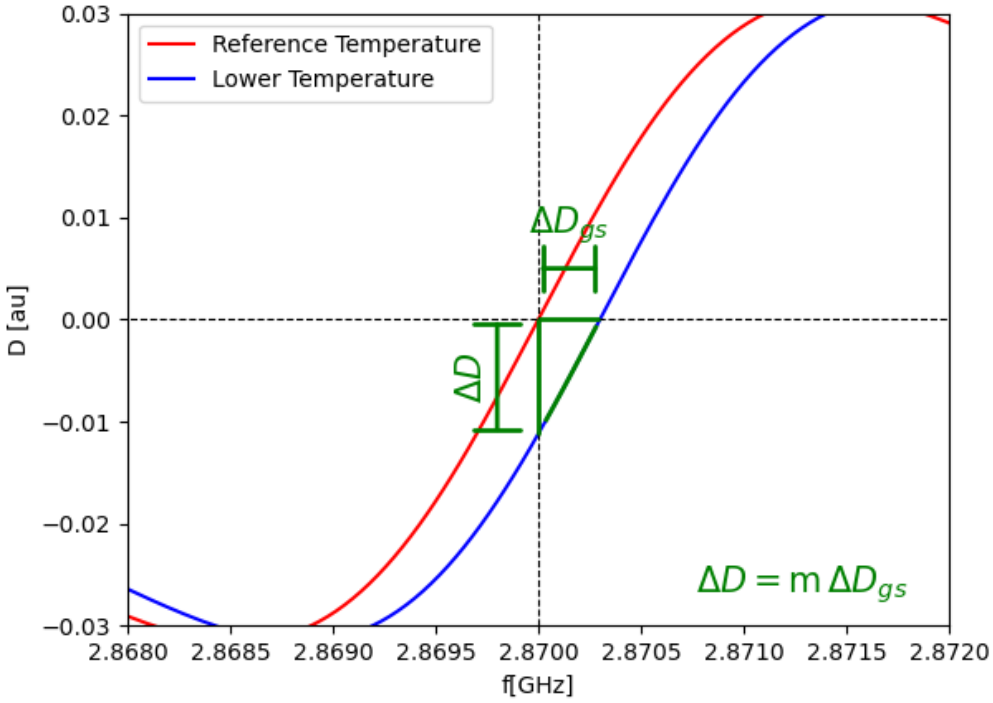

Fig. 3.8 Zoom on the linear region of the differential spectrum. The plot shows the portion of the curve where fluorescence changes linearly with the shift in resonance frequency.

This method is particularly well-suited for applications requiring minimal exposure (e.g., live-cell imaging or real-time thermometry), as it significantly reduces the laser and MW duty cycle while maintaining measurement sensitivity.

3.2.3 Pulsed ODMR

In contrast to CW-ODMR, pulsed ODMR separates the optical pulse, to initialize and readout the spin state, from the MW control. Usually, a short green pulse first polarizes the spin into $|m_s = 0\rangle$ and then a sequence of MW pulses drives the spin coherently. A brief readout pulse finally converts the spin state into PL. By avoiding continuous illumination during the spin manipulation, pulsed schemes reduce power broadening and often give higher contrast and narrower effective linewidths, which can improve sensitivity [49–51].

Before introducing the pulse sequences, it helps to picture the NV spin on a Bloch sphere (Fig. 3.9). In a small axial magnetic field, the ground state can be treated as an effective two-level system spanned by $|m_s = 0\rangle$ and one of $|m_s = \pm 1\rangle$. On the Bloch sphere, the north pole is $|m_s = 0\rangle$, the south pole is the chosen $|m_s = \pm 1\rangle$, and the equator contains equal superpositions with a well-defined phase. Under green laser light, the spin is prepared near the "north" pole. A resonant MW field then rotates the Bloch vector around an axis set by the MW phase. On this sphere, the quantum state is denoted $|\psi\rangle$, geometrically, it appears as the corresponding Bloch vector whose tip lies on the unit sphere. The polar angle, θ, encodes the population balance between the two levels, while the azimuthal φ angle sets their relative phase.

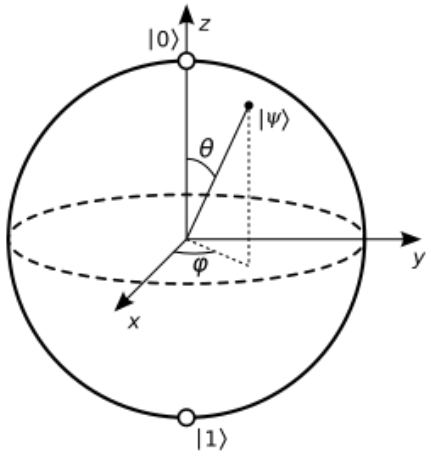

Fig. 3.9 Representation of a state on the Bloch sphere. The diagram visualizes a generic quantum state and its evolution under microwave driving.

A MW pulse acts thus like a short controlled rotation. Its rotation angle grows with pulse power and duration. A $\pi/2$ pulse rotates the state by 90° from the pole to the equator, creating a superposition. A π pulse rotates by 180°, swapping the populations of the two levels.

In the pulse sequence a delay τ appears, which denotes the free-precession time with the MW off: during τ the Bloch vector precesses around z and accumulates phase due to any detuning or external signal (e.g., a small magnetic field). By choosing pulse phases (rotation axes) and delays (phase accumulation), small frequency shifts can be converted into measurable changes of photoluminescence at readout.

Common pulse sequences include:

- **Rabi oscillations** ($\pi/2$–t) (Fig. 3.10a): used to calibrate $\pi/2$ and π pulse lengths and to set the MW amplitude via the Rabi frequency. This is a basic tool to tune the MW drive before sensing.

- **Ramsey interferometry** ($\pi/2$–τ–$\pi/2$) (Fig. 3.10b): measures the free precession of the spin and provide both the resonance frequency (via the fringe frequency) and T_2^* (via the decay of the fringes). It is used to track slow or DC shifts such as temperature-induced changes of $D_{\mathrm{gs}}(T)$ or small quasi-static magnetic fields [33, 50].

- **Hahn echo** ($\pi/2$–τ–π–τ) (Fig. 3.10c): refocuses inhomogeneous dephasing and reveals the coherence time T_2. It also acts as a narrow band-pass for AC fields near $1/(2\tau)$, improving magnetic sensitivity in noisy environments [50, 51].

- **Dynamical decoupling** (e.g., CPMG, XY8): extends coherence by applying many π pulses, offering stronger noise filtering and higher sensitivity to oscillating signals in a chosen frequency band. This is widely used for nanoscale AC magnetometry and spin-noise spectroscopy [51].

In practice, pulsed ODMR can achieve linewidths limited by the lifetime or by the spin coherence and often yields higher sensitivity than CW-ODMR. The trade-off is greater experimental complexity: fast pulse electronics, precise timing, and careful balancing of duty cycle and photon budget.

Although pulsed ODMR was not employed in this thesis, it is an important and complementary technique for NV-based sensing and is a natural route for future improvements under bio-compatible power levels.

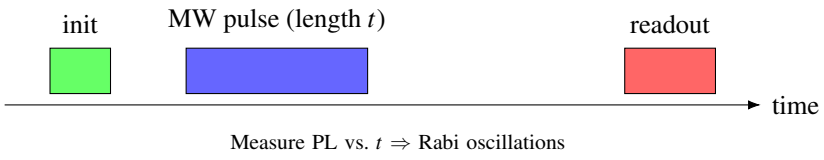

(a) Rabi sequence: calibrates $\pi/2$ and π pulses from the Rabi frequency.

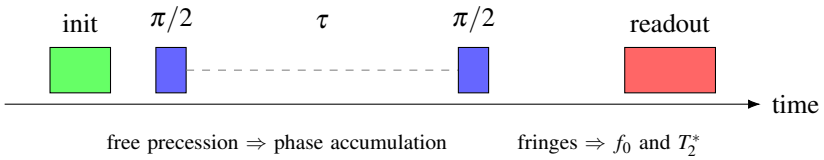

(b) Ramsey sequence: measures resonance frequency and T_2^*.

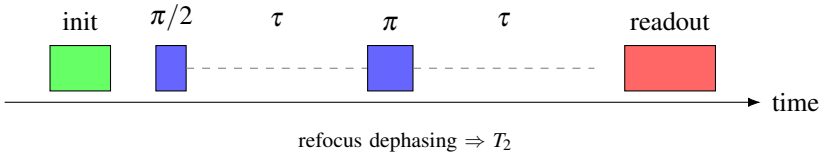

(c) Hahn echo: refocuses dephasing and yields T_2.

Fig. 3.10 Timing diagrams for (a) Rabi, (b) Ramsey, and (c) Hahn echo experiments on NV centers. Green bars indicate optical initialization, red bars the readout, which measures the spin state populations that evolve during the preceding microwave and free evolution periods, blue bars denote microwave pulses, and dashed segments mark free evolution periods. The figure summarizes the main spin manipulation sequences used in quantum sensing.

Chapter 4

Quantum Biosensing with NV Centers in Diamond

Living systems generate weak magnetic, electric, and thermal signals during normal function. Reading these signals at small scales and in real time can reveal how cells work and communicate. As explained in Chap. 3, the NV^- sensor in diamond allows optical readout of a quantum spin at room temperature, it is photostable and biocompatible, and it can work close to cells [49, 51, 54].

In this chapter, we first present the background of classical electrophysiology and magnetometry and the interest in quantum sensors, then we describe practical implementations that use NV centers for neuronal magnetic sensing and for intracellular thermometry, including options based on widefield chips, nanodiamonds, and integration with AFM tips. Finally we discuss sensitivity targets, noise sources, experimental choices, and realistic milestones.

4.1 Background and NV approaches for biosensing

Electrophysiology is the study of electrical signals of biological cells and tissues. Typical techniques measure voltages or currents directly at the cell membrane or nearby, to probe ionic or axial currents.

In the following we quickly review the main methods used to probe cells and we clarify what quantities they measure.

Patch clamp and MEA. Patch clamp [55] is the gold standard for single cell electrophysiology, it measures current or voltage across a the membrane or limited to a membrane patch with sub millisecond time resolution and current resolution in the *pA* range, but it is invasive and the cell is irreversibly damaged after the measurement [56]. Microelectrode arrays [57, 58], also called MEA, record the activity of cells at the same time in a non invasive way, they measure extracellular voltages and thus give indirect information on currents. The readout is an average signal over the electrode area and thus the resolution is above the single cell level. Typical electrodes are 10–30 μm wide and made of Ti or ITO [58, 59]. CMOS MEA increase density and pair well with optogenetics, however geometry still limits spatial resolution and the view is discrete [60–62].

Other sensitive probes. Magnetometers like SQUIDs reach the fT range but need cryogenic conditions and large pickup areas [63, 64]. Chip scale atomic magnetometers work at room temperature but have a sensor–sample distance on the order of millimetres [65]. Both probes are not ideal when the source is a single cell or part of this (axon) because the magnetic field drops fast with distance [66, 67, 65]. For electric fields, single electron transistors (SET) are very sensitive, but they usually need low temperature, for this reason room temperature biosensing is still limited [68, 69].

Table 4.1 Representative biorelevant sensors and typical constraints. The table summarizes main sensors and experimental limitations for biological applications.

Sensor	**Sensitivity**	**Working distance**	**Notes**
SQUID magnetometer	0.9–1.4 fT $\mathrm{Hz}^{-1/2}$	cm	Cryogenic, large WD [66, 67]
Chip scale atomic magnetometer	< 5 fT $\mathrm{Hz}^{-1/2}$	mm	Room temperature, compact optics [65]
NV ensemble, widefield	$\sim$ pT $\mathrm{Hz}^{-1/2}$	μm to contact	On chip imaging [70, 51]
Single NV, nanoscale	nT to μT $\mathrm{Hz}^{-1/2}$	nm	Near field probe [71, 72]
SET electrometer	$\ll 1\,e$ $\mathrm{Hz}^{-1/2}$	nm to μm	Often low temperature [68]

Most physical details on NV centers and ODMR are discussed in Chap. 3, here we focus on what is needed to choose measurement approaches for biosensing and to place the sensor close to living samples.

To perform sensing with diamond two different approach are available: widefield or nanoscale imaging a and sensing.

Widefield imaging uses a thin NV layer near the surface and a camera to record photoluminescence while sweeping the microwave frequency, it works in liquid and gives maps over tens to hundreds of micrometers at once.

Nanodiamond based sensing uses small particles that attach to membranes or get internalized. Their better positioning in proximity of the target cells improves the detection of the signal, but readout is local and calibration depends on particle properties, in practice one can calibrate many particles under the same conditions and report a statistical mean and its uncertainty for the sample [34, 54, 51, 73]. A further option is to integrate the NV sensor on scanning tips, for example diamond nanopillars or nanoneedles mounted on AFM tips. This enables controlled approach to membranes and sub 100 nm positioning while imaging the sample topography. This approach is slower than camera-based widefield imaging but it increases spatial resolution and helps correlating magnetic maps with structural features.

4.2 NV magnetic readout: from signals to experiments

Neurons generate action potentials that travel along axons, a schematic representation of mammalian neurons is presented in Fig. 4.1. When ion channels open, ions cross the membrane and axial currents flow inside the channel. These currents create small magnetic fields (see Fig. 4.1), but the field drops quickly with distance. For this reason proximity is crucial for detecting these signals and, it is therefore useful to estimate the signal amplitude we expect at a certain distance and the sensitivity needed to detect it.

To estimate the amplitude of the electromagnetic fields produced by an action potential (AP, representation in Fig. 4.2), and thus the sensitivity that an NV sensor must reach, we first need a model for how the AP starts and propagates.

The Hodgkin–Huxley framework allows us to estimate the ionic current that crosses the membrane when ion channels open [74, 75]. For a human neuron, a representative total transmembrane current density (sum of many single-channel

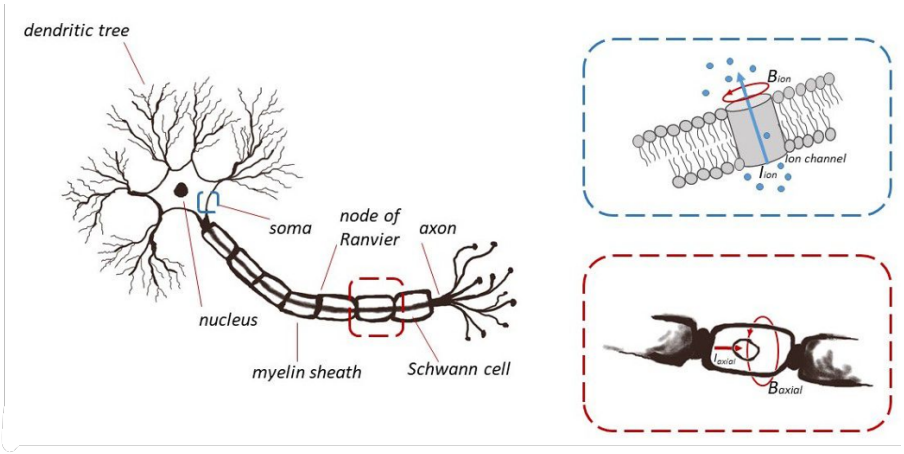

Fig. 4.1 Neuron schematic showing soma, axon, nodes of Ranvier, and myelin sheath [7]. The panels on the right depict the local magnetic field around a single ion channel (top) and the axial field along an active axon segment (bottom), illustrating how neuronal currents generate detectable magnetic signals.

contributions) is [76]

$$I_{\perp} \simeq (1-10)\ \mathrm{pA}\,\mu\mathrm{m}^{-2} \tag{4.1}$$

with a pulse duration of about

$$\Delta t \simeq 1\ \mathrm{ms} \tag{4.2}$$

Each local ionic current produces a magnetic field that can be estimated with the Biot–Savart law. In integral form, the line integral of the magnetic field along a closed loop is proportional to the enclosed current, and for a straight segment one can write

$$\oint \mathbf{B} \cdot d\ell = \mu_0 I_{\mathrm{ion}}. \tag{4.3}$$

The net amplitude, however, depends on how many channels are open, on their surface density, and on their spatial arrangement. Because vector directions differ, individual contributions can partially cancel, conversely, clustering can amplify the local field [77, 78]. As a guideline, if the local current density reaches $\sim$ 100 pA/μm^2 and an NV sensor is positioned a few nanometres from the membrane (e.g., by targeting functionalised nanodiamonds [79, 73]), near-field values of order $0.1-5$ nT (or higher) are plausible in the immediate vicinity of active channels.

Currents are not only transverse. Longitudinal (axial) currents flow along the axon to support AP propagation and also generate a magnetic field encircling the fiber. Compartment models that resolve nodes of Ranvier and myelinated segments predict peak axial fields of about [80–82] $B_{\text{axial}} \simeq 3$ pT on the outer membrane near a node, and $B_{\text{axial}} \simeq 2.3$ pT, on the external surface of the myelin sheath. In bundles, superposition can reduce the net signal: for a nerve made of ~ 100 axons carrying currents in partly opposite directions, maximum fields of only a few pT (e.g., ~ 6 pT) are expected at an external point [82]. These picotesla values are consistent with the scale of fields detected in magnetoencephalography (MEG) once the centimetre-scale stand-off is considered [83].

Based on these numbers, an NV sensor placed on the membrane or a few micrometres away should sample on a sub-millisecond timescale to follow the AP rising ramp (a practical target is $\Delta t \simeq 0.1$ ms). Considering that a sensing volume of order $V \sim 10\ \mu\text{m}^3$ is sufficient to map propagation along typical axons, the corresponding sensitivity requirement, expressed as a noise spectral density, is [84]

$$\eta_{req} = \delta B_{\min}\sqrt{\Delta t} \simeq 3\ \text{pT}\sqrt{0.1\ \text{ms}} \approx 30\ \text{fT}\,\text{Hz}^{-1/2}, \tag{4.4}$$

which sets a demanding target for single-axon measurements.

Note that η_{req} is not a property of the sensor, it is the performance we need for a good signal-to-noise ratio in one sample at that bandwidth.

Independently of this target, the sensor has a fundamental limit set by spin projection noise [85]:

$$\eta_q \approx \frac{1}{\gamma_e}\frac{1}{\sqrt{n\,T_2^*}} \tag{4.5}$$

where γ_e is the electron gyromagnetic ratio, n is the number of NV centers that contribute within the sensing volume, and T_2^* is the inhomogeneous dephasing time. For a volume of $\sim 10\ \mu\text{m}^3$ and typical T_2^* values, η_q is often in the tens of $\text{pT}\,\text{Hz}^{-1/2}$ [86]. This tells us what the material and the NV statistics allow in the best case.

In real experiments the achieved sensitivity with continuous-wave ODMR is well described by [51]:

$$\eta_{\text{cw}} \approx \frac{\Delta\nu}{C\,\gamma_t\sqrt{R}} \tag{4.6}$$

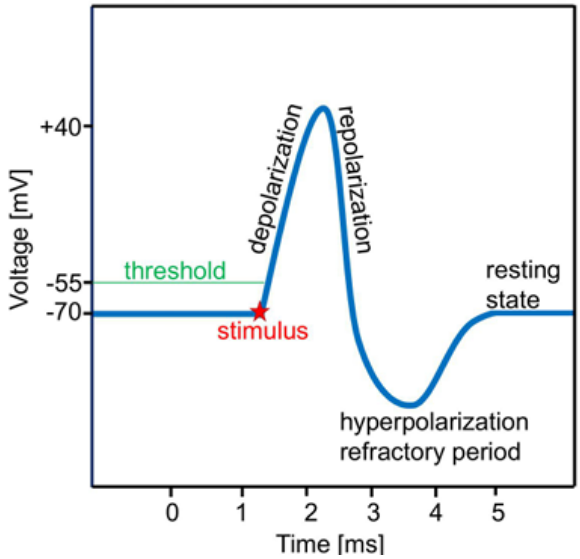

Fig. 4.2 Typical action-potential waveform with threshold, depolarization, repolarization, and after-hyperpolarization phases. The $\sim$0.5–1 ms rising phase motivates the sampling step $\Delta t \approx 0.1$–0.2 ms used in sensitivity estimates.

with $\Delta\nu$ the ODMR linewidth, C the contrast, and R the detected photon rate. Power broadening, technical noise, and limited photon collection often make η_{cw} a factor 2–10 above η_q. In practice we first compute η_{req} from B_{AP} and Δt according to eq. 4.4, then we evaluate the limit set by the material η_q from n and T_2^*, and finally we tune optics and readout to push the operational value η_{cw} down toward η_q. Increasing n and T_2^* helps the fundamental limit, while narrowing $\Delta\nu$, increasing C, and collecting more photons R improve the achieved sensitivity.

During experiments, several noise sources are present: photon shot noise sets a floor that scales as $1/\sqrt{R}$, laser amplitude drift moves the baseline, microwave power fluctuations broaden the resonance, magnetic noise from surface spins shortens T_2^*, and sample motion blurs the images. Table 4.2 lists these sources and common mitigation steps.

Reaching good sensitivity while keeping cells healthy means balancing proximity to the neurons, material quality of the diamond, and soft optical and microwave stimulation. The aim is to increase the signal at the sensor and lower the noise without stressing the biological sample.

On the material side, a longer T_2^* and a sufficient NV density help because the noise floor decreases with coherence time and with detected photons. Very shallow

Table 4.2 Simple noise budget and practical countermeasures for widefield NV magnetometry in cell culture. The table outlines dominant noise sources and mitigation strategies to improve magnetic sensitivity in biological environments.

Noise source	**Effect**	**Mitigation**
Photon shot noise	Sensitivity $\propto 1/\sqrt{R}$	Higher NA, better collection, thicker NV layer [51]
Laser amplitude noise	Baseline drift	Intensity stabilization, ratiometric imaging
Microwave power noise	Line broadening	Pulse sequences [70]
Surface magnetic noise	Shorter T_2^*	Surface termination, gentle cleaning
Sample motion	Imaging blur	Shorter frames, tracking [54]

NV layers improve proximity to neuronal currents, however near-surface defects and adsorbates reduce coherence because of magnetic noise that shortens T_2^*, so depth and surface chemistry must be chosen together. In practice, isotopic purification, controlled or implantation with proper annealing, and clean oxygen termination reduce surface spins and keep cells comfortable, hydrogen termination can help conductivity for microwave delivery but is less stable and can introduce drift and noise, so it needs passivation and careful handling [87]. For these reasons many bio chips use a near-surface NV layer of about 5–20 nm with oxygen termination and a moderate NV density to avoid excess background.

On the optics and microwave side, higher optical power increases contrast and photon counts, but it can heat and stress cells, so experimentally it is better to prefer the lowest power that keeps a stable contrast, expand the beam to lower the intensity per unit area, and limit the duration of the exposure time. Microwaves should be duty-cycled when possible, placing the wire at few millimeters from the sample. A simple safety check is to monitor the zero-field splitting D_{gs} without stimulation and verify that it does not drift with optical or microwave power [51, 88].

A practical workflow is the following. Grow neurons on oxygen-terminated diamond, use coatings like poly-D-lysine if needed, align a small bias field along one NV axis, and set the microwave on the slope of the ODMR curve so that frequency shifts convert into intensity changes. First record reference frames without stimulation to estimate noise and remove fixed patterns, then apply the stimulus and compute difference or ratio maps, this differential mode cancels slow drifts and reveals weak features [51, 54].

A magnetic map $\mathbf{B}(\mathbf{r},t)$ does not determine a single current pattern, because different current distributions can produce similar fields. To obtain a meaningful estimation, simple assumptions that match the sample are introduced (for example, an axon running parallel to a plane at a known depth), together with constraints from imaging (axon path and size) and from electrodes (boundary conditions). A simple forward model (for example, a straight line current at a given depth or a thin dipole sheet) is fitted to the measured $\mathbf{B}$ to estimate a small set of parameters, typically current amplitude, depth, and lateral position. The residuals, defined as the difference between measured and model fields, are then inspected to check consistency, if they remain small and structureless, the estimate is accepted, otherwise the model is adjusted [89, 90].

4.3 NV thermal readout: from signals to experiments

In this thesis we are interested in the use NV-based thermometry as the main tool to quantify intracellular temperature, because it can provide measurement of temperature changes after calibration.

The interest, in particular in biosensing, is justified by the fact that temperature controls channel kinetics, synaptic release, and metabolism, and several studies report small heat transients linked to activity [8, 91–95]. Other cellular thermometers exist, for example organic dyes and fluorescent proteins [96–99], however they provide qualitative readouts (relative intensity or ratiometric proxies) and do not return an absolute ΔT. Quantum dots are bright and photostable, but biocompatibility remains an issue and the readout is commonly relative rather than absolute [100, 101] (see Tab. 4.3).

With NV centers there are two main routes: ODMR and all-optical protocols.

In ODMR-based thermometry the ground-state splitting D_{gs} shifts with temperature due to lattice expansion and spin–phonon coupling,the ODMR protocol enables absolute or differential temperature in cells with sub-degree precision [102, 103]. In all-optical thermometry with group-IV centers such as SiV, the zero-phonon line shifts with temperature, which avoids using microwaves and can be more compatible with sensitive preparations, the use of this technique in biosensing is growing but fewer reports exist [12] and this method is less mature then the ORMR one. Recent

Table 4.3 Intracellular thermometry options. The table compares available techniques for temperature measurement inside cells. Sensitivity is qualitative, as it depends on calibration and specific experimental protocol.

Probe	**Biocompat.**	**Photostab.**	**Notes**
Organic dyes or FP	High	Limited	Mostly relative readouts, pH/background sensitive [104]
Quantum dots	Medium–low	High	Heavy-metal concern, often relative signal [101, 97]
Nanodiamonds, NV ODMR	High	Very high	Absolute or differential T via $D_{gs}(T)$ [102, 103]
Nanodiamonds, SiV, GeV, SnV ZPL	High	Very high	All-optical readout, fewer bio reports [12, 105]

work combines nanoheaters with nanodiamond readout and reports temperature transients in neurons, showing feasibility and opening questions on heat budgets and diffusion in the cytoplasm [9, 8].

To calibrate the sensor the technique is to measure $D_{gs}(T)$ in buffer while varying temperature in steps with a heater, then fit a linear slope in the temperature range (see Fig. 4.3), keeping the same optical powers used in biological measurements so that any laser-induced self-heating is included in the calibration.

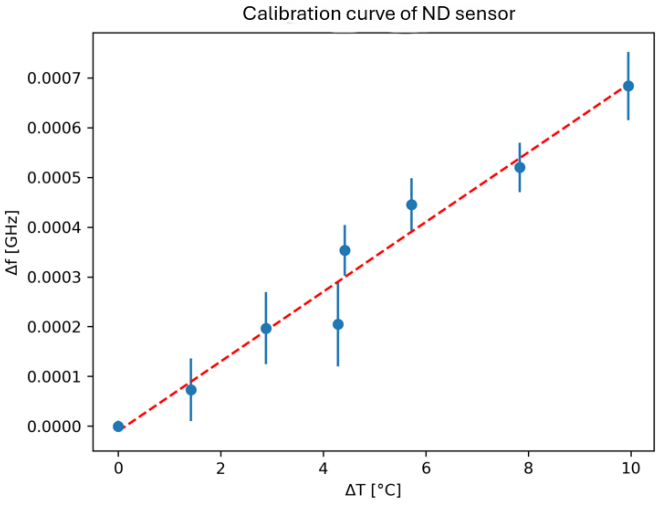

Fig. 4.3 Example of a calibration curve. The plot shows resonance frequency versus temperature, used to extract the thermal coefficient for NV-based thermometry.

In the following, drawing from recent reviews on nanodiamond biosensing [12], the main experimental paradigms relevant to this thesis are reported.

4.3.1 Intracellular nanodiamond thermometry.

NV nanodiamonds were internalized in living cells and used to measure absolute temperature changes after a local $D_{\mathrm{gs}}(T)$ calibration [103]. The method was then applied to neurons, where, after the internalization of NDs (see Fig. 4.4), pharmacological protocols were used to boost or silence network activity, and differential measurement schemes were applied [8]. These experiments revealed fast temperature transients linked to firing, with sub-degree precision at the volume set by the point spread function. Controls checked that D_{gs} did not drift with laser or microwave power, reducing the risk of artifacts.

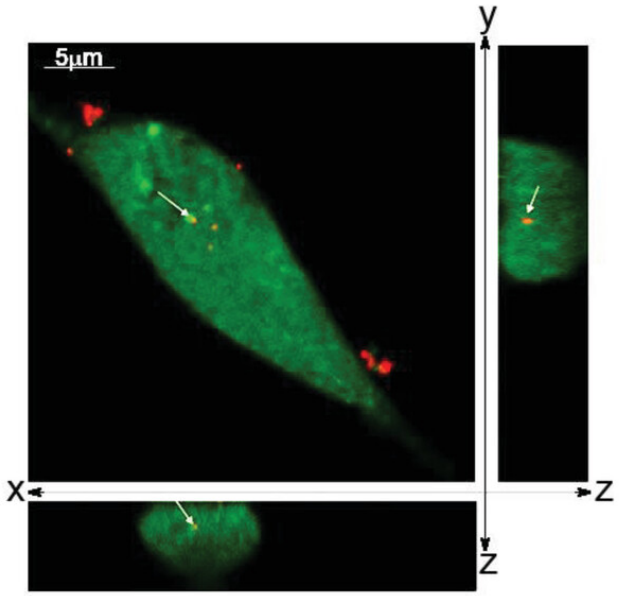

Fig. 4.4 Nanodiamond internalized in a neuron (adapted from [8]). The confocal image demonstrates cellular uptake of the nanodiamond, confirming its biocompatibility.

4.3.2 All-optical thermometry.

NV thermometry was demonstrated without microwaves by tracking optical features such as the Debye–Waller factor, allowing temperature readout with purely optical means [105]. Single-nanoparticle work reported ratiometric readout with a noise floor of about 0.3 $\mathrm{K\,Hz^{-1/2}}$ [106], and later studies used all-optical NV sensing to follow biochemical kinetics with sensitivity around 80 $\mathrm{mK\,Hz^{-1/2}}$ [107]. For group-IV centers, the method tracks near-infrared ZPL shifts: SiV nanodiamonds enabled

ultrasensitive, multiparametric readout and have been used in live-cell imaging, while GeV centers enabled fiber-coupled, implantable thermometry in freely moving mice with $\sim 0.15^{\circ}$C accuracy [108–110]. In all cases, a short in situ calibration and checks on spectral stability are important to ensure reliable ΔT.

Figure 4.5 illustrates examples of all-optical thermometry across different color centers. Panel (a) shows the temperature-dependent spectrum of SiV centers [108], panel (b) shows GeV spectra measured under similar conditions [110], and panel (c) shows NV center spectra [106]. These spectra highlight how shifts in the zero-phonon line or overall emission profile can be exploited to measure temperature at the nanoscale without using microwaves.

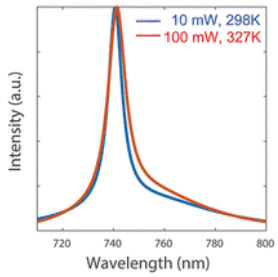

SiV: temperature-dependent spectrum [108].

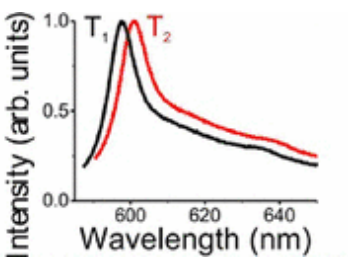

GeV: temperature-dependent spectrum [110].

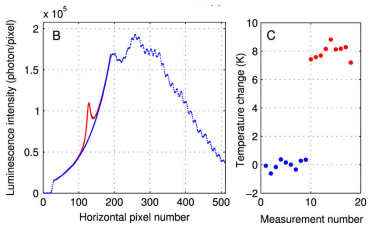

NV: temperature-dependent spectrum [106].

Fig. 4.5 Examples of all-optical thermometry. The figure shows temperature-dependent spectra for SiV, GeV, and NV centers, illustrating how spectral shifts can be used for nanoscale temperature sensing.

4.3.3 Hybrid nanoheater + ND readout.

Gold nanoheaters were co-localized with nanodiamonds, see Fig. 4.6 so that optical excitation produced a controlled heat source while the NV reported the local temperature rise [9]. By changing heater power and timing it was possible to map steady and transient responses and to fit simple diffusion models. The approach was extended to neurons, where activity-linked temperature changes were resolved during real physiological stimulation [8]. Key controls verified the heater–sensor distance, excluded direct ND absorption at the heater wavelength, and repeated the $D_{\mathrm{gs}}(T)$ calibration after the protocol.

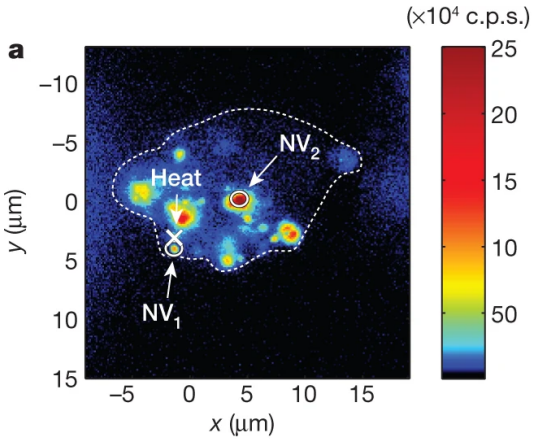

Fig. 4.6 Nanodiamond co-localized with a gold nanoparticle used as a nanoheater (adapted from [9]). The composite image highlights local heating and its detection through NV fluorescence.

Chapter 5

Experimental setup overview

This chapter introduces the experimental platform shared among the activities of my thesis. In particular the chapter summarizes the excitation and detection optics, the mapping system, and the electronic interface, leaving experiment-specific settings to the following chapters.

5.1 Confocal Microscopy for ODMR Measurements

Confocal microscopy enables the optical investigation of photoluminescent systems with high spatial selectivity and depth resolution, which makes it particularly suitable for characterizing NV centers in diamond [111–113]. Optical sectioning is achieved by rejecting out-of-focus light with a spatial filter (a pinhole) placed in front of the detector. A scheme of principle of the confocal setup is provided in Fig. 5.1.

The microscope is dubbed confocal because excitation, sample, and detection planes are optically conjugate. Unlike wide-field microscopy, where an extended area is illuminated at once, the confocal setup illuminates and probes the sample point-by-point, images are built by scanning either the excitation beam or the sample.

To excite NV^- centers, the excitation energy must exceed that of the optical transition. In practice, a green laser is commonly used, typically at $\lambda \sim 532\,\mathrm{nm}$, although the specific excitation scheme depends on the experiment. The beam is collimated and reflected by a dichroic mirror that transmits longer wavelengths while reflecting the green excitation. The reflected beam is focused onto the sample by

a microscope objective, defining the excitation spot at the focal plane. The same objective collects the red-shifted photoluminescence emitted by the NV centers. The emitted light retraces the optical path: it passes through the objective, is transmitted by the dichroic, then spectrally filtered to remove residual green light, and finally reaches the detector. A pinhole blocks out-of-focus contributions, providing axial resolution and enabling optical sectioning [111].

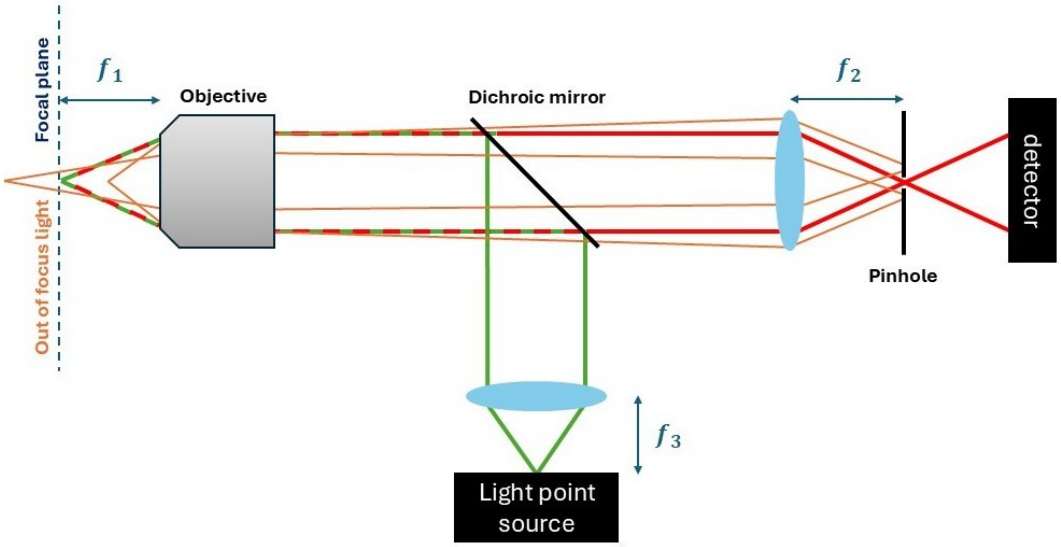

Fig. 5.1 Schematic of a confocal microscope. The pinhole blocks out-of-focus light, improving axial resolution and enabling high-contrast fluorescence imaging.

In our experiments, the NV photoluminescence is typically detected with single-photon avalanche diode (SPAD) modules, which offer high sensitivity and precise timing for ODMR and time-resolved measurements.

Single-Photon Avalanche Diodes (SPADs). SPADs detect single photons by operating a p–n junction in Geiger mode, that is, reverse-biased close to the breakdown region. The absorption of one photon can trigger a self-sustained avalanche that produces a macroscopic electrical pulse, which is then counted by standard electronics. After each detection event the device must be quenched (passively or actively) to stop the avalanche and restore the bias, this recovery sets the dead time and limits the maximum count rate. Because the avalanche amplitude is nearly fixed, SPADs do not resolve the number of photons within one dead-time window, they act as binary "click" detectors. Dark counts arise from thermally generated carriers and increase

with temperature and excess bias, to reduce them, commercial modules are often thermoelectrically cooled. The overall detection efficiency depends on wavelength and device design. In the spectral band relevant for NV emission ($\gtrsim 500\,\mathrm{nm}$), typical modules provide a photon detection efficiency above about 40%, together with low dark-count rates and sub-nanosecond timing jitter, which is adequate for our ODMR and PL measurements.

5.1.1 Spatial Resolution

In optical microscopy, spatial resolution is limited by diffraction (and residual aberrations). While aberrations can be minimized by careful alignment, diffraction sets the fundamental bound.

The point spread function (PSF) describes how a point emitter is imaged. For a point-like source,

$$I(x,y,z) = \delta^3(x_0,y_0,z_0) \otimes \mathrm{PSF}(x,y,z), \tag{5.1}$$

so the image of a point-like source directly reveals the PSF.

At the focal plane ($z = 0$) under the paraxial approximation, the lateral intensity profile is

$$I_p(\rho,0) = \frac{2\,[J_1(v)]^2}{v^2}, \qquad v = \frac{2\pi\rho\, n \sin\alpha}{\lambda}, \tag{5.2}$$

where J_1 is the first-order Bessel function, ρ the radial coordinate, n the refractive index, and α the half-angle of the focused cone.

The lateral resolution can be characterized via the calculation of the Airy radius R_{xy} or its reciprocal η_x

$$R_{xy} = \frac{0.61\,\lambda}{n\sin\alpha} = \frac{0.61\,\lambda}{\mathrm{NA}}, \qquad \eta_{xy} = \frac{1}{R_{xy}}. \tag{5.3}$$

Along the optical axis ($\rho = 0$), an analytical form for the axial intensity near focus is

$$I_p(0,z) = \left[\frac{\sin(u/4)}{u/4}\right]^2, \qquad u = \frac{2\pi z\, n \sin^2\alpha}{\lambda}, \tag{5.4}$$

leading to the axial resolution

$$R_z = \frac{2n\lambda}{\mathrm{NA}^2}, \qquad \eta_z = \frac{1}{R_z}. \tag{5.5}$$

Both R_{xy} and R_z depend on wavelength and numerical aperture (NA), for example, increasing NA (e.g., with oil-immersion objectives) improves resolution [111].

5.1.2 Optical Sectioning

In wide-field fluorescence the camera collects light from many axial planes, so out-of-focus regions add background and the z contrast is poor. In a confocal microscope (Fig. 5.1) a pinhole is positioned in a plane conjugate to the focus and blocks most out-of-focus light. The detected signal then comes mainly from a thin slice around the focal plane, this results in optical sectioning [111–113].

A simple model shows the difference. For a uniformly illuminated plane, the energy recorded by a wide-field system is the integral of the intensity PSF:

$$E_{\text{wide-field}}(z) = \iint \mathrm{PSF}(x,y,z)^2 \, dx\, dy, \tag{5.6}$$

which is nearly constant with z (planes above and below focus contribute similarly). In a confocal microscope, excitation and detection are both spatially filtered, so the effective response scales as PSF^2 in intensity and the collected energy becomes

$$E_{\text{confocal}}(z) = \iint \mathrm{PSF}(x,y,z)^4 \, dx\, dy \;\propto\; z^{-2} \quad (z \gg \lambda), \tag{5.7}$$

which falls quickly when the plane is moved away from focus. This produces thin optical slices and better axial contrast.

The pinhole size is set in Airy Units. About 1 Airy Units is a good compromise: smaller values improve sectioning but reduce photon counts, larger values increase signal but also background. Sectioning improves when the objective has a higher NA and when refractive indices are well matched. Using the objective's correction collar and the proper coverslip thickness helps to reduce spherical aberration.

For NV measurements, sectioning confines readout to the shallow NV layer near the diamond surface, or to a single NDs, and reduces background from the medium, which stabilizes ODMR and thermometry.

5.2 Integration of Multielectrode Arrays for Simultaneous Electrophysiology and Thermometry

In NV-based biosensing experiments it is important to have an independent mean to probe the activity of the cells targeted by the quantum nanosensor. This is provided by a MEA wich was integrated in the confocal setup.

The MEA enables simultaneous acquisition of electrophysiological signals and nanothermometric readouts from neuronal culture. The MEA used in this work is the model 60MEA100/10iR-Ti (Multi Channel Systems, MCS), which offers high temporal resolution and low-noise performance for in vitro recordings [114].

This MEA consists of 60 planar microelectrodes arranged in an 8×8 grid, with diameters typically in the 10–30 μm range and a 100 μm pitch (Fig. 5.2). The electrodes are made of titanium nitride (TiN), selected for biocompatibility, low impedance, and good charge-transfer properties. The chip is fabricated on a glass substrate with an integrated reference electrode and mounted in a 30 mm Petri dish, facilitating integration with inverted optical microscopes.

Each electrode is connected to a high-input-impedance amplifier through a dedicated channel in the MCS headstage, enabling parallel recordings at sampling rates up to ~ 50 kHz per channel. The MEA allows detection of extracellular action potentials (spikes) and spontaneous network activity across neuronal populations cultured on the chip surface. The transparent, planar substrate is compatible with high-NA optical access from below, which is essential for confocal imaging [115].

To integrate the MEA with the confocal microscope, the MCS MEA headstage was mechanically coupled to a piezoelectric XY translation stage mounted on a customized Olympus IX73 microscope. This configuration allows precise co-registration of the optical focal plane with the MEA plane, enabling targeted optical excitation and readout of fluorescent ND sensors in close proximity to active neurons.

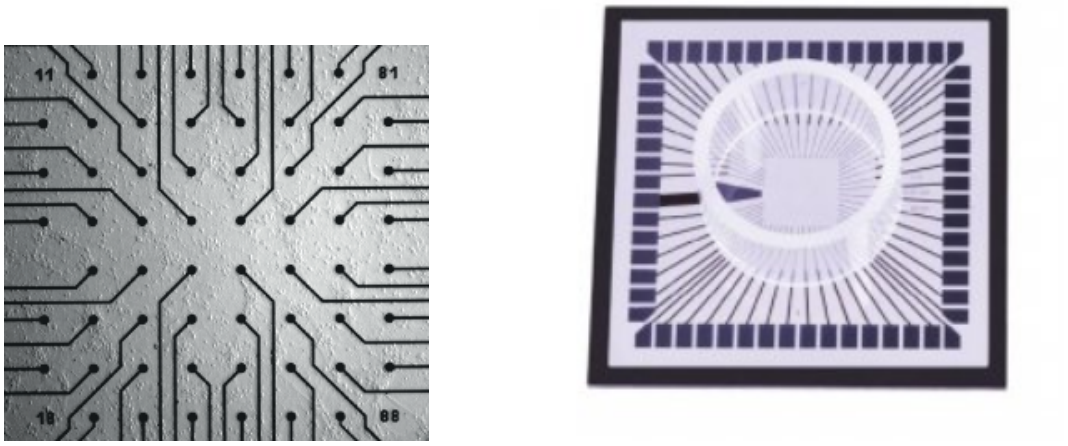

(a) (b)

Fig. 5.2 Electrode grid and MEA chip. Panel (a) shows the electrode layout, and panel (b) displays the corresponding MEA chip used for neuronal recordings.

The combined setup enables time-correlated acquisition of electrical and thermal signals. ND-based ODMR thermometry provides local, real-time temperature readouts via the temperature dependence of the NV zero-field splitting [102], while the MEA captures extracellular electrical activity from individual neurons and networks. The concurrent acquisition of these signals allows investigation of the interplay between synaptic/network dynamics and intracellular temperature fluctuations [9, 8].

In my experimental activity I was involved in the setup of this innovative compound facility for simultaneous neuron firing activity and NV-based thermometry measurement.

Chapter 6

Experiment - Diamond samples engineering

This chapter, together with the following two, focuses on the experimental work I carried out during my three-year PhD at the Istituto Nazionale di Ricerca Metrologica (INRiM), together with my original contributions. The aim is to give a clear and coherent account of the methods, measurements, and results that supported the conclusions of this research.

This chapter (and the following) opens with the scientific motivation and specific goals of the study, then moves to the preparation and processing of the samples. It next describes the measurement setups and the procedures adopted to collect and analyse the data. The central part presents the results, highlighting the main trends and their interpretation in light of the literature. The chapter ends with a concise conclusion that summarises the findings and outlines possible directions for future work for each experiment.

6.1 Effects of Thermal Oxidation and Proton Irradiation on ODMR Sensitivity in Sub-100 nm Nanodiamonds

The first experiment [116] examines how processing can tune nanodiamonds for intracellular sensing. It introduces the study of thermal oxidation and proton irradiation (with annealing) to shrink particle size while preserving ODMR performance, and outlines how surface chemistry and size were linked to photoluminescence and ODMR metrics.

Intracellular NV sensing requires nanodiamonds of extremely small dimension, because smaller particles enhance cellular uptake, can reach narrow biological structures, and allow specific functionalisation. On the other hand, reducing the size of the particle reduces the number of NV centres affecting sensitivity and makes charge state and spin properties more sensitive to surface noise. This trade-off motivated the design of a processing route that preserved, and ideally improved, spin readout while targeting sizes well below 100 nm.

In this chapter we explore two routes to tune surface chemistry and defect density in commercially available HPHT NDs, with the goal of maintaining robust PL and CW-ODMR features at sub-20 nm dimensions.

- **thermal oxidation**, used to clean the surface and tune terminations that stabilise NV^- and photoluminescence,
- **proton irradiation followed by annealing**, used to create vacancies and increase NV density.

We then quantify how these processes affect the NV charge state, PL output, particle size, the ODMR contrast and linewidth, and the thermal sensitivity.

6.1.1 Samples and Processing

In this paragraph we describe how the samples were prepared.

Commercial HPHT nanodiamonds (Pureon MSY 0–0.1, median size ∼55 nm) were employed as the starting material. The full processing route is summarized in Fig. 6.1 and described below in the same order.

- **Step 1 — Annealing in N_2.** Untreated NDs were annealed at 800 °C for 2 h in nitrogen. This converts amorphous surface carbon into graphitic phases and stabilizes the crystal before oxidation (**AnnND**).
- **Step 2 — Air oxidation at 500 °C.** Two oxidation times were used to tune the surface chemistry corresponding to two batches of NDs (listed in bold)
  - 3 h → **Ox**^{low}**ND**, a moderate oxidation that removed the outer defective layer and introduced oxygen terminations while limiting excessive etching,
  - 36 h → **Ox**^{high}**ND**, a longer oxidation that further thinned the particles and increased the density of oxygen-containing groups.

  Oxidation removes sp^2 carbon and adds O-terminations, improving hydrophilicity and favouring the NV^- charge state.
- **Step 3 — Proton irradiation (from Ox^{high}).** A portion of **Ox**^{high} was irradiated with 2 MeV H^+ at two fluences to create vacancies
  - 1×10^{15} cm^{-2} (low fluence),
  - 4×10^{16} cm^{-2} (high fluence).
- **Step 4 — Annealing and re-oxidation.** After irradiation, samples were annealed again in N_2 at 800 °C for 2 h to mobilize vacancies and form NV centers with native nitrogen (∼100 ppm). A final air oxidation consolidated the surface
  - 12 h at 500 °C after low fluence → **Irr**^{low}**ND**, that is, irradiated at 1×10^{15} cm^{-2}, vacancy-activated, and re-oxidised to stabilise the surface,
  - 12 h at 500 °C after high fluence → **Irr**^{high}**ND**, that is, irradiated at 4×10^{16} cm^{-2}, vacancy-activated, and re-oxidised under the same conditions.

In summary, thermal oxidation purifies and functionalises the surface, promoting NV^- over NV^0, whereas irradiation plus annealing increases the number of active

centres. The sequence is designed to keep particles small and dispersible, while remaining bright and spin-stable for ODMR sensing.

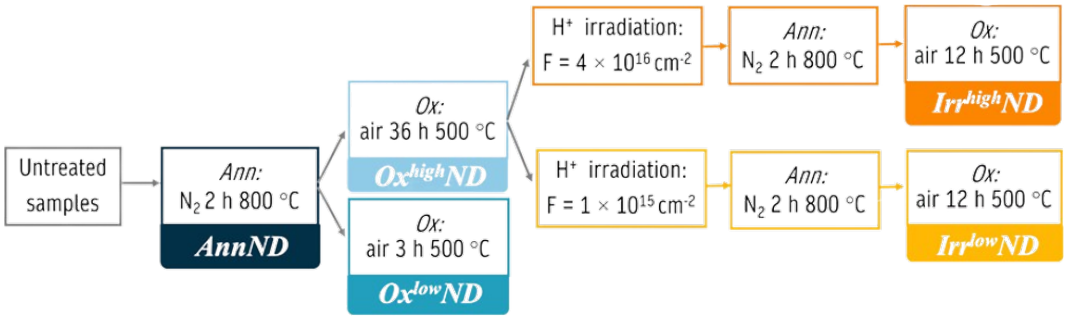

Fig. 6.1 Process flow for annealing, oxidation, irradiation, and post-annealing with re-oxidation. The boxes indicate processing temperatures, durations, and ion fluences used for sample preparation.

6.1.2 Experimental Approach

We evaluated the effect of the treatment on surface chemistry, structure, size and spin readout with a single, coherent protocol. Diffuse Reflectance Infrared Fourier Transform (DRIFT) spectroscopy probes vibrational modes by recording the infrared light that is diffusely reflected by a powdered or rough sample. In this geometry the scattered signal is converted into an effective absorbance, which makes the method sensitive to surface functional groups on nanodiamonds. In our case DRIFT was used to track oxygen-containing terminations created by oxidation. Dynamic Light Scattering (DLS) measures fluctuations of the scattered laser intensity due to Brownian motion, then uses the Stokes–Einstein relation to extract the hydrodynamic diameter. It returns a z-average size and a polydispersity index, so it is well suited to detect aggregation and to compare colloidal stability in water and cellular medium. Increasing O-terminations is desirable because it improves hydrophilicity, promotes colloidal stability in physiological media such as phosphate-buffered saline (PBS), and helps stabilise the NV^- charge state near the surface. Raman spectroscopy monitors the suppression of sp^2 phases (G-band near 1580 cm^{-1}) and the prominence of the diamond line at $\sim$1332 cm^{-1}. Room-temperature PL is integrated over 650–780 nm and decomposed to estimate the NV^-/NV^0 ratio. Size statistics for isolated particles are obtained by Atomic Force Microscopy (AFM) in non-contact mode, using maximum height as a robust metric on the sub-50 nm scale. Finally, single-particle CW-ODMR is performed. Laser power at the sample and the microwave power at the antenna

were kept low to limit power broadening and remain within bio-constraints. ODMR spectra were analysed with double-Lorentzian fits to determine the ODMR contrast (C) and the peak FWHM ($\Delta\nu$). These, combined with the photon rate R, are required to evaluate the shot-noise-limited temperature sensitivity.

6.1.3 Results and Discussion

6.1.3.1 Surface chemistry and dispersion

DRIFT shows the growth of oxygenated terminations upon oxidation, with a clear band near 1780 cm^{-1} and multiple features between 1300 and 1000 cm^{-1}, together with broad O–H absorption from 3700 to 3000 cm^{-1} and an H_2O bend at 1630 cm^{-1} (see Fig. 6.2a). DLS confirms the improvement in dispersibility, oxidised NDs remain stably suspended in water and in PBS, whereas AnnND, richer in C–H terminations, exhibits larger hydrodynamic diameters that indicate aggregation (see Fig. 6.2b).

Aggregation of NDs is undesirable because it reduces diffusion and effectively increases the probe size during biological uptake. From a sensing perspective, oxygen-terminated surfaces favour NV^- stabilisation and mitigate surface-related PL suppression, improving the robustness of ODMR readout.

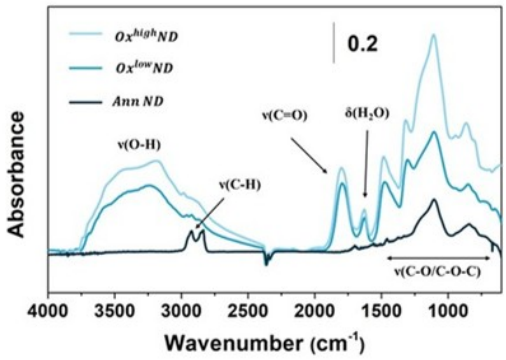

(a) DRIFT spectra before and after oxidation. The growth of carbonyl and C–O features, together with the O–H envelope, indicates oxygenated terminations.

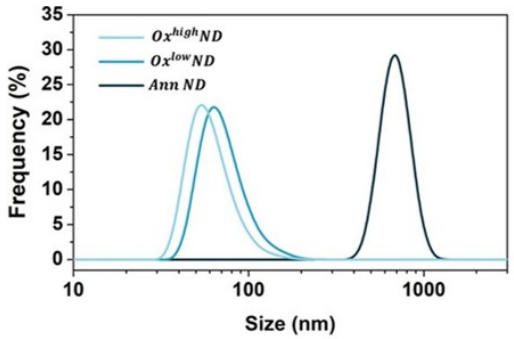

(b) DLS in water. Oxidised NDs display smaller hydrodynamic diameters and narrower distributions than AnnND, consistent with improved colloidal stability.

Fig. 6.2 Surface chemistry and dispersion. DRIFT spectra reveal chemical fingerprints correlating with improved nanodiamond dispersibility measured by DLS.

6.1.3.2 Raman and PL

Oxidation suppresses the sp^2-related G-band near 1580 cm^{-1} and enhances the diamond line at $\sim$1332 cm^{-1}, indicating surface purification. In parallel, the integrated NV emission increases after oxidation and is further increased by irradiation followed by annealing, which is consistent with a higher NV density and reduced nonradiative losses (see Fig. 6.3).

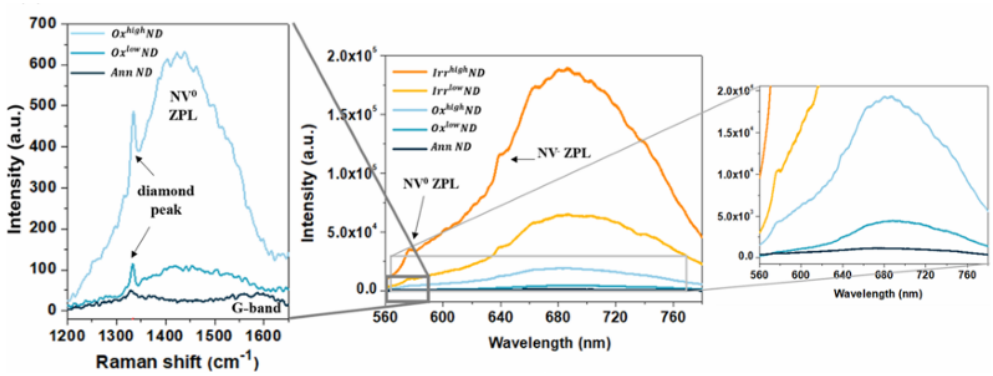

Fig. 6.3 Raman and PL characterization. The Raman spectrum (left) shows G-band removal after oxidation and a sharper diamond peak, while the PL spectrum (right) demonstrates a progressive intensity increase from annealed to oxidized and irradiated samples, integrated over 650–780 nm.

Looking at Fig. 6.4a and Fig. 6.4b we can see that spectral decomposition indicates that $Ox^{low}ND$ (3 h) displays a larger NV^-/NV^0 ratio than $Ox^{high}ND$ (36 h), suggesting that moderate oxidation better stabilises the negative charge state. Irradiation followed by annealing increases brightness, the higher fluence maximises PL, whereas the most favourable NV^-/NV^0 balance is typically observed at intermediate fluence, consistent with the donor–acceptor balance at high defect densities.

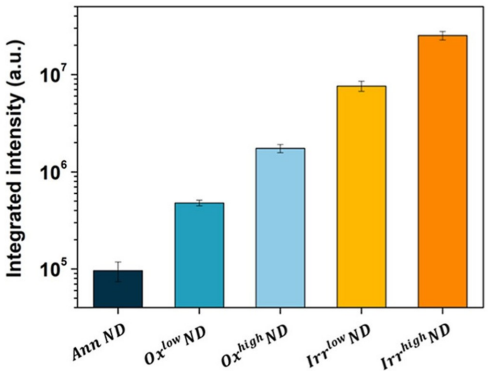

(a) Integrated PL for the different processes. Oxidation enhances emission, and irradiation, particularly at high fluence, provides a further increase.

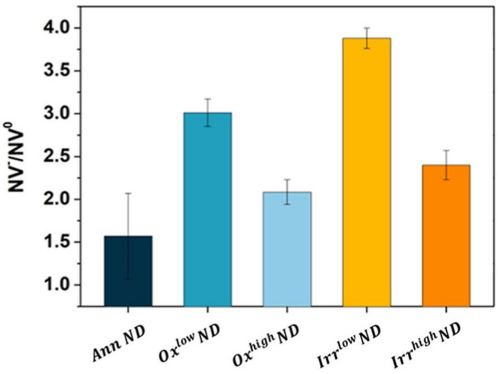

(b) NV^-/NV^0 ratio. Ox^{low}ND exceeds Ox^{high}ND, and an intermediate irradiation level often gives the best balance.

Fig. 6.4 PL intensity and charge-state balance. The plot compares the photoluminescence signal and NV^-/NV^0 ratio for differently treated samples, indicating improved emission with optimized surface termination.

6.1.3.3 Size statistics

AFM confirms progressive size reduction (see Fig. 6.5a). Longer oxidation (Ox^{high}ND) gives smaller particles than Ox^{low}ND, and irradiation followed by annealing and re-oxidation leads to a further decrease. Irradiated batches reach sub-20 nm mean diameters while retaining measurable PL and ODMR. Moreover, the standard deviation became smaller after the full sequence, which indicated more homogeneous samples and translated into more robust measurements and better repeatability across datasets.

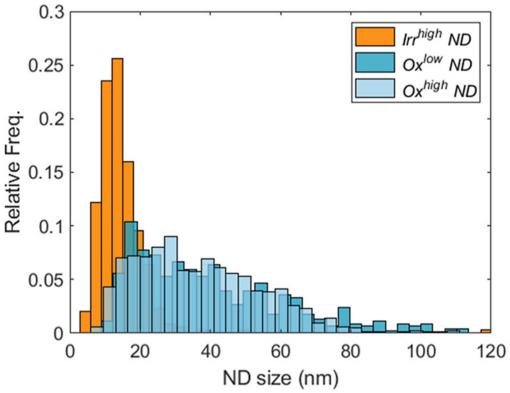

(a) AFM histograms of maximum height for Ox^{low}, Ox^{high} and Irr^{high} batches.

Sample	Average max h (nm)
$Ox^{low}ND$	43.5 ± 1.5
$Ox^{high}ND$	37.0 ± 0.6
$Irr^{high}ND$	18.5 ± 0.4

(b) Summary table with mean ± SD. Irradiated batches approach sub-20 nm averages with reduced dispersion.

Fig. 6.5 Size statistics by AFM on isolated nanodiamonds. The distribution confirms particle sizes ranging from tens to a few hundred nanometers

6.1.3.4 ODMR metrics and sensitivity

Within a multi-institution collaboration, the analysis of ODMR spectra and the evaluation of temperature sensitivity for the processed nanodiamonds was my main contribution during activity in the laboratories at INRIM. The measurement principle and notation is the same as the one presented in Chap. 3.

Experimental setup. A home-built single-photon confocal microscope (see Chap. 5) was used to record PL and CW-ODMR on isolated nanodiamonds (see Fig. 6.6). A continuous-wave 532 nm laser was routed by a dichroic beamsplitter and focused with a 60× air objective (NA 0.9). The optical power at the sample was 100 μW. The same objective collected the PL, which was filtered by a 532 nm notch and a 650 nm long-pass, coupled to a multimode fiber and detected by a silicon SPAD. For ODMR, a microwave source (Keysight N5183B) fed a planar antenna placed near the sample to provide a uniform field in the area of interest. After an initial sweep to avoid power broadening, the same laser and microwave settings were used for all batches for consistency.

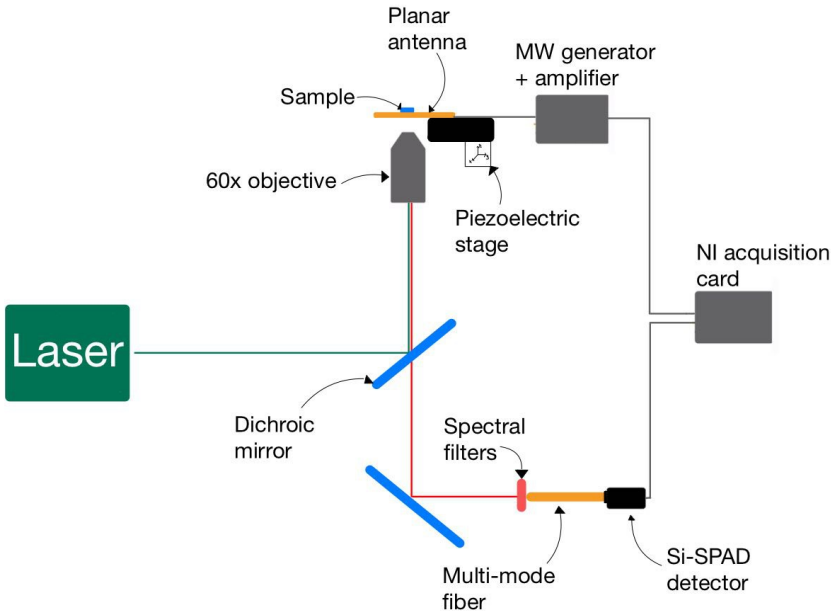

Fig. 6.6 Confocal PL and continuous-wave ODMR setup used for isolated nanodiamonds at INRIM. The schematic shows excitation and detection paths together with the planar microwave antenna.

Experimental procedure. Confocal PL maps were recorded over $(80 \times 80)\,\mu\mathrm{m}^2$ regions (see Fig. 6.7). For each candidate spot we drew a compact ROI around the diffraction-limited emitter, and we estimated the local background. The background-subtracted photon rate was computed as $R = \left(\mathrm{counts}_{\mathrm{ROI}} - \mathrm{counts}_{\mathrm{bg}}\right)/t_{\mathrm{acq}}$. This procedure both corrects for ambient signal and rejects aggregates: spots with elongated profiles, multiple maxima, or an apparent radius larger than ~ 1.5 times the point-spread function were classified as clusters and discarded.

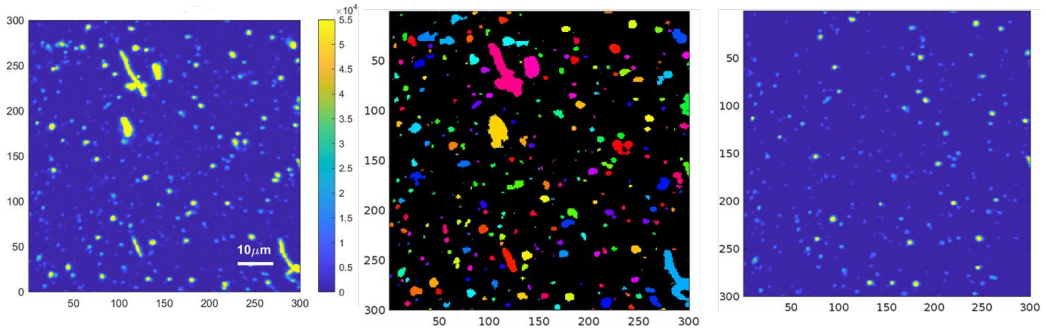

(a) Background removal

(b) Object identification

(c) Filtered PL map showing single NDs and sub-resolution aggregates

Fig. 6.7 PL-map processing pipeline used to select single emitters for ODMR measurements. All maps were acquired over 80×80 μm^2 with fixed dwell time and pixel size, allowing statistical emitter selection.

CW-ODMR spectra were then fitted with double Lorentzian profiles (see Fig. 6.8a) to estimate C and $\Delta\nu$, and the set $\{C,\Delta\nu,R\}$ was inserted in Eq. 6.1 to compute the sensitivity η_T.

Sensitivity definition. For temperature sensing, the shot-noise-limited sensitivity was estimated as

$$\eta_T \approx \frac{K\Delta\nu}{C\sqrt{R}\left|\frac{\partial D_{\mathrm{gs}}}{\partial T}\right|}, \tag{6.1}$$

where K depends on the lineshape ($K\approx0.77$ for a Lorentzian), $\Delta\nu$ is the FWHM linewidth, C is the ODMR contrast, R is the detected photon rate, and $\partial D_{\mathrm{gs}}/\partial T$ is the coupling constant that links temperature to resonance shifts (see Chap. 3). This represents a lower bound under our acquisition conditions.

Results and discussion. Figure 6.8a reports a representative ODMR spectrum with a double-Lorentzian fit. Across batches, linewidth distributions (Fig. 6.8b) remained comparable and did not show systematic broadening despite the higher NV density introduced by irradiation, consistent with operating at low optical and microwave power. By contrast, the ODMR contrast was consistently higher for Irr^{low} samples than for oxidised-only batches (Fig. 6.8c), and statistical tests confirmed that this increase was significant under our conditions. Irradiation followed by annealing increased the NV density, so under the same excitation the detected photon rate

R was higher than in Ox-only samples. This gain in R compensated size-related losses and kept the shot-noise-limited sensitivities clustered around $\sim 10\ \mathrm{K}/\sqrt{\mathrm{Hz}}$ (Fig. 6.8d). In practice, sub-20 nm particles reached sensitivities comparable to much larger oxidised-only batches, despite a reduction in diameter greater than a factor of two and a corresponding volume reduction greater than a factor of eight. Overall, the increased NV density after irradiation and activation offset the photon-budget penalty due to downsizing, without a detectable penalty in $\Delta\nu$ at the low powers used.

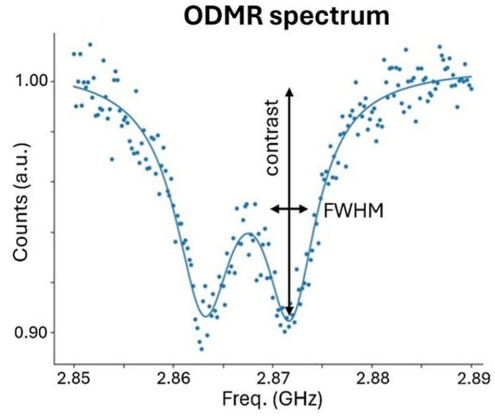

(a) Example ODMR spectrum and double-Lorentzian fit (Irr^{high}ND).

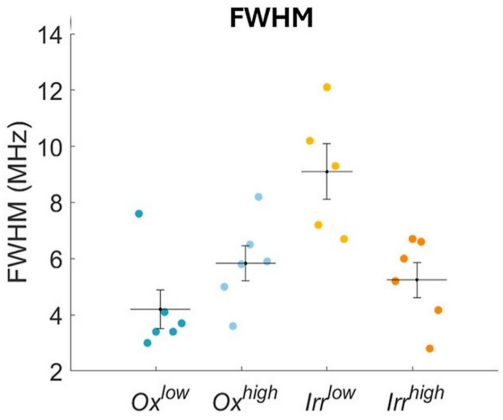

(b) FWHM distributions across batches.

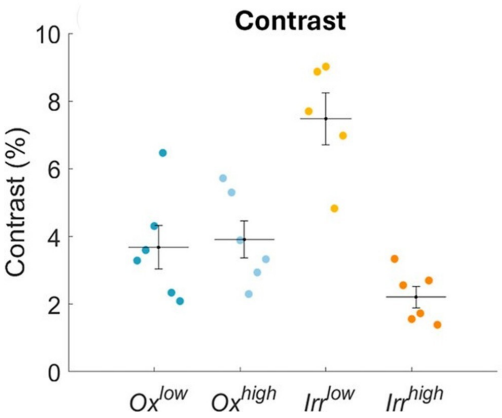

(c) Contrast distributions across batches.

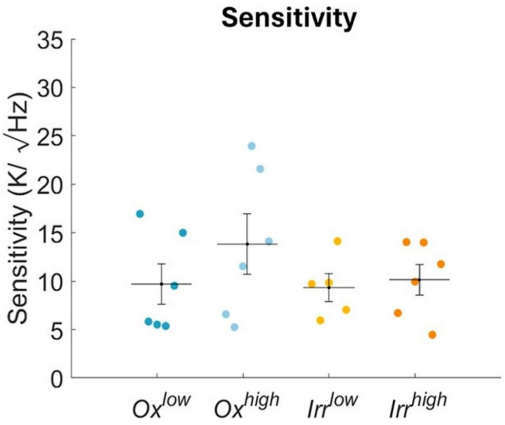

(d) Shot-noise-limited η_T from single NDs.

Fig. 6.8 ODMR metrics and estimated temperature sensitivity. The grid summarizes variations and trends in photoluminescence contrast, linewidth, and thermal sensitivity across processing routes.

6.1.4 Conclusions

Thermal oxidation cleans and functionalises the nanodiamond surface, which improves dispersion in water and stabilises the NV^- charge state close to the surface. Proton irradiation followed by annealing increases the density of color centers by creating vacancies that combine with native nitrogen. When these routes are combined in a controlled sequence the particles become smaller, with averages around ~ 20 nm, but they keep a strong and stable photoluminescence and support reliable CW-ODMR at low optical powers. The single-particle sensitivities remain around $\sim 10\ \mathrm{K}/\sqrt{\mathrm{Hz}}$ despite the large reduction in volume, and the spread of the metrics decreases after the full processing, which makes the behaviour more reproducible across emitters.

From a sensing perspective these results matter because intracellular protocols impose strict limits on optical power and acquisition time. Probes must be small, dispersible, and spectrally stable. The data showed that oxygen termination reduced surface-related noise and that vacancy engineering increased brightness without a linewidth penalty, mitigating the usual size–performance trade-off. In practice this defined a process window for biocompatible NDs that preserved ODMR contrast and narrow lines while reaching sub-20 nm. Future work will refine oxidation and irradiation doses to balance size, brightness, and linewidth, assess long-term stability in physiological buffers, and test performance in cells under realistic optical and microwave constraints.

6.2 Optimization of Germanium–Vacancy Centers in Diamond

The second activity I was involved in concerned the optimization of GeV centers created by ion implantation and post-annealing [117]. The goal was to compare conventional high-vacuum anneals with HPHT processing and to quantify how these routes impact single-emitter brightness, lifetime, and saturation. My specific contribution focused on the optical characterization and data analysis at the single-defect level, including the extraction and comparison of excited-state lifetimes, saturation count rates (I_{sat}), saturation powers (P_{sat}), and the excitation efficiency metric

$E_{\text{sat}} = P_{\text{sat}}/I_{\text{sat}}$, which represents the optical power needed to reach the emission saturation, normalized to the saturated intensity.

This parameter is inversely proportional to the quantum efficiency of the emitter and is therefore a useful figure of merit for evaluating the emitter's performance in terms of excitation–emission conversion. Lower values of E_{sat} indicate more efficient single-photon generation, as fewer excitation photons are needed to reach a given level of emission.

This makes E_{sat} particularly relevant when aiming to minimize heating or power consumption, or when many emitters are addressed simultaneously within integrated photonic platforms. As such, it provides a compact and quantitative indicator to compare the photophysical properties of different fabrication and post-treatment strategies.

Group-IV color centers in diamond are valuable both as SPS and as probes for all-optical thermometry. For thermometry the key point is that the ZPL is temperature dependent and the shift can be read spectrally, so temperature can be measured without applying microwaves. This is useful in biological samples and in integrated photonic platforms where microwave fields are undesirable. As SPS they offer high and stable photoluminescence with narrow spectral lines, which results attractive for quantum applications.

Here we focus on the GeV center (Fig. 6.9a), a representative group-IV emitter with a narrow ZPL at $\sim$602 nm (Fig. 6.9b). Structurally, the GeV is a germanium–divacancy complex: after implantation and annealing a Ge atom occupies the bond-center between two adjacent vacancies along a $\langle 111 \rangle$ axis in a split-vacancy configuration with D_{3d} symmetry (Fig. 6.9a). This inversion-symmetric geometry suppresses a permanent electric dipole and reduces first-order Stark shifts from local fields, which limits spectral diffusion and helps to keep the ZPL narrow and the optical response stable.

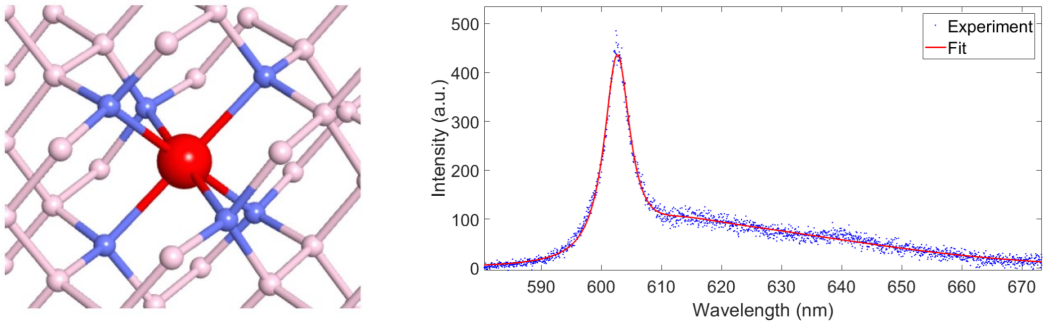

(a) (b)

Fig. 6.9 GeV center in diamond: structural model and optical signature. Panel (a) shows the Ge atom at the bond-center position between two adjacent vacancies, while panel (b) presents a typical room-temperature PL spectrum with the ZPL appearing at ∼602 nm.

A practical question is how to activate GeV centers PL emission efficiently after Ge^- ion implantation and how post-implantation annealing affects brightness, lifetime and the optical power needed to reach saturation. We compare conventional high-vacuum annealing with HPHT processing and we evaluate single-emitter performance with a focus on lifetime, saturation behavior and on an efficiency metric defined as the excitation power required per saturated count rate, E_{sat}.

6.2.1 Samples and Processing

Three type-IIa single-crystal diamonds from Element Six were used. Samples #1 and #2 were electronic grade with dimensions $2 \times 2 \times 0.5$ mm^3 and < 5 ppb of N and B. Sample #3 was optical grade, $3 \times 3 \times 0.3$ mm^3, with $N_{\mathrm{S}} < 1$ ppm and $B_{\mathrm{S}} < 0.05$ ppm. All samples were implanted with 40 keV Ge^-. In each sample we defined square regions of approximately 200×200 μm^2 using a collimation mask, and we set fluences between 10^{10} and 10^{13} cm^{-2}. Single GeV centers were later probed near the outer edges of these squares where scattered ions create isolated defects at low areal density. The objective is to compare vacuum anneals at different temperatures with an HPHT treatment and to quantify their effect on activation and optical performance.

Table 6.1 Summary of samples and post-implantation treatments. The table lists the different processing steps applied to each sample, including annealing and oxidation conditions.

Sample	**Grade**	**Size (mm^3)**	**Impurities**	**Post-implantation annealing**
#1	Electronic	$2 \times 2 \times 0.5$	< 5 ppb N, < 5 ppb B	900°C for 2 h and 1000°C for 10 h, in high vacuum
#2	Electronic	$2 \times 2 \times 0.5$	< 5 ppb N, < 5 ppb B	1500°C for 1 h, in high vacuum
#3	Optical	$3 \times 3 \times 0.3$	$N_S < 1$ ppm, $B_S < 0.05$ ppm	2000°C for 15 min at 6 GPa, HPHT

Vacuum anneals were used to diffuse vacancies and form GeV centers in samples #1 and #2. HPHT processing for sample #3 was carried out with a split-sphere multi-anvil press under quasi-hydrostatic conditions at 2000°C and 6 GPa for 15 min.

6.2.2 Experimental Approach

Experimental setup. A home-built confocal microscope (see Chap. 5.1) was used to locate and study single GeV centers (see Fig. 6.10). A continuous-wave 520 nm laser was coupled through a single-mode fiber, directed to the sample by a dichroic beamsplitter and focused with a high-NA objective. The same objective collected the photoluminescence, which passed through long-pass filters and was coupled into a multimode fiber that could be connected either to a spectrometer for ZPL confirmation or to single-photon detectors for correlation and counting. The Hanbury Brown and Twiss interferometer used a 50:50 fiber beamsplitter, two SPADs and a time-correlation module. A short optical delay on one arm and a small electronic delay on the timing unit improved the visualization and the fitting of the antibunching dip. This arrangement enabled PL maps, spectra and $g^{(2)}(\tau)$ traces on the same platform.

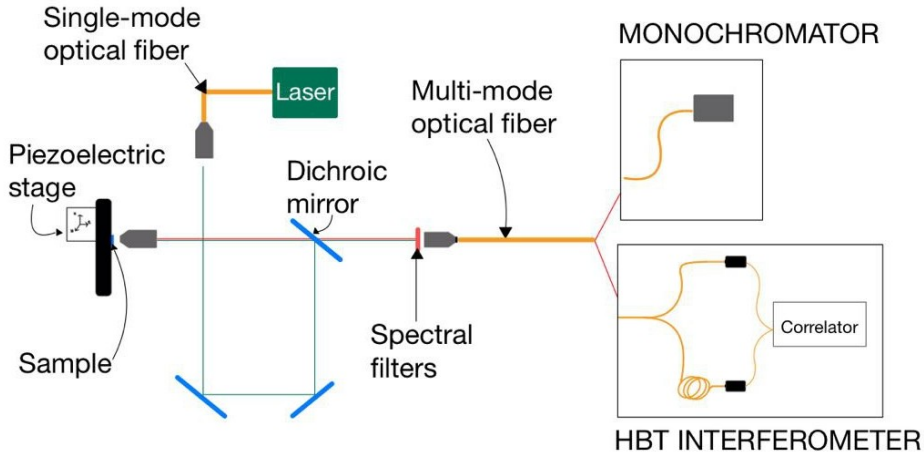

Fig. 6.10 Schematic of the confocal PL and HBT setup used for single GeV center characterization. The system enables both spectral analysis and second-order correlation measurements to identify single-photon emitters.

Experimental procedure. Single GeV centers were searched by PL mapping at the edges of the implanted squares where isolated emitters are more likely (see Fig. 6.11). For each candidate spot we recorded a PL spectrum to confirm the GeV ZPL at $\sim$602 nm, then we measured $g^{(2)}(\tau)$ and attributed single-photon emission when $g^{(2)}(0) < 0.5$. Intensity–power curves were fitted using the saturation model in Eq. 2.8, and the excited-state lifetime τ was extracted from the linear dependence of the antibunching rate $\lambda_1(P)$ using Eq. 2.11. To compare processing routes we used the efficiency parameter E_{sat}, where a lower value indicates a higher photon output per unit excitation power.

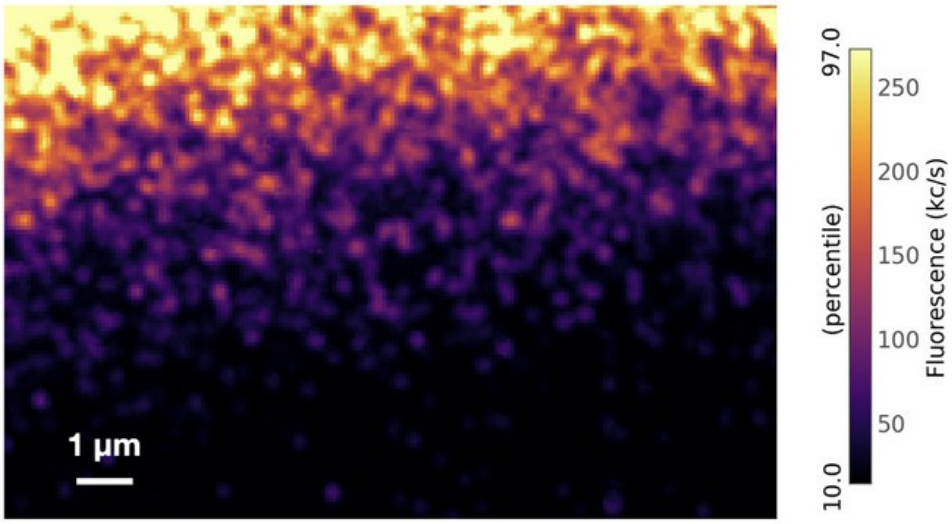

Fig. 6.11 Example confocal PL map at the edge of an implanted region highlighting isolated emitters. The spatial distribution reveals localized GeV centers suitable for single-photon studies.

6.2.3 Results and Discussion

The following are the results of the investigations on GeV centers.

HPHT cleans the spectrum and promotes GeV. Low-temperature PL measured before and after HPHT on the same region shows a clear spectral reshaping. NV emission and the 467.7 nm band decrease, while the GeV ZPL at $\sim$602 nm becomes the dominant feature (Fig. 6.12). The ratio between the GeV ZPL and the diamond Raman line increases, which indicates a higher relative GeV contribution and fewer competing centers.

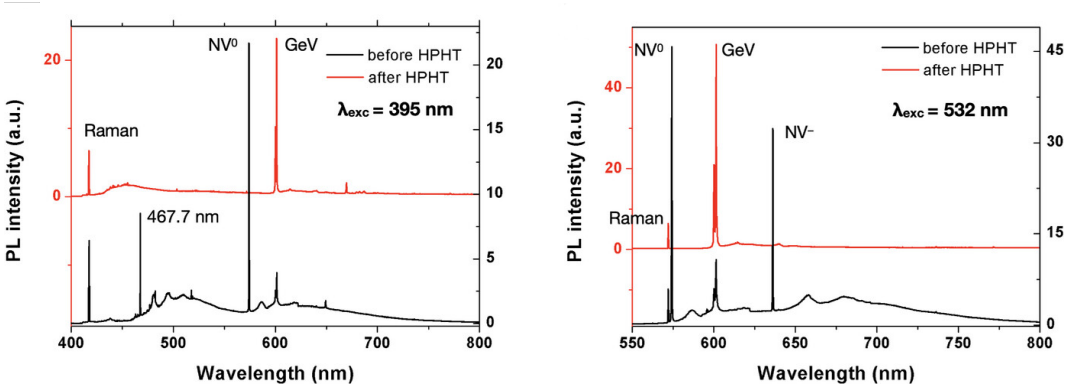

(a) PL before and after HPHT, $\lambda_{\text{exc}} = 395$ nm. (b) PL before and after HPHT, $\lambda_{\text{exc}} = 532$ nm.

Fig. 6.12 Spectral effect of HPHT treatment. The GeV ZPL at ∼602 nm becomes dominant, while NV-related and 467.7 nm bands are suppressed, indicating efficient defect conversion.

Single-photon validation and lifetime. PL maps at the edges of the implanted regions revealed bright isolated spots that we selected for analysis. Autocorrelation traces showed $g^{(2)}(0) < 0.5$ over a range of excitation powers (Fig. 6.13a), which confirms single-photon emission. The antibunching rate increased linearly with power as expected from a three-level model, and from the intercept we estimated the excited-state lifetime (Fig. 6.13b). Looking at Fig. 6.14a, one can notice that, when grouping the data by post-implantation treatment, the lifetime distributions partly overlap. HPHT centers often show longer lifetimes, consistent with the median values reported in Table 6.2.

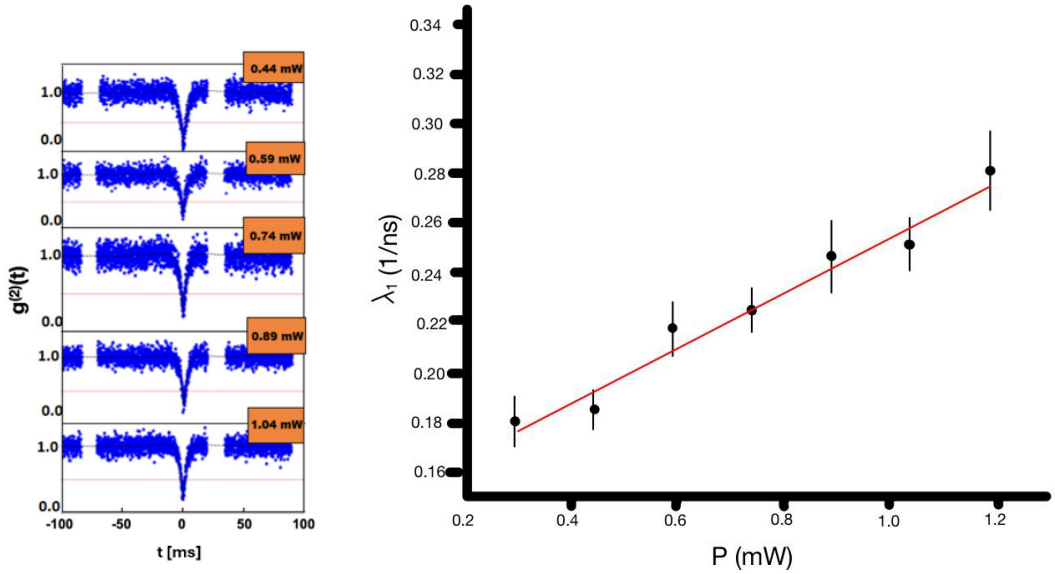

(a) Second-order autocorrelation traces.

(b) Antibunching rate versus power, linear fit to extract lifetime.

Fig. 6.13 Single-photon validation and lifetime extraction for representative emitters. The curves show the antibunching behavior and exponential decay used to determine excited-state lifetimes.

Saturation behavior and efficiency. From the intensity–power curves we extracted I_{sat} and P_{sat} for each emitter. After 900 to 1000°C vacuum anneals both parameters display wide variability across nominally identical regions, which suggests a nonuniform residual damage. Increasing the vacuum anneal temperature to 1500°C lowers P_{sat} on average, which points to improved activation and fewer traps. The HPHT route gives the largest change, with a lower median P_{sat} around 0.9 mW and a higher median I_{sat} around 1.2 Mcps. As a consequence the efficiency metric E_{sat} is the smallest for HPHT, with improvements up to about a fourfold factor compared to 900°C in vacuum. These trends are consistent with the box-chart statistics of $P_{\mathrm{sat}}/I_{\mathrm{sat}}$, see Figs. 6.14b and 6.14c, and with the medians summarized in Table 6.2.

Table 6.2 Median excited-state lifetimes and saturation parameters for single GeV centers under different post-implantation anneals. The table summarizes values extracted from the reference study, highlighting the performance enhancement achieved by HPHT processing.

Post-implantation treatment	**Median τ [ns]**	**Median I_{sat} [kcps]**	**Median P_{sat} [mW]**
900°C (2 h), vacuum	4.8 ± 1.9	900 ± 600	3.0 ± 1.2
1000°C (10 h), vacuum	5.9 ± 1.6	600 ± 500	3.1 ± 1.4
1500°C (1 h), vacuum	3.0 ± 0.6	650 ± 350	1.2 ± 0.5
HPHT (2000°C, 6 GPa, 15 min)	7.0 ± 0.9	1200 ± 400	0.9 ± 0.3

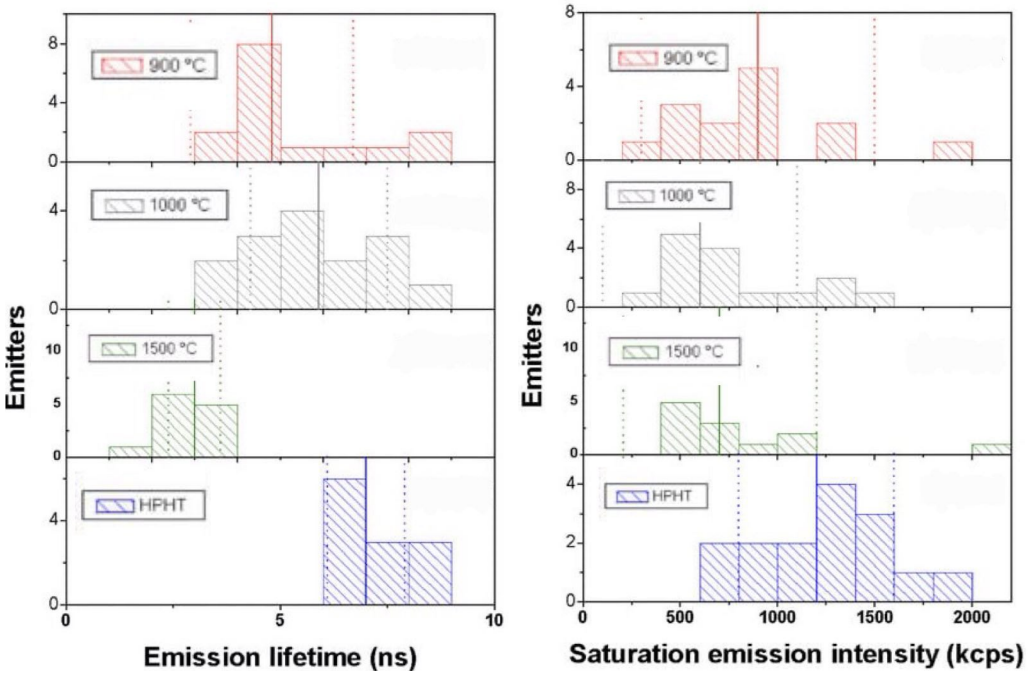

(a) Lifetime τ. (b) I_{sat}.

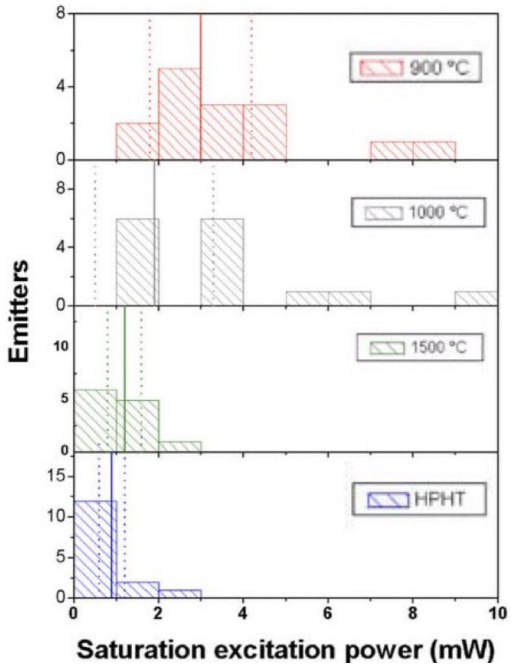

(c) P_{sat}.

Fig. 6.14 Distributions of τ, I_{sat}, and P_{sat} for different annealing routes. The plots demonstrate that HPHT treatment yields longer lifetimes, higher saturated count rates, and lower saturation powers, indicating enhanced emitter brightness.

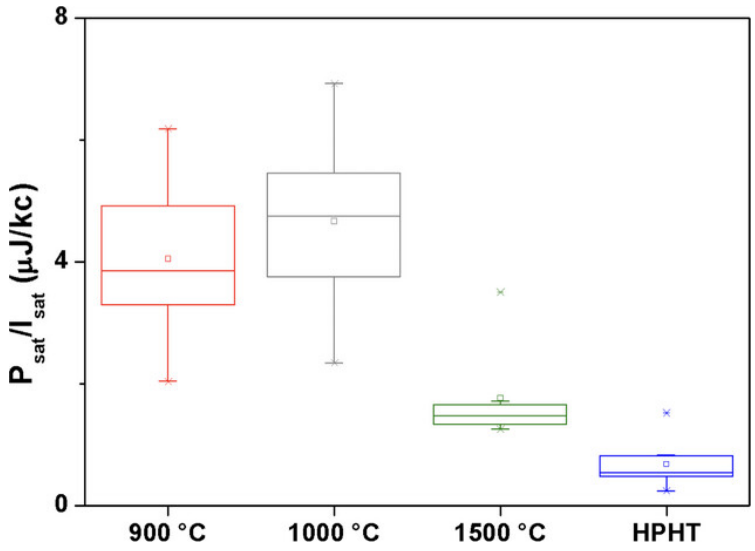

Fig. 6.15 Efficiency metric $E_{\mathrm{sat}} = P_{\mathrm{sat}}/I_{\mathrm{sat}}$. Lower values correspond to more efficient excitation–emission cycles, HPHT-treated samples show the smallest medians, consistent with up-to-fourfold improvements in optical efficiency.

Interpretation. The combined spectral, lifetime and saturation trends suggest that HPHT reduces residual implantation damage such as multi-vacancy complexes, stabilizes the GeV charge state and suppresses nonradiative recombination. The lower P_{sat} and the higher I_{sat} are consistent with a cleaner local environment and with fewer competing defects, which makes HPHT a suitable route when high-efficiency GeV emission is required.

6.2.4 Conclusions

We compared vacuum anneals at different temperatures with HPHT processing for activating GeV centers created by ion implantation. The experiments show that HPHT reshapes the spectrum in favour of GeV, reduces the optical power needed to reach saturation and increases the saturated count rate. Lifetime statistics indicate a reduction of nonradiative channels, which is consistent with a cleaner microscopic environment around the emitter. In practical terms this leads to higher photon rates at lower excitation power, a desirable combination for photonic integration and for thermometry where self-heating must be minimized. The efficiency parameter E_{sat} improves systematically under HPHT and reaches the lowest median values among the tested routes, with gains up to about a factor four relative to 900°C vacuum

anneals. These overall trends are in line with the single-emitter study on GeV centers, which identified HPHT as an effective pathway to enhance excitation–emission efficiency for integrated quantum photonics.

Chapter 7

Experiment – Biological Application

In this chapter, I will explore the possibility to simultaneously monitor neuronal activity and temperature variations in living neuronal cultures using nanodiamond-based quantum thermometry. By integrating ODMR techniques with a MEA platform, we aim to establish a robust experimental protocol that allows real-time, biocompatible dual readout of electrophysiological and thermal signals.

This investigation focuses on validating the compatibility of the setup with biological samples, optimizing the acquisition parameters, and preparing the system for future experiments that will probe the thermal impact of neural excitation and silencing.

7.1 Simultaneous recording of firing activity and temperature variation in neuronal culture

Since temperature plays a crucial role in biology and medicine, regulating several cellular processes and acting as a potential indicator of pathological conditions such as Parkinson's or Alzheimer's disease [118, 119], it is of great importance to understand the temperature dynamics inside the cell and how temperature variations can affect neuronal health. To correlate these two phenomena, it is necessary to simultaneously acquire both the electrical activity of the neuronal network and the local temperature changes. Inspired by the approach presented in [8], I was involved in an experiment whose goal was to design an experimental setup capable

of performing NV-based thermometry while simultaneously recording the electrical signals of the same neuronal culture.

This work is still ongoing at INRiM laboratories, but I was able to contribute to the realization and preliminary validation of the setup.

The platform required for electrophysiology measurement of the neuronal network is a MEA, described in Chap. 5.2, which was integrated in the typical confocal microscope to relize a setup combining this technique with the optical and electrophysiological readout. It was initially essential to verify that the experimental conditions imposed by the ODMR measurement were compatible with neuronal viability. To this purpose, all variables involved in the ODMR experiment were tested separately: first the nanodiamond incubation, then the effect of laser excitation and of the microwave field, and finally the combined conditions simulating a full ODMR acquisition. These tests confirmed the compatibility of our measurement protocol with living neuronal cultures.

Once the experimental parameters were demonstrated to be biocompatible, and before applying pharmacological protocols to modulate network activity, we tested the solvent used for drug dilution, dimethyl sulfoxide (DMSO). DMSO, although widely used, can be cytotoxic or induce bath heating if not properly diluted. Therefore, a careful dilution protocol was developed and validated through ODMR measurements performed both with and without cells, confirming that the solvent did not induce measurable thermal artifacts.

7.1.1 Setup

The experimental setup used for the simultaneous optical and electrical acquisition is based on a confocal microscope integrated with a live-cell electrophysiology platform. The confocal configuration ensures high spatial resolution and optical sectioning, as described in Chap. 5. The system is built around an inverted microscope (Olympus IX73, Fig. 7.2a), adapted to host the optical excitation and collection paths required for ODMR thermometry. A schematic of the setup is shown in Figure 7.1.

The excitation source (532 *nm*) is provided by the 2^{nd} harmonics of a continuous-wave Nd:YAG laser (Coherent Prometheus 100NE) delivering up to 100 mW with excellent power stability. The beam is driven by two dielectric mirrors used for alignment along the optical path, and through a periscope mirror to adjust the

height of the beam. A dichroic mirror (long-pass at 567 nm) reflects the green excitation light toward the sample, where it is focused by an air objective (Olympus UPlanFL 60×, NA 0.67). This configuration provides a diffraction-limited spot size of approximately 1.2 µm, ideal for single-nanodiamond measurements.

The MEA headstage (Fig. 7.2b) is mounted on a piezoelectric scanning stage (Prior ProScan III,) which allows precise movement in the *xy* plane for imaging and region-of-interest selection. Below the MEA, a planar copper antenna is positioned to deliver the MW field necessary for ODMR excitation of the NV centers. The microwave signal is generated by a Keysight N5172B synthesizer and amplified by a Mini-Circuits ZVA-183G-S+ power amplifier to a maximum output of 20 dBm. The antenna geometry is optimized to produce a homogeneous MW field across the central region of the MEA, where the neurons are located.

The NV photoluminescence is collected through the same objective used for excitation, passes through the dichroic mirror, and is filtered by a 532 nm notch filter and a 650 nm long-pass emission filter. The filtered fluorescence is then focused onto a pinhole and detected by a single-photon avalanche diode (PerkinElmer SPCM-AQR-15) operating in photon-counting mode. Photon counts are acquired by a National Instruments *USB-6343* board and processed for ODMR analysis. Wide-field imaging of the neuronal layer can also be performed through the Olympus eyepiece.

In summary, the integrated configuration allows simultaneous recording of the neurons' electrical activity through the MEA and their local temperature through the NV-based optical readout, enabling direct correlation between network firing and nanoscale thermal dynamics.

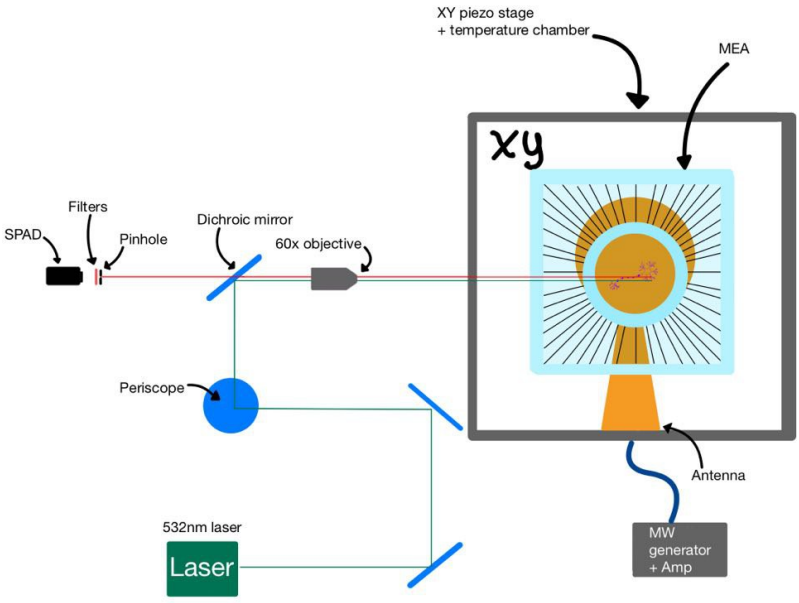

Fig. 7.1 Schematic of the confocal setup integrated with the MEA platform for simultaneous ODMR thermometry and electrical recording. The configuration enables correlated optical and electrophysiological measurements in neuronal cultures.

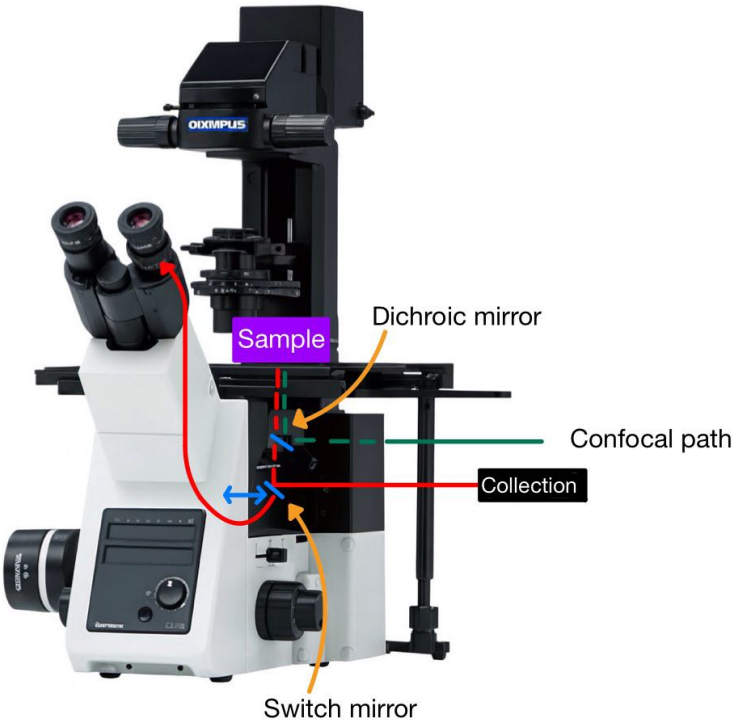

(a) Schematic of the inverted confocal microscope (Olympus IX73) used for ODMR thermometry. The optical path includes the excitation laser reflected by a dichroic mirror toward the sample, and the emitted PL collected back through the same objective and directed to the confocal detection path. The switch mirror allows toggling between widefield and confocal imaging modes.

(b) MEA recording platform and headstage (Multi Channel Systems) integrated with the confocal setup for simultaneous optical and electrophysiological acquisition.

Fig. 7.2 Optical path of the confocal microscope used for NV-based thermometry and MEA recording system. Panel (a) shows the optical components, and panel (b) illustrates the integrated electrical system for combined temperature and activity measurements.

7.1.1.1 Tracking system

I upgraded the setup by adding a fast steering mirror (FSM; Newport FSM–CD300B) to enable PL mapping and real–time tracking of a selected ND, a sketch of the upgraded setup is reported in Fig. 7.4.

The FSM is placed in a plane conjugate to the back aperture of the objective (pupil–conjugate plane) using a $4f$ relay made of two lenses with focal lengths f_1 and f_2 (Fig. 7.3). In this configuration, a small angular deflection at the mirror produces a lateral shift at the sample while the illumination of the objective back aperture remains constant. Practically, the FSM sits at the front focal plane of the first relay lens and the objective pupil is conjugated to the back focal plane of the second lens, this preserves numerical aperture and confocal alignment and avoids beam walk at the pinhole.

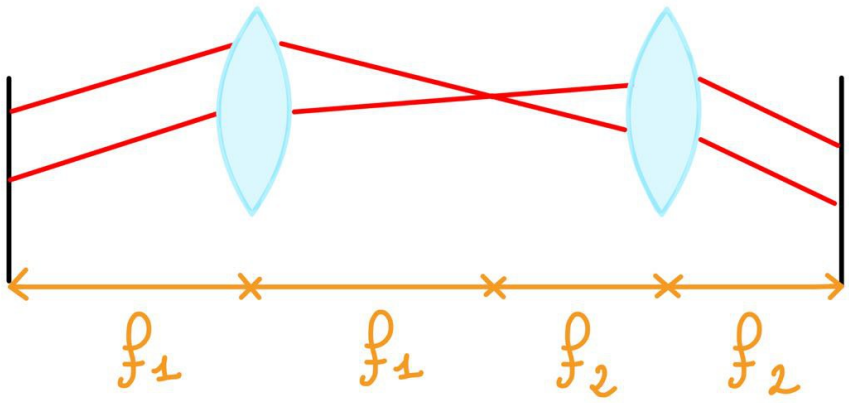

Fig. 7.3 Schematic representation of a 4f optical relay system. The setup consists of two lenses separated by the sum of their focal lengths ($f_1 + f_2$). The configuration reimages a scanning or FSM mirror onto the objective pupil, ensuring lateral motion of the focal spot without changing the illumination angle.

In PL mapping mode, the FSM performs a grid scan to acquire PL maps that help locate bright nanodiamonds. In tracking mode, the same mirror keeps the selected ND centered in the confocal focus to reduce signal drift and noise. This is achieved by small periodic adjustments of the mirror position based on the detected PL intensity. All components are synchronized to maintain stable operation during long acquisitions. With this FSM and $4f$ relay, the ND stays centered, the pinhole

remains aligned, and the stability and precision of the ODMR temperature readout are improved while remaining fully compatible with MEA recordings.

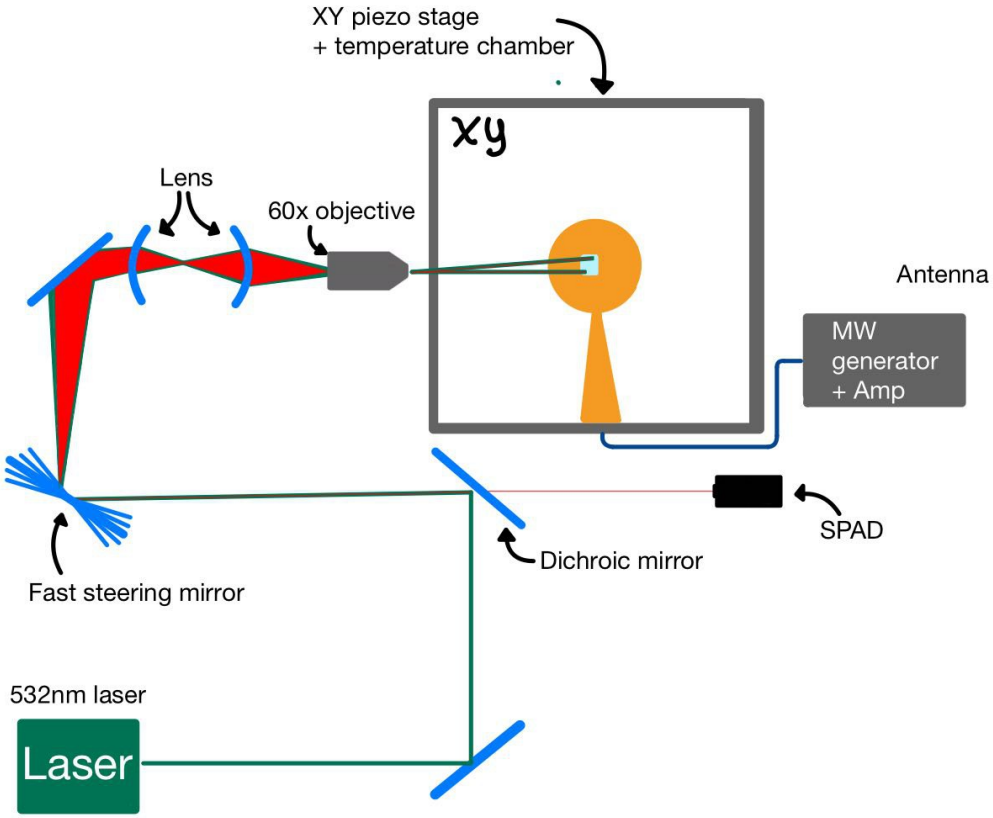

Fig. 7.4 Optical and electronic components of the real-time tracking system. The FSM is positioned at a pupil-conjugate plane with a 4f relay so that mirror tilts produce lateral shifts while maintaining alignment of the confocal pinhole.

7.1.2 Experimental results

7.1.2.1 Calibration curves

The ability to convert the spectral shift of the NV center into a precise temperature variation relies on an accurate calibration of each ND. This procedure establishes the proportionality between the zero-field splitting and temperature, expressed by the thermal coefficient γ_T, and is therefore a fundamental step before applying the method to live-cell thermometry.

To calibrate the NDs, i.e. to estimate the γ_T of each ND, one normally measures how the resonance frequencies shift when temperature changes using the method explained in Sec. 3.2.2 and performs a linear interpolation to extract the thermal coefficient (see Fig. 4.3). However, we observed two critical issues when this procedure was applied to our data [120]. First, choosing different resonance dips leads to different calibration coefficients, even under the same conditions, showing that the result depends on which peak is tracked (see Fig. 7.5). Second, when the temperature sweep is reversed, the points recorded during the cooling phase do not lie on the same line as the heating path. This deviation reveals that slow drifts or external perturbations can shift the resonance frequencies over time in ways unrelated to temperature, introducing an uncertainty into the calibration that is difficult to determine.

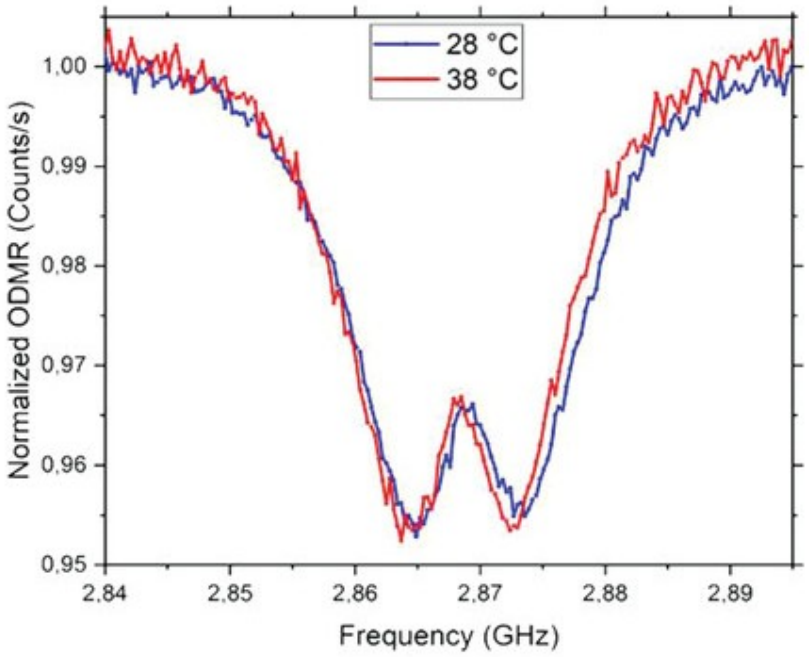

Fig. 7.5 ODMR spectra acquired at two different temperatures. The comparison shows that slow drifts or external magnetic fields can mimic temperature-induced shifts, highlighting the need for correlation-based calibration.

After noticing that the choice of a single resonance dip results in unreliable and variable γ_T values, we adopted a more robust method based on the full differential ODMR spectrum.

Spectra at each temperature were acquired by averaging approximately 500 sweeps, corresponding to an integration time of about one minute per frequency. The linear regions of the differential spectrum were then identified and fitted with straight lines that maximized the R^2 coefficient (see Fig. 7.6). The frequency shift associated with each temperature point was extracted by detecting the zero-crossings of the fitted lines. This analysis was applied independently to all available linear regions, producing multiple estimates of ΔD_{gs} for each temperature step.

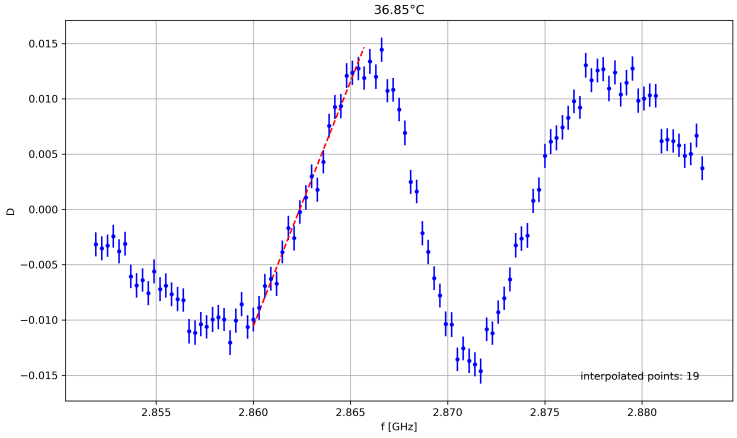

(a)

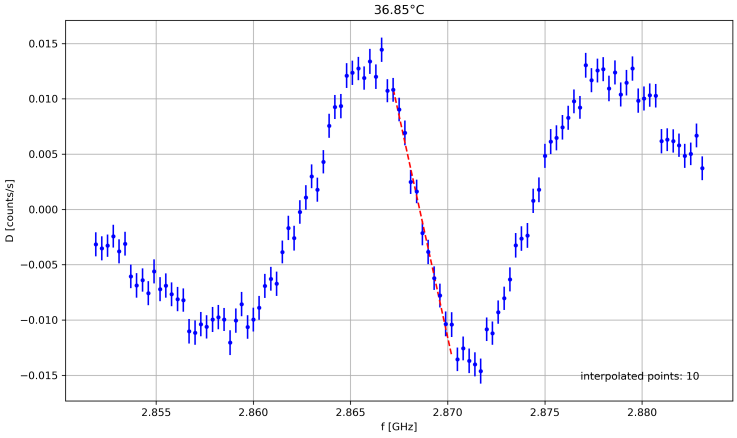

(b)

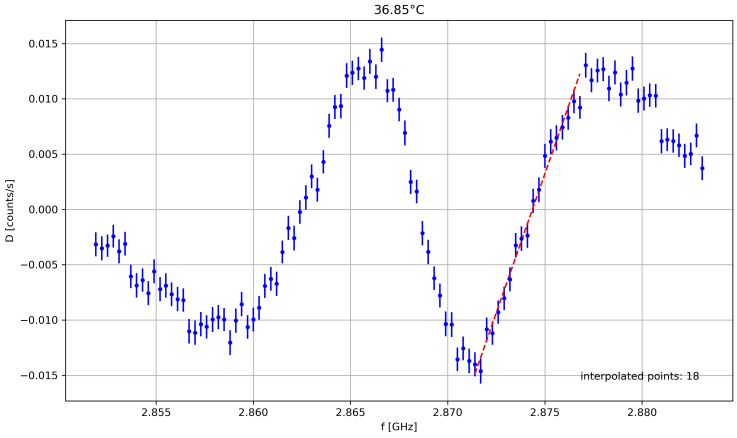

(c)

Fig. 7.6 Linear regions of the differential ODMR spectrum used for calibration. Each panel shows one of the three main resonance dips, with dashed lines indicating linear interpolation regions used to extract temperature coefficients.

In parallel, I evaluated an alternative strategy based on correlation analysis. Instead of focusing on specific resonance dips, the whole ODMR spectrum was considered. Each spectrum was compared to a reference using Pearson correlation [121]: by shifting one spectrum relative to the other and computing the correlation at each step, the optimal frequency offset corresponding to the maximum correlation was identified and taken as the temperature-induced spectral shift.

To improve precision, the spectra were upsampled via interpolation, increasing the effective resolution beyond the step size of the scan. A Monte Carlo method was also implemented: synthetic spectra were generated by adding noise compatible with the measured signal-to-noise ratio, and the correlation procedure was repeated multiple times. For each calibration point, the shift was determined as the average of the individual simulation results, and its associated uncertainty was estimated as the standard deviation of the mean.

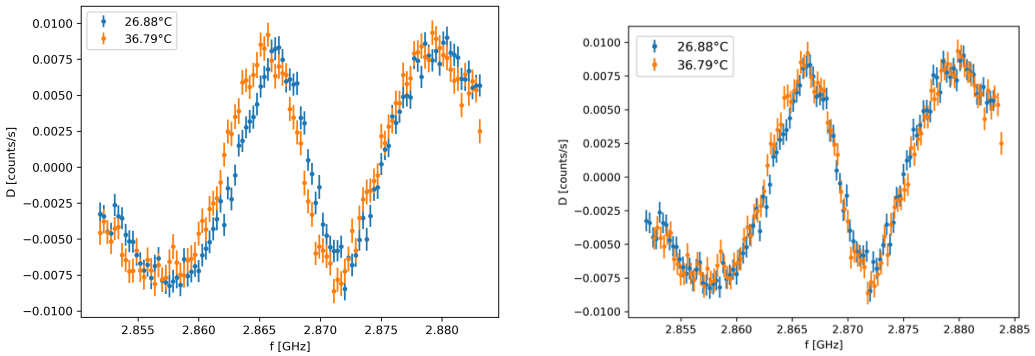

(a) Raw ODMR spectra acquired at different temperatures, showing slight misalignment due to slow drifts and field fluctuations.

(b) Same spectra after applying the frequency shift computed via correlation. The curves are realigned, isolating the pure temperature-induced displacement.

Fig. 7.7 Effect of correlation analysis on calibration spectra. The method compensates for slow drifts and magnetic fluctuations, yielding improved spectral alignment and more accurate γ_T estimation.

Table 7.1 summarizes the calibration results obtained from five independent measurements. The γ_T values derived from individual resonance dips show variability, which reflects the sensitivity of each peak to noise and drift. However, their associated uncertainties are comparable to those obtained with the correlation method.

This result leads to two viable strategies for quantifying temperature shifts:

- Evaluate the temperature shift from each linear region of the differential spectrum (using the respective γ_T) and compute a weighted average.
- Apply the correlation-based method to determine the global spectral shift.

Although the correlation-based method offers an elegant solution and is less sensitive to local distortions, it is still not widely adopted. For this reason, in future experiments we will rely on the differential fitting of multiple linear regions, which combines interpretability and consistency. Nonetheless, the correlation method remains promising and deserves further study.

Table 7.1 Summary of calibration results for five calibration curves. The table reports the fitted thermal coefficients γ_T (in kHz/K) for each resonance peak and for the correlation-based approach.

Calibration	γ_T Left [kHz/K]	γ_T Central [kHz/K]	γ_T Right [kHz/K]	γ_T Correlation [kHz/K]
1	-89.0 ± 4.1	-89.7 ± 3.6	-103.8 ± 3.6	-93.0 ± 12.0
2	-104.5 ± 6.1	-90.6 ± 3.5	-54.9 ± 5.9	-74.0 ± 8.0
3	-85.6 ± 5.3	-78.1 ± 4.6	-59.8 ± 4.2	-70.0 ± 6.0
4	-123.8 ± 6.1	-85.9 ± 4.4	-69.4 ± 6.0	-64.0 ± 11.0
5	-104.7 ± 4.7	-79.6 ± 3.3	-78.2 ± 4.3	-81.0 ± 5.0
Mean ± SD	-99.0 ± 2.3	-85.1 ± 1.7	-65.1 ± 2.0	-76.2 ± 3.2

7.1.2.2 Viability test

To corroborate our analysis is necessary to assess the viability of cells, i.e. to record the activity of the network while applying experimental variables.

Viability measurements were performed on primary hippocampal neuronal cultures at 14–15 days in vitro, following the same preparation described by Petrini et al. [8]. At this developmental stage, the neurons establish mature synaptic networks and display spontaneous electrical activity suitable for stability testing.

Under standard culture conditions, hippocampal neurons are kept at 37 °C in a humidified atmosphere containing 5% CO_2, which maintains the physiological pH and supports normal metabolic activity. During optical and electrophysiological measurements, this condition cannot be fully reproduced, since the setup does not

include an incubator. For this reason, the bath temperature was precisely regulated at 37 °C using the heater integrated into the MEA platform, while the temperature was continuously monitored by a thermocouple placed near the sample. During recordings, the cultures were temporarily exposed to ambient air, and specific control tests were carried out to confirm that the absence of CO_2 during short measurement sessions does not affect the spontaneous firing activity of the network.

The effect of the experimental protocol on neuronal functionality was assessed by comparing the firing rate under different environmental or optical conditions. Data obtained under each condition were statistically compared using the Kruskal–Wallis test with a significance level of $p < 0.05$. This nonparametric approach allows comparison between groups without assuming normality of the data distribution.

In the first test, the stability of neuronal activity was examined in the absence of CO_2. Recordings were carried out in ambient air for 30 minutes while monitoring spontaneous spiking activity. No significant variation in firing rate was detected across 10-minute intervals (Fig. 7.8, Tab. 7.2), indicating that short-term exposure to an open-air environment does not compromise neuronal excitability within the duration of the experiments.

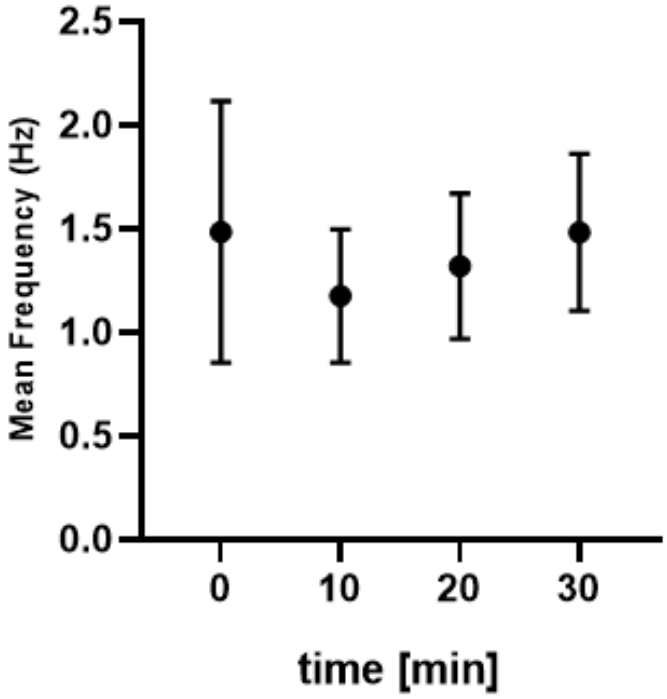

Fig. 7.8 Time course of firing rate in the absence of CO_2 over 30 minutes. The graph shows stable neuronal activity, confirming baseline consistency during control experiments.

Table 7.2 Multiple comparisons following Kruskal–Wallis test for neuronal firing in absence of CO_2. The table reports that no significant differences were found ($p > 0.05$).

Comparison	**Adjusted *p*-value**	**Significant?**
0 min vs 10 min	0.1632	No
0 min vs 20 min	0.2972	No
0 min vs 30 min	> 0.9999	No
10 min vs 20 min	> 0.9999	No
10 min vs 30 min	0.2919	No
20 min vs 30 min	0.5265	No

The potential influence of nanodiamonds on neuronal physiology was evaluated by incubating the cultures with a final concentration of 0.6 µg/mL for 5 hours, as in the reference protocol [8]. Baseline recordings were acquired before the addition of nanodiamonds and compared with those collected after incubation. The Kruskal–Wallis test confirmed that no significant difference was present between

the two conditions. These results demonstrate that the chosen nanodiamond concentration and incubation time do not alter the firing properties of hippocampal networks.

The possible effect of optical excitation was then tested by illuminating the nanodiamond-loaded cultures with a continuous 532 nm laser at 1 mW for 30 minutes. The firing rate remained unchanged throughout the exposure (Fig. 7.9, Tab. 7.3). This power level was therefore selected as an upper limit for subsequent measurements, ensuring that illumination intensities below this threshold can be applied without risk of photo-induced alterations in neuronal activity.

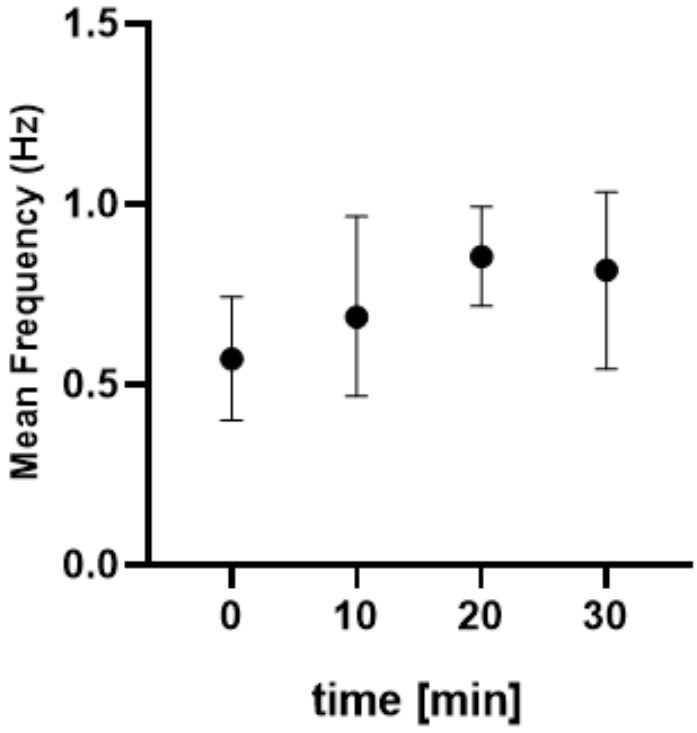

Fig. 7.9 Firing activity under continuous 1 mW laser illumination. The measurements show no significant perturbation, indicating optical safety under typical excitation power.

Table 7.3 Multiple comparisons following Kruskal–Wallis test for 1 mW laser exposure. The table confirms no significant differences across time points ($p > 0.05$).

Comparison	**Adjusted p-value**	**Significant?**
0 min vs 10 min	> 0.9999	No
0 min vs 20 min	0.1482	No
0 min vs 30 min	0.5040	No
10 min vs 20 min	> 0.9999	No
10 min vs 30 min	> 0.9999	No
20 min vs 30 min	> 0.9999	No

The tolerance of neurons to microwave irradiation was also evaluated. Microwaves were applied at an input power of –10 dBm, amplified by 20 dB using a Mini-Circuits ZVA-183G-S+ amplifier, resulting in an estimated output power of approximately +10 dBm at the antenna. Continuous microwave exposure for 30 minutes, in the presence of nanodiamonds, did not induce any measurable change in firing dynamics (Fig. 7.10, Tab. 7.4), confirming that the applied electromagnetic fields are compatible with neuronal viability under the adopted experimental parameters.

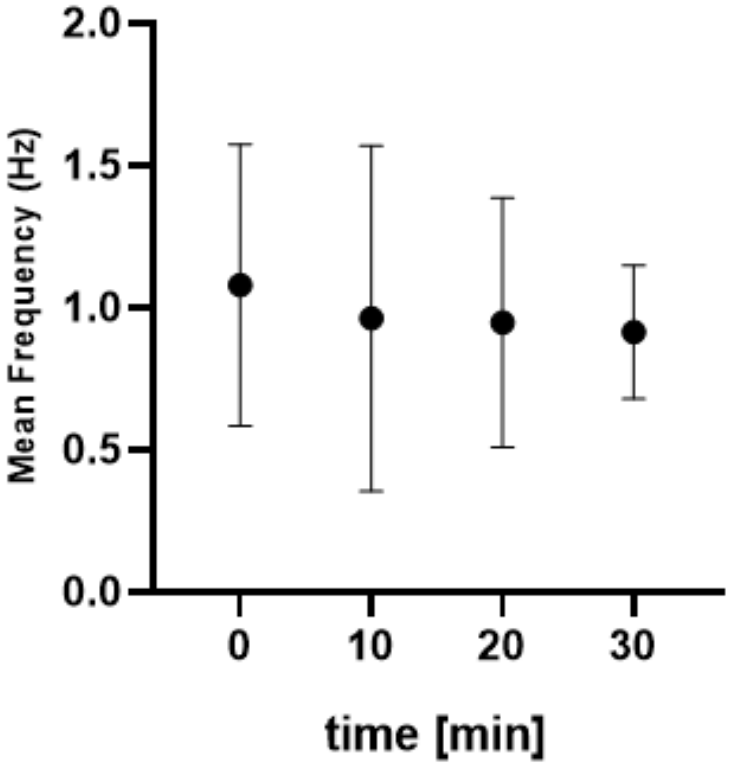

Fig. 7.10 Firing rate during 30 minutes of microwave and ND exposure. The data demonstrate that neuronal activity remains statistically indistinguishable from baseline conditions.

Table 7.4 Multiple comparisons following Kruskal–Wallis test for firing rate under MW exposure. The analysis reveals no significant differences ($p > 0.05$).

Comparison	**Adjusted *p*-value**	**Significant?**
0 min vs 10 min	0.0739	No
0 min vs 20 min	> 0.9999	No
0 min vs 30 min	> 0.9999	No
10 min vs 20 min	> 0.9999	No
10 min vs 30 min	0.1525	No
20 min vs 30 min	> 0.9999	No

These results demonstrate that the individual contributions of environmental (CO_2), optical (laser), and electromagnetic (microwave) factors, as well as nanodiamond internalization, do not significantly affect the electrophysiological properties of the cultures within the experimental time.

The combined optical and electrical configuration adopted in this study can therefore be considered biocompatible for short-term live measurements.

7.1.2.3 ODMR simulation

To further evaluate the overall compatibility of the experimental conditions, a simulation of a full ODMR acquisition was performed by combining nanodiamond incubation, optical excitation, and microwave irradiation under the most demanding parameters tested. This approach was intended to replicate as closely as possible the real operating conditions of the thermometric measurements while maintaining the same acquisition duration used for the individual viability test.

During the simulated measurement, the cultures were exposed to continuous 532 nm illumination at 1 mW and microwave excitation corresponding to an effective power of approximately +10 dBm at the antenna. Under these conditions, the firing rate remained unchanged compared to baseline recordings, confirming that the simultaneous presence of the optical and electromagnetic fields does not compromise the physiological integrity of the neuronal cultures (Fig. 7.11, Tab. 7.5).

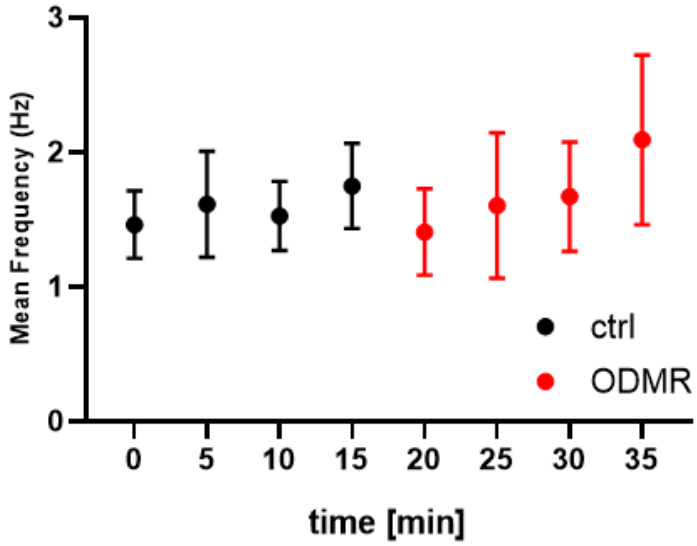

Fig. 7.11 Simulated ODMR acquisition performed on hippocampal cultures. The combination of nanodiamonds, laser excitation, and microwave irradiation did not produce measurable changes in neuronal firing.

Table 7.5 Multiple comparisons following Kruskal–Wallis test for firing rate during ODMR acquisition. The table shows that all variations fall within expected physiological variability.

Comparison	**Adjusted p-value**	**Significant?**
0 min vs 5 min	> 0.9999	No
0 min vs 10 min	> 0.9999	No
0 min vs 15 min	> 0.9999	No
0 min vs 20 min	> 0.9999	No
0 min vs 25 min	0.9999	No
0 min vs 30 min	> 0.9999	No
0 min vs 35 min	> 0.9999	No
5 min vs 10 min	> 0.9999	No
5 min vs 15 min	> 0.9999	No
5 min vs 20 min	> 0.9999	No
5 min vs 25 min	0.6414	No
5 min vs 30 min	> 0.9999	No
5 min vs 35 min	> 0.9999	No
10 min vs 15 min	> 0.9999	No
10 min vs 20 min	> 0.9999	No
10 min vs 25 min	> 0.9999	No
10 min vs 30 min	> 0.9999	No
10 min vs 35 min	> 0.9999	No
15 min vs 20 min	> 0.9999	No
15 min vs 25 min	> 0.9999	No
15 min vs 30 min	> 0.9999	No
15 min vs 35 min	> 0.9999	No
20 min vs 25 min	0.2236	No
20 min vs 30 min	0.7410	No
20 min vs 35 min	0.0184	Yes
25 min vs 30 min	> 0.9999	No
25 min vs 35 min	> 0.9999	No
30 min vs 35 min	> 0.9999	No

The absence of major variations in electrophysiological activity under these combined conditions demonstrates that the setup operates within a safe range of power and exposure time. A minor difference observed between 20 and 35 minutes

of microwave exposure reached statistical significance ($p = 0.0184$), however, the magnitude of this variation remained within the physiological variability of spontaneous firing rates and is not indicative of a systematic effect. The result is therefore interpreted as a random fluctuation rather than a true alteration of network activity. This finding also confirms that potential heating induced by either laser or microwave irradiation remains below the detection threshold of the neurons, consistent with the minimal thermal load expected for these optical and electromagnetic parameters. Such stability is particularly relevant for subsequent thermometric applications, as it ensures that temperature changes recorded in ODMR experiments will reflect intrinsic biological or experimental variations rather than artifacts associated with the excitation sources themselves.

These results confirm that the complete configuration is compatible with live-cell measurements and can be employed for simultaneous acquisition of neuronal firing and nanoscale temperature variations without compromising culture viability.

7.1.2.4 DMSO test

Before applying any pharmacological treatments to modulate network activity, we performed control experiments to assess the effect of the solvent used for drug dilution, DMSO. DMSO is commonly used in biological research to dissolve hydrophobic compounds, but if not properly handled, it can introduce cytotoxic effects or alter the thermal environment of the culture.

To evaluate these risks, we performed dedicated thermometric measurements in the absence of cells. In these tests, 100 μL of pure DMSO were directly added to 4 mL of culture medium, and the bath temperature was monitored using a standard thermocouple. As shown in Figure 7.12, this procedure consistently led to a sharp and rapid temperature increase, due to the exothermic reaction between DMSO and water. These results confirmed the necessity of pre-dilution to avoid temperature artifacts in sensitive experiments.

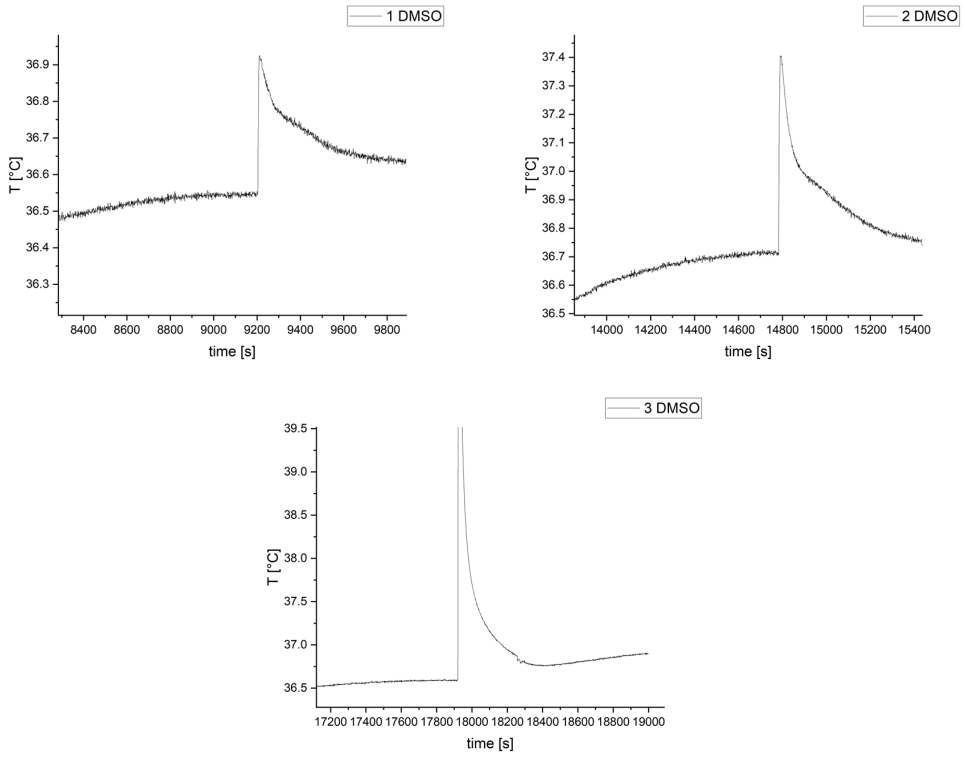

Fig. 7.12 Bath temperature response to DMSO addition recorded with a standard thermocouple. Each panel shows an independent replicate where exothermic mixing of DMSO and water produces a clear temperature increase, confirming that undiluted DMSO addition must be avoided.

In addition to thermal artifacts, DMSO can also compromise cell viability if present in excessive concentrations. Literature and empirical observations indicate that concentrations above 0.1% can interfere with neuronal function. To stay within a safe range, we adopted a dilution protocol that ensures the final DMSO concentration remains at or below 0.1%. Specifically, an intermediate solution was prepared by mixing 100 μL of DMSO with 900 μL of culture medium, creating a 10% solution. Then, 10 μL of this intermediate were added to the MEA well containing approximately 1 mL of culture medium, reaching the desired 0.1% final concentration (see Fig. 7.13). Importantly, this pre-dilution allows most of the heat generated by the DMSO–water reaction to dissipate in the intermediate step, avoiding any thermal increase in the neuronal chamber.

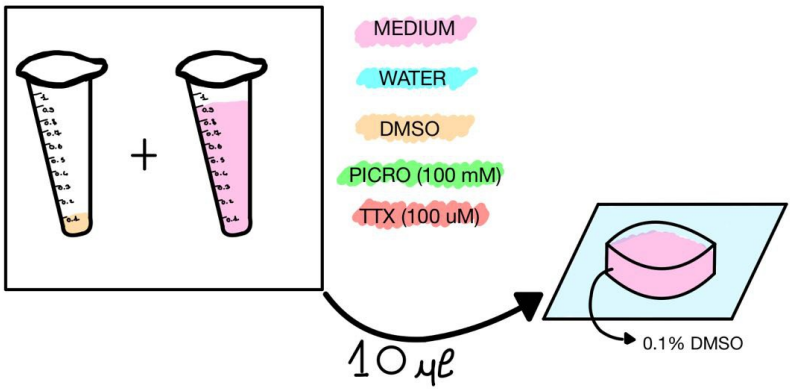

Fig. 7.13 DMSO dilution protocol. The figure outlines the preparation steps used to obtain safe working concentrations for biological experiments.

Follow-up control tests under these diluted conditions, involving simultaneous thermometric and electrophysiological recordings, are currently ongoing. These will be essential to verify that the optimized dilution protocol does not produce any unwanted effects in living neuronal networks, either on temperature or electrical activity.

Once the DMSO protocol has been validated, we plan to apply two pharmacological agents to modulate network excitability: picrotoxin and tetrodotoxin (TTX). These compounds are widely used in neuroscience for their well-characterized, opposing actions on neural signaling.

Picrotoxin protocol. Picrotoxin is a $GABA_A$ receptor antagonist that inhibits inhibitory transmission and increases network excitability. It is not soluble in water at the concentrations required, so it is first prepared as a 100 mM stock in 100% DMSO. From this, an intermediate solution is made by mixing 100 μL of stock with 900 μL of medium, resulting in a 10 mM solution in 10% DMSO. A 10 μL aliquot of this is added to the MEA chamber (1 mL), producing a final concentration of 100 μM picrotoxin and 0.1% DMSO (see Fig. 7.14). This is expected to suppress inhibition and induce a hyperexcitable state in the network.

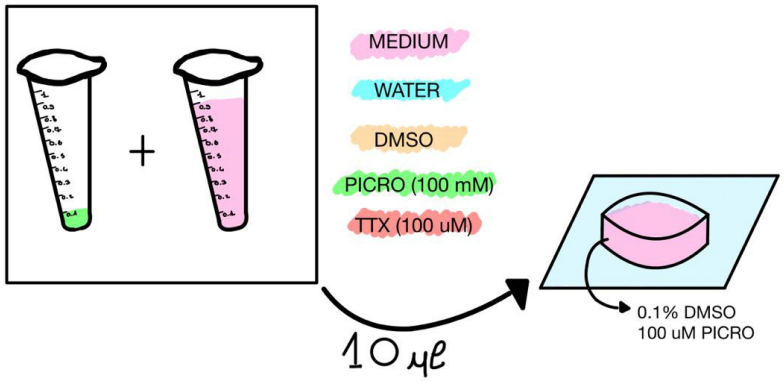

Fig. 7.14 PICRO dilution protocol. The schematic summarizes the dilution process for controlled application in neuronal cultures.

Tetrodotoxin protocol. TTX is a voltage-gated sodium channel blocker that silences neurons by preventing action potentials. It is water-soluble, so a 100 μM stock is diluted with water (300 μL stock + 700 μL water) to make a 30 μM intermediate. From this, 10 μL are added to the MEA chamber, yielding a final concentration of 300 nM TTX (see Fig. 7.15). This is sufficient to block all spiking activity in the culture.

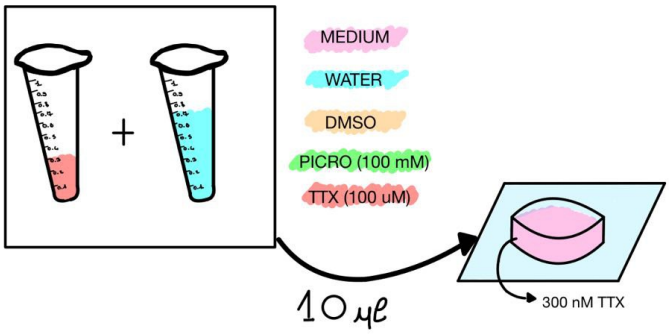

Fig. 7.15 TTX dilution protocol. The figure describes the stepwise preparation used for tetrodotoxin administration in electrophysiological assays.

In summary, the control tests with DMSO established a dilution strategy that avoids thermal and cytotoxic effects. The planned experiments with picrotoxin and TTX will enable us to explore how strong changes in neural excitability are reflected in local temperature dynamics, as recorded by nanodiamond thermometry.

Chapter 8

Experiment – Calibrated detection of mesoscopic photon flux for NV ensemble ODMR

In this chapter I present a collaborative Italian-Czech pilot study on radiometric traceability of NV-based sensing. In this experiment I partecipated to the characterization of a calibrated silicon detector designed and developed by the Czech Metrology Institute (CMI), in a "mesoscopic" photon flux regime (10^7-10^8 photons per second). This regime is of interest for ODMR measurements with dense NV ensembles. The goal is not only to record clear ODMR spectra from small, near-surface NV volumes, but to do so with traceability and linearity, enabling absolute photon-flux estimates and sensitivity budgeting that remain meaningful across different instruments and laboratories.

8.1 Samples and Processing

The diamond sample under analysis was a $3 \times 3 \times 0.3\,\mathrm{mm}^3$ electronic-grade CVD plate (Element Six), specified with < 1 ppm substitutional nitrogen and < 0.05 ppm boron. To create a well-defined sensing layer close to the surface, implantation of $^{14}N^+$ ions at 10 keV with a fluence of $10^{14}\,\mathrm{ions\,cm}^{-2}$ was performed, followed by a 2 h anneal at 950°C. This recipe yields a thin NV-rich region located roughly 10–15 nm below the surface. Under a diffraction-limited green spot of about $1.5\,\mu$m

in diameter, this layer contains on the order of 7×10^5 NV centers. Such an ensemble is small enough to preserve the advantages of a micrometer-scale probe volume, yet large enough to generate a photon flux that quickly exceed the SPAD saturation threshold as soon as the optical power is increased from the lowest range.

8.2 Experimental Approach

Setup The measurements were carried out on a confocal microscope optimized for single-emitter sensitivity but adaptable to ensemble work (Fig. 8.1). Excitation at 532 nm (Nd:YAG SHG, Coherent Prometheus 100NE) was focused through an Olympus UPLANFL air objective with NA $= 0.67$. The collected red emission was cleaned using a 532 nm notch and a 650 nm long-pass filter and then divided between two detection arms: one feeding a commercial SPAD, the other feeding the calibrated detector developed by CMI. Microwave control around 2.87 GHz was provided by a Keysight N5183B source and delivered through a planar ring antenna with a bandwidth of approximately 400 MHz, which allowed reliable frequency sweeps without constant retuning.

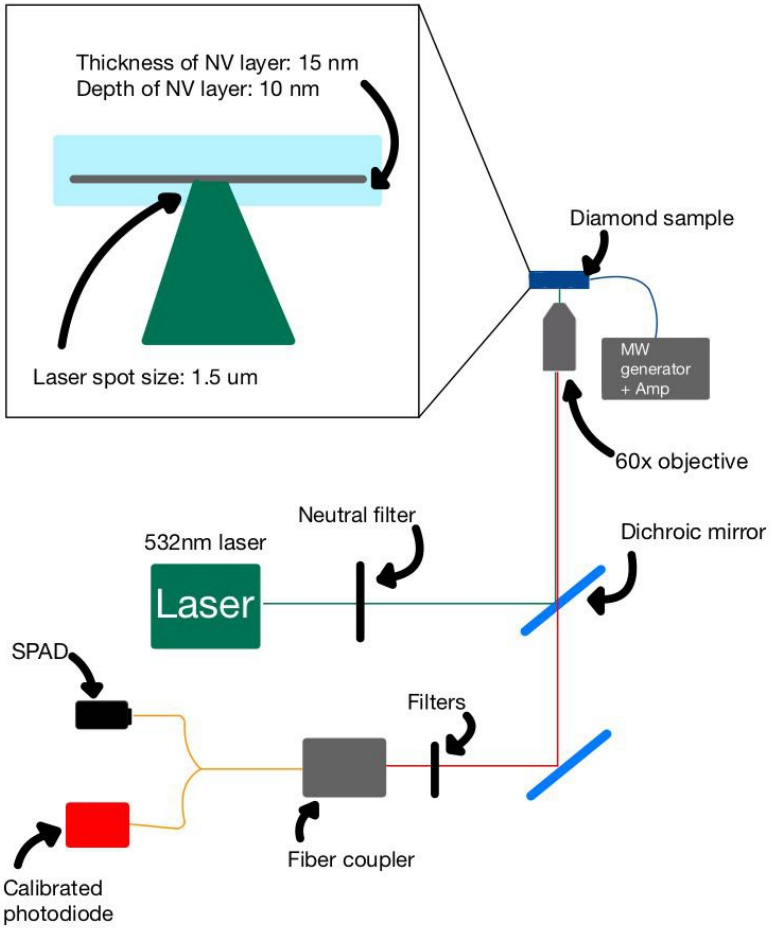

Fig. 8.1 Schematic view of the optical setup used for the measurements. The 532 nm excitation laser is focused through an air objective onto the diamond sample, while the photoluminescence is filtered and equally split between two detection paths. One path feeds a commercial SPAD, and the other a calibrated photodetector designed at the CMI. This configuration enables a direct comparison between detection regimes under identical optical conditions.

Custom calibrated detector design The custom detector, developed at the Czech Metrology Institute, uses a low-noise $3 \times 3\,\mathrm{mm}^2$ Si photodiode (S1227-33BQ) combined with a switched-integrator amplifier (SIA) (Fig. 8.2). The integration time τ can

be tuned from 1 ms up to 1 s, with a fast reset of about 0.1 ms, so that we can choose between faster sampling and deeper integration depending on the optical power and the desired spectral resolution. The feedback capacitance $K = (1.045 \pm 0.003)\,\mathrm{pF}$ was calibrated against a stable voltage source and a $100\,\mathrm{M\Omega}$ standard resistor, ensuring that the conversion from integrated voltage to photocurrent is accurately determined rather than assumed.

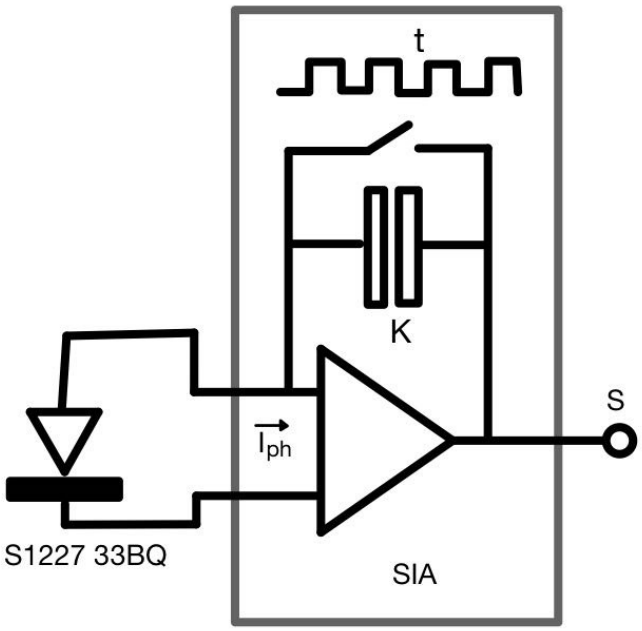

Fig. 8.2 Schematic representation of the calibrated CMI detector. The system consists of a low-noise silicon photodiode connected to a switched-integrator amplifier (SIA). The integration time, controlled by a microprocessor, ranges from 1 ms to 1 s with a minimum reset time of about 0.1 ms. The precisely calibrated feedback capacitance defines the current-to-voltage conversion factor of the device.

The absolute spectral responsivity $R(\lambda)$ of the photodiode was calibrated from 580 to 960 nm in 10 nm steps (Fig. 8.3), traceable to a cryogenic radiometer. By combining the measured responsivity curve $R(\lambda)$ with the actual NV emission spectrum, the detected signal can be expressed as an absolute optical power, traceable to primary standards and directly comparable across different experiments. This eliminates the ambiguity of arbitrary “counts” units typical of non-calibrated photoluminescence measurements.

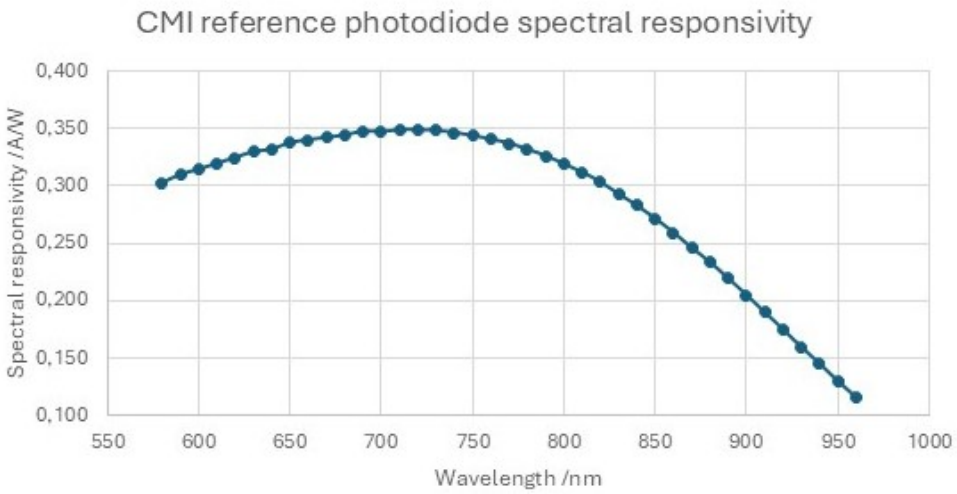

Fig. 8.3 Spectral responsivity $R(\lambda)$ of the calibrated photodiode measured at the Czech Metrology Institute. The calibration, performed in 10 nm steps from 580 nm to 960 nm, is traceable to a cryogenic radiometer, ensuring measurement accuracy. .

The SIA output S (in volts) is proportional to the time-integrated photocurrent. After subtracting the dark offset D we compute

$$I_{\mathrm{ph}} = \frac{(S-D)\,K}{\tau}.$$

To correctly convert this current into optical power, we define an effective responsivity

$$R_{\mathrm{eff}} = \frac{\int S_{\mathrm{NV}}(\lambda)\,R(\lambda)\,d\lambda}{\int S_{\mathrm{NV}}(\lambda)\,d\lambda},$$

where $S_{\mathrm{NV}}(\lambda)$ is the measured NV emission spectrum under our filtering. The optical power is then $P_{\mathrm{opt}} = I_{\mathrm{ph}}/R_{\mathrm{eff}}$. Finally, we estimate the photon flux using the mean photon energy $E_{\mathrm{ph}} = hc/\lambda_{\mathrm{mean}}$ (with λ_{mean} extracted from the same spectrum), so that

$$N = \frac{P_{\mathrm{opt}}}{E_{\mathrm{ph}}}.$$

The key point is the following: because K and $R(\lambda)$ are calibrated, the conversion chain from volts to photons does not rely on hidden assumptions, and the numbers that we report can be compared, audited, and reused for instrument-to-instrument alignment.

Experimental procedure The measurements were planned to gradually test both the performance and the limits of the calibrated detector, while maintaining a direct comparison with a commercial SPAD wherever possible. The procedure started with a characterization of the ensemble photoluminescence as a function of excitation power delivered to the sample. By progressively increasing the optical power, I obtained the saturation curve $I(P)$, from which both the saturation power P_{sat} and the maximum emission rate I_∞ were extracted through a standard two-level fit. This preliminary step was important not only to quantify the brightness of the ensemble, but also to identify the range where the PL remains linear with excitation, ensuring that subsequent ODMR measurements would not be affected by optical saturation.

Once this calibration step was completed, I acquired ODMR spectra at three representative excitation powers, corresponding to the low, intermediate, and high regimes of the detector response. Both the SPAD and the calibrated detector were used simultaneously, with the photoluminescence signal split equally between them, so that the comparison would not depend on external variations. For each condition, the ODMR contrast and linewidth were extracted from Lorentzian fits.

To quantify temperature sensitivity, I applied the differential approach described in Sec. 3.2.2 and computed the sensitivity according to the following expression:

$$S_{\Delta T} = \frac{\sqrt{2}\,\sigma_c}{\gamma_T\, m}\sqrt{\tau} \tag{8.1}$$

where m represents the slope of the linear region in the differential spectrum, σ_c is the standard deviation of the detected counts, and γ_T is the temperature coefficient of the NV resonance ($\gamma_T \simeq -75\,\text{kHz/K}$ at room temperature). The statistical uncertainty σ_c was determined directly from the time traces of each detector, recorded for a total acquisition time of 11 s, with a sampling interval of 18 ms for the SPAD and 200 ms for the calibrated detector.

This procedure provides an empirical and realistic estimation of the temperature sensitivity, reflecting the actual performance of each detection chain under identical experimental conditions.

8.3 Results and Discussion

Photoluminescence and saturation behavior. The photoluminescence intensity as a function of excitation power followed the expected saturation trend, described by eq. 2.8 (Fig. 8.4).

Across the explored range of excitation powers, the emission proved stable, with no signs of nonlinear effects or distortions, allowing the ODMR measurements to be analyzed with confidence

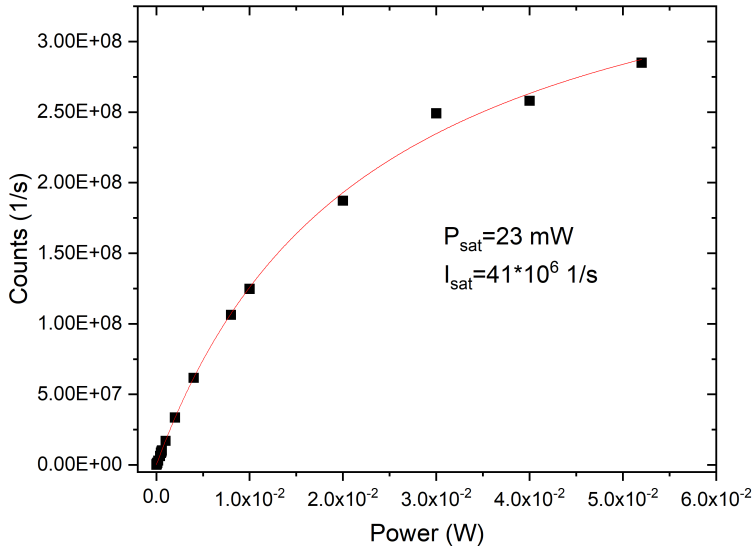

Fig. 8.4 Photoluminescence saturation curve of the NV ensemble. The measured counts (black dots) are fitted with the empirical model following eq. 2.8 (red line). The extracted parameters provide the characteristic saturation power and maximum emission rate of the ensemble.

ODMR performance and comparison between detectors Figure 8.5 compares the ODMR spectra acquired with the calibrated CMI detector and with the commercial SPAD at different excitation powers. At low optical power (25 μW) and correspondingly low photoluminescence levels, the SPAD showed a cleaner and less noisy signal than the CMI detector, as expected from its internal gain and shorter sampling time. At intermediate powers, around 400 μW, both detectors provided consistent and stable data, with similar linewidth and contrast. When the excitation

was increased to 4 mW, the SPAD exceeded its saturation limit and the detected signal dropped to zero, while the calibrated detector continued to operate linearly, delivering well-defined ODMR spectra. This behaviour highlights the complementary working ranges of the two devices: the SPAD performs best at low photon fluxes, whereas the calibrated detector enables quantitative readout at higher emission levels, in the so-called mesoscopic regime. The systematic factor of about two between the count rates of the two detectors can be attributed to the lower detection efficiency of the SPAD at the NV emission wavelengths.

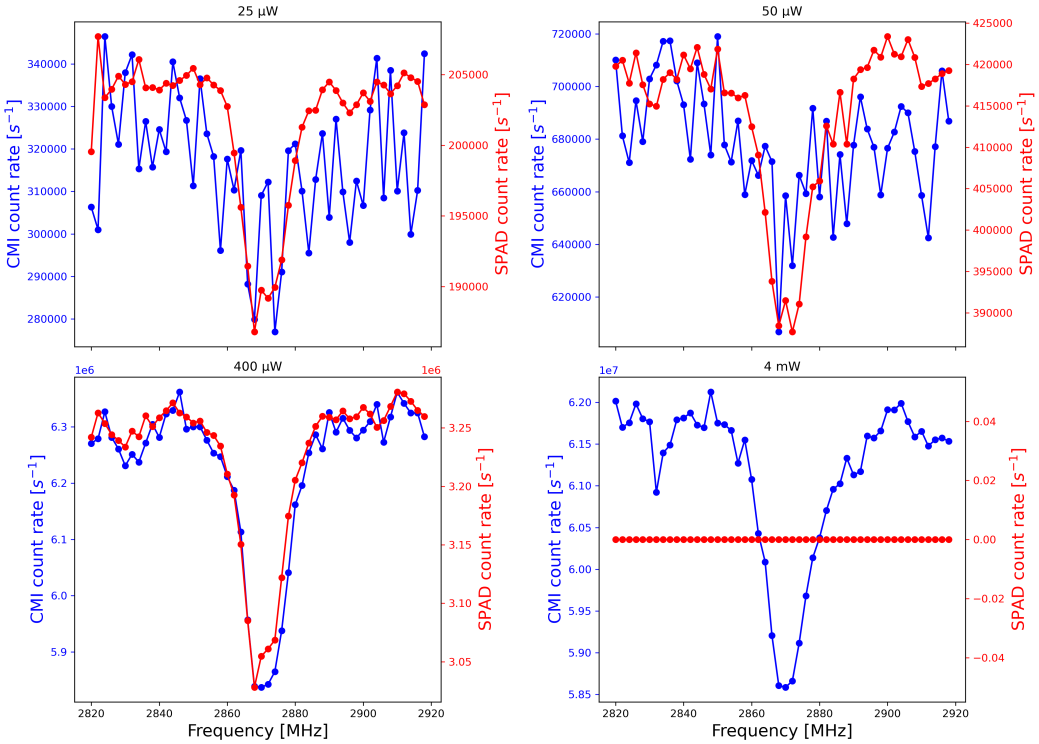

Fig. 8.5 ODMR spectra acquired with the calibrated CMI detector (black squares) and the commercial SPAD (red squares) at increasing optical powers. The comparison shows that while the SPAD signal saturates at high power, the calibrated detector remains linear, maintaining clear ODMR contrast.

Uncertainty, slope extraction, and temperature sensitivity. For each optical power, the slope m of the differential spectrum and the statistical uncertainty σ_c were combined to estimate the temperature sensitivity $S_{\Delta T}$ according to eq. 8.1 (Table 8.1). For the calibrated detector, sensitivity improves significantly from low to intermediate powers, thanks to the increase in photon flux while the noise remains

nearly constant. Beyond 4 mW, the improvement saturates as the contrast decreases slightly and the linewidth broadens. The SPAD performs best at very low power, but quickly becomes unusable once the optical flux exceeds its saturation threshold (see Fig. 8.6).

Table 8.1 Comparison of estimated temperature sensitivities for the SPAD and the calibrated detector at different excitation powers. The table reports values derived using Equation 8.1 with $\tau = 11$ s and $\gamma_T = -75$ kHz/K, summarizing the performance difference between the two detection systems.

Detector	**Power (mW)**	**Slope m (mcounts)**	**Sensitivity $S_{\Delta T}$ (K/$\sqrt{\text{Hz}}$)**
SPAD	0.4	40	0.9
SPAD	4	–	Saturated
CMI detector	0.4	89	21.3
CMI detector	4	785	2.4
CMI detector	40	1329	2.4

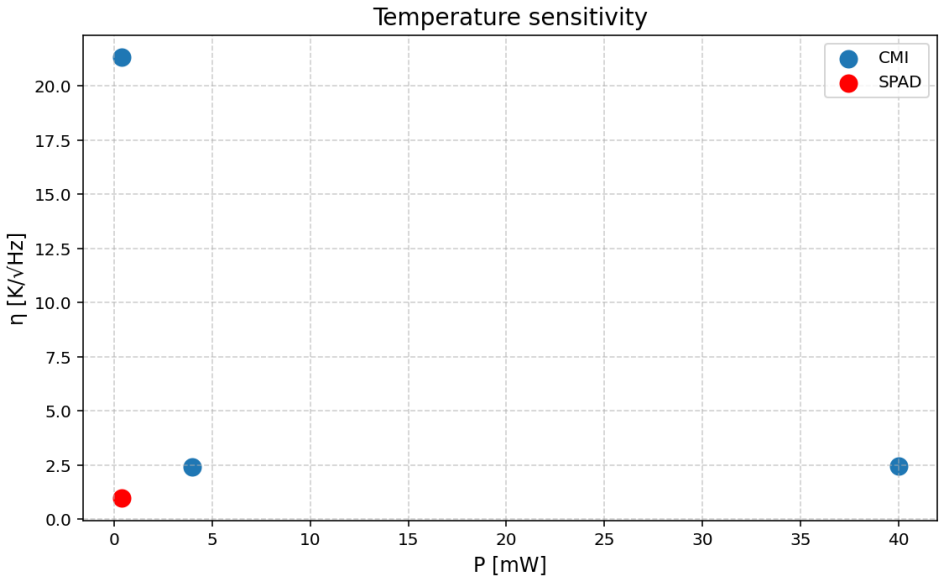

Fig. 8.6 Temperature sensitivity as a function of optical power for the SPAD (red) and the calibrated detector (blue). The plot demonstrates that the SPAD offers better sensitivity at low flux, whereas the calibrated detector preserves stable performance across a wider power range, extending the dynamic range of the experiment.

8.4 Conclusion

This study shows that a calibrated silicon photodetector can fill an important gap in NV ensemble experiments. The detector keeps a linear and stable response in a range of photon flux where SPADs start to saturate, and at the same time it provides absolute measurements of optical power and photon count. The ability to convert voltage signals into traceable photon numbers adds a clear metrological advantage to ODMR sensing, changing what is often a qualitative measurement into one that is quantitative and reliable.

This is particularly relevant in the intermediate photon regime, which is common in NV ensemble measurements. In this range, traditional single-photon detectors cannot be used due to saturation, while standard photodiodes do not offer sufficient sensitivity. The calibrated detector successfully operates in this middle regime, offering a reliable tool to cover experimental conditions that are otherwise difficult to quantify.

The metrological impact of this approach is significant. Having a calibrated, traceable detector means that measurement results can be compared across different laboratories and experimental setups with increased confidence. It also supports the development of reference protocols for quantum sensing, improving reproducibility and long-term consistency. This is an essential requirement for moving quantum technologies toward industrial and commercial applications.

Even though SPADs are still the best choice for very low light levels, the calibrated photodetector works well in a different range where higher optical powers can be used to improve signal-to-noise ratio without losing accuracy. This makes it particularly suitable for experiments involving NV ensembles or other color center systems, where the total fluorescence signal is stronger than that of a single emitter but still requires careful calibration.

In conclusion, the tested detector offers not only strong performance in terms of sensitivity and linearity, but also adds a new level of confidence to optical readouts in quantum sensing experiments. It supports the future development of quantum sensors that can be used not only for research, but also in practical applications where reliable and reproducible measurements are required.

As the field of quantum sensing continues to grow, tools like this will be essential to close the gap between experimental science and real-world implementation.

The integration of traceable optical detection is therefore a key step toward the metrological standardization of quantum technologies.

Chapter 9

Conclusions and Outlook

This thesis presented an extended study on diamond color centers, focusing on their fabrication, optical properties, and implementation in experimental setups aimed at applications in quantum technologies and life sciences. The work was organized around four main experimental directions: (i) the surface processing of nanodiamonds to achieve sub–20 nm dimensions while preserving thermal sensitivity, (ii) the engineering and optical optimization of GeV centers in bulk diamond, (iii) the development of a platform for intracellular thermometry in neurons using NV centers in nanodiamonds combined with multielecrode array for neuronal firing readout, and (iv) the characterization of a custom calibrated photodetector. These activities were described in Chapters 6, 7 and 8.

Together, these investigations demonstrate how diamond color centers can be applied to different research domains, ranging from photonics to biology, providing solid and versatile tools for quantum sensing, bioimaging, and traceable measurements.

Chapter 6 explored two key developments. The first addressed the challenge of producing nanodiamonds below 20 nm in size, a critical range for cellular internalization. However, particles of this dimensions often suffer from surface-related defects that reduce ODMR contrast and sensitivity. Through controlled thermal oxidation and ion implantation, we obtained nanodiamonds that remained stable and functional, keeping ODMR sensitivity even at smaller dimensions. These results are particularly relevant for the development of highly miniaturized quantum sensors that can operate in demanding biological contexts.

In the same chapter, it is also reported the fabrication of GeV centers in bulk diamond through ion implantation and thermal post-processing. In particular, we compared two different annealing strategies: conventional high-temperature annealing in vacuum and HPHT annealing. My contribution involved the optical characterization of single GeV emitters, including the analysis of their saturation behavior and fluorescence lifetime. One of the main findings was that HPHT treatment improves emitter brightness and reduces the required excitation power, suggesting this approach is promising for all-optical thermometry in biological environments.

Chapter 7 described the application of NV-based thermometry to living systems. My main contribution was the design, construction, and validation of a hybrid experimental platform combining optical and electrical recordings. This setup, based on a confocal microscope integrated with a multi-electrode array, enable the simultaneous acquisition of temperature signals and neuronal activity.

A crucial step in this work was ensuring that the experimental conditions, specifically, laser illumination, microwave excitation, and nanodiamond incubation, were compatible with neuronal viability. I performed a set of viability tests that confirmed that none of these elements, either individually or in combination, affected the spontaneous firing of the neuronal network. This step was essential to validate the reliability of thermometric measurements in live biological environments.

To interpret temperature changes with high accuracy, I adopted an alternative calibration method based on spectral correlation analysis. This approach tracks the overall shift in the ODMR spectrum, rather than analyzing only individual resonances. It was compared to the traditional method based on fitting the linear regions of the differential spectrum. The results showed that both techniques produce consistent results, allowing flexibility in future data analysis depending on the experimental context.

Importantly, this platform enables the observation of physiologically relevant temperature variations with high spatial and temporal resolution. The ability to correlate temperature with real-time neuronal activity opens new possibilities in neuroscience, allowing better insight of temperature dynamics in biological system at the single cell level .

Chapter 8 reports on a collaborative study with the Czech Metrology Institute, where we evaluated a calibrated, low-noise photodiode detector for optical powers in the intermediate regime. This region, typical for NV ensembles, falls in a power

range which is above the saturation threshold of SPAD and below analog photodiodes sensitivity. The tested detector offered high linearity, traceable responsivity, and low noise in the nW–μW range. I tested the performance of this detector and compared to that of standard SPADs in the particular instance of ODMR thermometry. The results confirmed the detector's suitability for quantum sensing experiments in the mesoscopic regime, leading to a calibrated and traceable light detection.

Each of the activities presented in this thesis involved different technical challenges. These ranged from optimizing the optical alignment of the confocal system, to dealing with biological constraints for cell survival. Among these, one of the most demanding aspects was working with living neuronal samples, where variability from sample to sample often led to complex and not immediately interpretable results. Ensuring neuronal viability while performing simultaneous optical and electrical measurements required careful control of laser illumination, microwave excitation, and nanodiamond incubation. These challenges highlight the need for extensive statistical analysis to reliably interpret the observed phenomena, a requirement that will remain important in future studies.

Among all contributions, the implementation of a synchronized optical and electrical readout platform represents a major achievement. It enables the study of thermal and electrophysiological dynamics in parallel, providing a robust framework for future research in cellular thermodynamics.

Looking ahead, several research directions can be pursued. In biological applications, the platform developed in this thesis could be extended to target specific organelles using functionalized nanodiamonds, or adapted to other cell types and tissues. The thermometric method could be applied to study fast or transient events in living cells.

Regarding GeV centers, future efforts may focus on their spin properties and the feasibility of all-optical readout in ambient conditions. On the materials side, further surface treatments and irradiation protocols could help improve brightness and spin coherence in ultra-small nanodiamonds. Finally, the use of calibrated detectors like the one tested here could contribute to the development of traceable quantum thermometry systems, bridging the gap between basic research and metrology.

In conclusion, this thesis contributes to the growing field of diamond-based sensing and photonics. It demonstrates how color centers in diamond can be engineered and applied in complex environments, from solid-state platforms to living

systems, while maintaining performance and measurement reliability. The methods and technologies developed during this work offer a flexible and robust toolkit for exploring new questions in both quantum science and life sciences.

Bibliography

[1] Michael Ströck. Eight allotropes of carbon. https://commons.wikimedia.org/wiki/File:Eight_Allotropes_of_Carbon.png, 2006.

[2] Mariusz Sapinski. Model of carbon wire heating in accelerator beam.

[3] Alberto Carrasco-Casado, Veronica Marmol, and Natalia Denisenko. *Free-Space Quantum Key Distribution*, pages 589–607. 08 2016.

[4] Linh Pham, David Le Sage, A. Stacey, M. Markham, Daniel Twitchen, and M. Lukin. Enhanced metrology using preferential orientation of nitrogen-vacancy centers in diamond. *Physical Review B*, 86, 07 2012.

[5] Andreas Brenneis, Louis Gaudreau, Max Seifert, H. Karl, M. Brandt, Hans Huebl, Jose Garrido, Frank Koppens, and Alexander Holleitner. Ultrafast electronic read-out of diamond nv centers coupled to graphene. 08 2014.

[6] Anna Galler and Patrik Thunström. Orbital and electronic entanglement in quantum teleportation schemes. *Physical Review Research*, 3, 08 2021.

[7] Giulia Petrini, Ekaterina Moreva, Ettore Bernardi, Paolo Traina, Giulia Tomagra, Valentina Carabelli, Ivo Pietro Degiovanni, and Marco Genovese. Is a quantum biosensing revolution approaching? perspectives in nv-assisted current and thermal biosensing in living cells. *Advanced Quantum Technologies*, 3(12):2000066, 2020.

[8] Giulia Petrini, Giulia Tomagra, Ettore Bernardi, Ekaterina Moreva, Paolo Traina, Andrea Marcantoni, Federico Picollo, Klaudia Kvaková, Petr Cígler, Ivo Pietro Degiovanni, et al. Nanodiamond–quantum sensors reveal temperature variation associated to hippocampal neurons firing. *Advanced Science*, 9(28):2202014, 2022.

[9] Gábor Kucsko, Peter C. Maurer, Norman Y. Yao, Masashi Kubo, Heung-Ryoul Noh, Patrick K. Lo, Hongkun Park, and Mikhail D. Lukin. Nanometre-scale thermometry in a living cell. *Nature*, 500:54–58, 2013.

[10] Liming Dai. *Carbon Materials: Science and Applications*. CRC Press, Boca Raton, 2006.

[11] Marcus W Doherty, Neil B Manson, Paul Delaney, Fedor Jelezko, Jörg Wrachtrup, and Lloyd CL Hollenberg. The nitrogen-vacancy colour centre in diamond. *Physics Reports*, 528(1):1–45, 2013.

[12] Carlo Bradac, Weibo Gao, Jacopo Forneris, Matthew E. Trusheim, and Igor Aharonovich. Quantum nanophotonics with group iv defects in diamond. *Nature Communications*, 10(1):5625, 2019.

[13] Zhiping Ju, Junjie Lin, Si Shen, Botao Wu, and E Wu. Preparations and applications of single color centers in diamond. *Advances in Physics: X*, 6(1):1858721, 2021.

[14] Fedor Jelezko and Jörg Wrachtrup. Single defect centres in diamond: A review. *physica status solidi (a)*, 203(13):3207–3225, 2006.

[15] Alp Sipahigil, Ruffin E Evans, Denis D Sukachev, Michael J Burek, Johannes Borregaard, Mihir K Bhaskar, Christian T Nguyen, Jose L Pacheco, Haig A Atikian, Charles Meuwly, et al. An integrated diamond nanophotonics platform for quantum-optical networks. *Science*, 354(6314):847–850, 2016.

[16] Jacopo Forneris, Daniela Gatto Monticone, Paolo Traina, Vladimir Grilj, Giorgio Brida, Giacomo Amato, Luisa Boarino, Emanuela Enrico, Ivo Pietro Degiovanni, Ekaterina Moreva, Nebojša Skukan, Miodrag Jakšić, Marco Genovese, and Paolo Olivero. Electrical stimulation of non-classical photon emission from diamond color centers by means of sub-superficial graphitic electrodes. *Scientific Reports*, 5:15901, 2015.

[17] R. Hanbury Brown and R. Q. Twiss. Correlation between photons in two coherent beams of light. *Nature*, 177:27–29, 1956.

[18] P. Grangier, G. Roger, and A. Aspect. Experimental evidence for a photon anticorrelation effect on a beam splitter: A new light on single-photon interferences. *Europhysics Letters (EPL)*, 1(4):173–179, Feb 1986.

[19] Ulrika F. S. D'Haenens-Johansson, James E. Butler, and Andrey N. Katrusha. Synthesis of diamonds and their identification. *Reviews in Mineralogy and Geochemistry*, 88(1):689–753, 07 2022.

[20] Karl Schmetzer. High pressure high temperature treatment of diamonds—a review of the patent literature from five decades (1960-2009). *Journal of Gemmology*, 32(1):52, 2010.

[21] Olga A Shenderova, Alexander I Shames, Nicholas A Nunn, Marco D Torelli, Igor Vlasov, and Alexander Zaitsev. Synthesis, properties, and applications of fluorescent diamond particles. *Journal of Vacuum Science & Technology B*, 37(3), 2019.

[22] Qi Liang, Chih-shiue Yan, Yufei Meng, Joseph Lai, Szczesny Krasnicki, Hokwang Mao, and Russell J Hemley. Recent advances in high-growth rate single-crystal cvd diamond. *Diamond and Related Materials*, 18(5-8):698–703, 2009.

[23] RS Balmer, JR Brandon, SL Clewes, HK Dhillon, JM Dodson, I Friel, PN Inglis, TD Madgwick, ML Markham, TP Mollart, et al. Chemical vapour deposition synthetic diamond: materials, technology and applications. *Journal of Physics: Condensed Matter*, 21(36):364221, 2009.

[24] Christopher M Breeding and James E Shigley. The "type" classification system of diamonds and its importance in gemology. *Gems Gemol*, 45(2):96–111, 2009.

[25] Yinhang Zhang, Kyong Yop Rhee, David Hui, and Soo-Jin Park. A critical review of nanodiamond based nanocomposites: Synthesis, properties and applications. *Composites Part B: Engineering*, 143:19–27, 2018.

[26] Lin Lai and Amanda S Barnard. Functionalized nanodiamonds for biological and medical applications. *Journal of nanoscience and nanotechnology*, 15(2):989–999, 2015.

[27] Helena S Knowles, Dhiren M Kara, and Mete Atatüre. Observing bulk diamond spin coherence in high-purity nanodiamonds. *Nature materials*, 13(1):21–25, 2014.

[28] Jean-Paul Boudou, Patrick A Curmi, Fedor Jelezko, Joerg Wrachtrup, Pascal Aubert, Mohamed Sennour, Gopalakrischnan Balasubramanian, Rolf Reuter, Alain Thorel, and Eric Gaffet. High yield fabrication of fluorescent nanodiamonds. *Nanotechnology*, 20(23):235602, 2009.

[29] Valerii Yu Dolmatov. Detonation-synthesis nanodiamonds: synthesis, structure, properties and applications. *Russian Chemical Reviews*, 76(4):339, 2007.

[30] Anke Krueger, Jochen Stegk, Yuejiang Liang, Li Lu, and Gerald Jarre. Biotinylated nanodiamond: simple and efficient functionalization of detonation diamond. *Langmuir*, 24(8):4200–4204, 2008.

[31] Christophe Couteau. Spontaneous parametric down-conversion. *Contemporary Physics*, 59(3):291–304, 2018.

[32] Marcus W. Doherty, Chunhui Rita Du, and Gregory D. Fuchs. Quantum science and technology based on color centers with accessible spin. *Journal of Applied Physics*, 131(1):010401, 01 2022.

[33] Victor Acosta and Philip Hemmer. Nitrogen-vacancy centers: Physics and applications. *MRS bulletin*, 38(2):127–130, 2013.

[34] A Gruber, A Drabenstedt, C Tietz, L Fleury, Joerg Wrachtrup, and C von Borczyskowski. Scanning confocal optical microscopy and magnetic resonance on single defect centers. *Science*, 276(5321):2012–2014, 1997.

[35] David D. Awschalom, Ronald Hanson, Jörg Wrachtrup, and Brian B. Zhou. Quantum technologies with optically interfaced solid-state spins. *Nature Photonics*, 12:516–527, 2018.

[36] Gary Wolfowicz, F. Joseph Heremans, Christopher P. Anderson, Shinobu Kanai, Hosung Seo, Adam Gali, Giulia Galli, and David D. Awschalom. Quantum guidelines for solid-state spin defects. *Nature Reviews Materials*, 6:906–925, 2021.

[37] Andreas Reiserer, Norbert Kalb, Gerhard Rempe, and Stephan Ritter. A quantum gate between a flying optical photon and a single trapped atom. *Nature*, 508(7495):237–240, April 2014.

[38] V. M. Schäfer, C. J. Ballance, K. Thirumalai, L. J. Stephenson, T. G. Ballance, A. M. Steane, and D. M. Lucas. Fast quantum logic gates with trapped-ion qubits. *Nature*, 555(7694):75–78, March 2018.

[39] Pieter Kok, W. J. Munro, Kae Nemoto, T. C. Ralph, Jonathan P. Dowling, and G. J. Milburn. Linear optical quantum computing with photonic qubits. *Rev. Mod. Phys.*, 79:135–174, Jan 2007.

[40] Jarryd J Pla, Kuan Y Tan, Juan P Dehollain, Wee H Lim, John JL Morton, Floris A Zwanenburg, David N Jamieson, Andrew S Dzurak, and Andrea Morello. High-fidelity readout and control of a nuclear spin qubit in silicon. *Nature*, 496(7445):334–338, 2013.

[41] Michel H Devoret and John M Martinis. Implementing qubits with superconducting integrated circuits. *Quantum Information Processing*, 3(1):163–203, 2004.

[42] Björn Trauzettel, Denis V Bulaev, Daniel Loss, and Guido Burkard. Spin qubits in graphene quantum dots. *Nature Physics*, 3(3):192–196, 2007.

[43] Viktor Ivády, Igor A Abrikosov, and Adam Gali. First principles calculation of spin-related quantities for point defect qubit research. *npj Computational Materials*, 4(1):76, 2018.

[44] David P. DiVincenzo. The physical implementation of quantum computation. *Fortschritte der Physik*, 48(9-11):771–783, 2000.

[45] Tim H. Taminiau, Jeroen Cramer, Toeno van der Sar, Viacheslav V. Dobrovitski, and Ronald Hanson. Universal control and error correction in multi-qubit spin registers in diamond. *Nature Nanotechnology*, 9:171–176, 2014.

[46] Lilian Childress and Ronald Hanson. Diamond nv centers for quantum computing and quantum networks. *MRS Bulletin*, 38(2):134–138, 2013.

[47] Marcus W. Doherty, Neil B. Manson, Paul Delaney, Fedor Jelezko, Jörg Wrachtrup, and Lloyd C. L. Hollenberg. The nitrogen-vacancy colour centre in diamond. *Physics Reports*, 528(1):1–45, 2013.

[48] Peter W Shor and John Preskill. Simple proof of security of the bb84 quantum key distribution protocol. *Physical review letters*, 85(2):441, 2000.

[49] Romana Schirhagl, Kevin Chang, Michael Loretz, and Christian L. Degen. Nitrogen-vacancy centers in diamond: Nanoscale sensors for physics and biology. *Annual Review of Physical Chemistry*, 65:83–105, 2014.

[50] L. Rondin, J.-P. Tetienne, T. Hingant, J.-F. Roch, P. Maletinsky, and V. Jacques. Magnetometry with nitrogen-vacancy defects in diamond. *Reports on Progress in Physics*, 77(5):056503, 2014.

[51] John F. Barry, Jennifer M. Schloss, Erik Bauch, Matthew J. Turner, Connor A. Hart, Linh M. Pham, and Ronald L. Walsworth. Sensitivity optimization for nv-diamond magnetometry. *Reviews of Modern Physics*, 92(1):015004, 2020.

[52] Jason M. Smith, Simon A. Meynell, Ania C. Bleszynski Jayich, and Jan Meijer. Colour centre generation in diamond for quantum technologies. *Nanophotonics*, 8(11):1889–1906, 2019.

[53] L. Rondin, J.-P. Tetienne, T. Hingant, J.-F. Roch, P. Maletinsky, and V. Jacques. Magnetometry with nitrogen-vacancy defects in diamond. *Reports on Progress in Physics*, 77(5):056503, 2014.

[54] David Le Sage, Koji Arai, David R Glenn, Stephen J DeVience, Linh M Pham, Lilah Rahn-Lee, Mikhail D Lukin, Amir Yacoby, Arash Komeili, and Ronald L Walsworth. Optical magnetic imaging of living cells. *Nature*, 496(7446):486–489, 2013.

[55] Erwin Neher and Bert Sakmann. The patch clamp technique. *Scientific American*, 266(3):44–51, 1992.

[56] Richard T Mathias, Ira S Cohen, and Carlos Oliva. Limitations of the whole cell patch clamp technique in the control of intracellular concentrations. *Biophysical journal*, 58(3):759–770, 1990.

[57] Alfred Stett, Ulrich Egert, Elke Guenther, Frank Hofmann, Thomas Meyer, Wilfried Nisch, and Hugo Haemmerle. Biological application of microelectrode arrays in drug discovery and basic research. *Analytical and bioanalytical chemistry*, 377(3):486–495, 2003.

[58] Michael Fejtl, Alfred Stett, Wilfried Nisch, Karl-Heinz Boven, and Andreas Möller. On micro-electrode array revival: its development, sophistication of recording, and stimulation. In *Advances in network electrophysiology: using multi-electrode arrays*, pages 24–37. Springer, 2006.

[59] Micha E Spira and Aviad Hai. Multi-electrode array technologies for neuroscience and cardiology. *Nano-Enabled Medical Applications*, pages 567–602, 2020.

[60] Douglas J Bakkum, Urs Frey, Milos Radivojevic, Thomas L Russell, Jan Müller, Michele Fiscella, Hirokazu Takahashi, and Andreas Hierlemann. Tracking axonal action potential propagation on a high-density microelectrode array across hundreds of sites. *Nature communications*, 4(1):2181, 2013.

[61] Milos Radivojevic, David Jäckel, Michael Altermatt, Jan Müller, Vijay Viswam, Andreas Hierlemann, and Douglas J Bakkum. Electrical identification and selective microstimulation of neuronal compartments based on features of extracellular action potentials. *Scientific reports*, 6(1):31332, 2016.

[62] György Buzsáki, Eran Stark, Antal Berényi, Dion Khodagholy, Daryl R Kipke, Euisik Yoon, and Kensall D Wise. Tools for probing local circuits: high-density silicon probes combined with optogenetics. *Neuron*, 86(1):92–105, 2015.

[63] MI Faley, U Poppe, K Urban, DN Paulson, and RL Fagaly. A new generation of the hts multilayer dc-squid magnetometers and gradiometers. In *Journal of physics: conference series*, volume 43, page 1199. IOP Publishing, 2006.

[64] F Baudenbacher, LE Fong, JR Holzer, and M Radparvar. Monolithic low-transition-temperature superconducting magnetometers for high resolution imaging magnetic fields of room temperature samples. *Applied Physics Letters*, 82(20):3487–3489, 2003.

[65] Svenja Knappe, Tilmann H Sander, Olaf Kosch, Frank Wiekhorst, John Kitching, and Lutz Trahms. Cross-validation of microfabricated atomic magnetometers with superconducting quantum interference devices for biomagnetic applications. *Applied Physics Letters*, 97(13), 2010.

[66] MI Faley, U Poppe, K Urban, DN Paulson, and RL Fagaly. A new generation of the hts multilayer dc-squid magnetometers and gradiometers. In *Journal of physics: conference series*, volume 43, page 1199. IOP Publishing, 2006.

[67] F Baudenbacher, LE Fong, JR Holzer, and M Radparvar. Monolithic low-transition-temperature superconducting magnetometers for high resolution imaging magnetic fields of room temperature samples. *Applied Physics Letters*, 82(20):3487–3489, 2003.

[68] Anri Nakajima. Application of single-electron transistor to biomolecule and ion sensors. *Applied Sciences*, 6(4):94, 2016.

[69] Jubayer Jalil, Yong Zhu, Chandima Ekanayake, and Yong Ruan. Sensing of single electrons using micro and nano technologies: a review. *Nanotechnology*, 28(14):142002, 2017.

[70] Linh My Pham, David Le Sage, Paul L Stanwix, Tsun Kwan Yeung, David Glenn, Alexei Trifonov, Paola Cappellaro, Philip R Hemmer, Mikhail D Lukin, Hongkun Park, et al. Magnetic field imaging with nitrogen-vacancy ensembles. *New Journal of Physics*, 13(4):045021, 2011.

[71] Jeronimo R Maze, Paul L Stanwix, James S Hodges, Seungpyo Hong, Jacob M Taylor, Paola Cappellaro, Liang Jiang, MV Gurudev Dutt, Emre Togan, AS Zibrov, et al. Nanoscale magnetic sensing with an individual electronic spin in diamond. *Nature*, 455(7213):644–647, 2008.

[72] CL Degen. Scanning magnetic field microscope with a diamond single-spin sensor. *Applied Physics Letters*, 92(24), 2008.

[73] Torsten Rendler, Jitka Neburkova, Ondrej Zemek, Jan Kotek, Andrea Zappe, Zhiqin Chu, Petr Cigler, and Jörg Wrachtrup. Optical imaging of localized chemical events using programmable diamond quantum nanosensors. *Nature communications*, 8(1):14701, 2017.

[74] Michael L Hines and Nicholas T Carnevale. The neuron simulation environment. *Neural computation*, 9(6):1179–1209, 1997.

[75] Blaise Agüera y Arcas, Adrienne L Fairhall, and William Bialek. Computation in a single neuron: Hodgkin and huxley revisited. *Neural computation*, 15(8):1715–1749, 2003.

[76] Fidel Santamaria and James Bower. *Hodgkin–Huxley Models*, pages 1173–1180. 12 2009.

[77] Matthew N Rasband and James S Trimmer. Developmental clustering of ion channels at and near the node of ranvier. *Developmental biology*, 236(1):5–16, 2001.

[78] Daisuke Sato, Gonzalo Hernández-Hernández, Collin Matsumoto, Sendoa Tajada, Claudia M Moreno, Rose E Dixon, Samantha O'Dwyer, Manuel F Navedo, James S Trimmer, Colleen E Clancy, et al. A stochastic model of ion channel cluster formation in the plasma membrane. *Journal of General Physiology*, 151(9):1116–1134, 2019.

[79] Bokai Zhang, Xi Feng, Hang Yin, Zhenpeng Ge, Yanhuan Wang, Zhiqin Chu, Helena Raabova, Jan Vavra, Petr Cigler, Renbao Liu, et al. Anchored but not internalized: shape dependent endocytosis of nanodiamond. *Scientific reports*, 7(1):46462, 2017.

[80] Mürsel Karadas, Adam M Wojciechowski, Alexander Huck, Nils Ole Dalby, Ulrik Lund Andersen, and Axel Thielscher. Feasibility and resolution limits of opto-magnetic imaging of neural network activity in brain slices using color centers in diamond. *Scientific reports*, 8(1):4503, 2018.

[81] Jasmina Isakovic, Ian Dobbs-Dixon, Dipesh Chaudhury, and Dinko Mitrecic. Modeling of inhomogeneous electromagnetic fields in the nervous system: a novel paradigm in understanding cell interactions, disease etiology and therapy. *Scientific reports*, 8(1):12909, 2018.

[82] LT Hall, GCG Beart, EA Thomas, DA Simpson, LP McGuinness, JH Cole, JH Manton, RE Scholten, Fedor Jelezko, Jörg Wrachtrup, et al. High spatial and temporal resolution wide-field imaging of neuron activity using quantum nv-diamond. *Scientific reports*, 2(1):401, 2012.

[83] Matti Hämäläinen, Riitta Hari, Risto J Ilmoniemi, Jukka Knuutila, and Olli V Lounasmaa. Magnetoencephalography—theory, instrumentation, and applications to noninvasive studies of the working human brain. *Reviews of modern Physics*, 65(2):413, 1993.

[84] Rolf Simon Schoenfeld and Wolfgang Harneit. Real time magnetic field sensing and imaging using a single spin in diamond. *Physical review letters*, 106(3):030802, 2011.

[85] Dmitry Budker and Michael Romalis. Optical magnetometry. *Nature physics*, 3(4):227–234, 2007.

[86] John F Barry, Matthew J Turner, Jennifer M Schloss, David R Glenn, Yuyu Song, Mikhail D Lukin, Hongkun Park, and Ronald L Walsworth. Optical magnetic detection of single-neuron action potentials using quantum defects in diamond. *Proceedings of the National Academy of Sciences*, 113(49):14133–14138, 2016.

[87] Gopalakrishnan Balasubramanian, Philipp Neumann, Daniel Twitchen, Matthew Markham, Roman Kolesov, Norikazu Mizuochi, Junichi Isoya, Jocelyn Achard, Johannes Beck, Julia Tissler, et al. Ultralong spin coherence time in isotopically engineered diamond. *Nature materials*, 8(5):383–387, 2009.

[88] Adam M Wojciechowski, Mürsel Karadas, Christian Osterkamp, Steffen Jankuhn, Jan Meijer, Fedor Jelezko, Alexander Huck, and Ulrik L Andersen. Precision temperature sensing in the presence of magnetic field noise and vice-versa using nitrogen-vacancy centers in diamond. *Applied Physics Letters*, 113(1), 2018.

[89] Jukka Sarvas. Basic mathematical and electromagnetic concepts of the biomagnetic inverse problem. *Physics in Medicine & Biology*, 32(1):11, 1987.

[90] Daniele Gatto Monticone, K Katamadze, Paolo Traina, E Moreva, Jacopo Forneris, Ivano Ruo-Berchera, Paolo Olivero, Ivo Pietro Degiovanni, Giorgio Brida, and M Genovese. Beating the abbe diffraction limit in confocal microscopy via nonclassical photon statistics. *Physical review letters*, 113(14):143602, 2014.

[91] SCOTT M Thompson, LEONA M Masukawa, and DAVID A Prince. Temperature dependence of intrinsic membrane properties and synaptic potentials in hippocampal ca1 neurons in vitro. *The Journal of neuroscience*, 5(3):817, 1985.

[92] Aymar CL de Lichtervelde, J Pedro de Souza, and Martin Z Bazant. Heat of nervous conduction: A thermodynamic framework. *Physical Review E*, 101(2):022406, 2020.

[93] Duan P Chen, Robert S Eisenberg, Joseph W Jerome, and Chi-Wang Shu. Hydrodynamic model of temperature change in open ionic channels. *Biophysical Journal*, 69(6):2304–2322, 1995.

[94] Duan P Chen, Robert S Eisenberg, Joseph W Jerome, and Chi-Wang Shu. Hydrodynamic model of temperature change in open ionic channels. *Biophysical Journal*, 69(6):2304–2322, 1995.

[95] Ezia Guatteo, Kenny KH Chung, Tharushini K Bowala, Giorgio Bernardi, Nicola B Mercuri, and Janusz Lipski. Temperature sensitivity of dopaminergic neurons of the substantia nigra pars compacta: involvement of transient receptor potential channels. *Journal of neurophysiology*, 94(5):3069–3080, 2005.

[96] Soo Ho Kim, Jermim Noh, Min Ku Jeon, Ki Woong Kim, Luke P Lee, and Seong Ihl Woo. Micro-raman thermometry for measuring the temperature distribution inside the microchannel of a polymerase chain reaction chip. *Journal of Micromechanics and Microengineering*, 16(3):526, 2006.

[97] Jui-Ming Yang, Haw Yang, and Liwei Lin. Quantum dot nano thermometers reveal heterogeneous local thermogenesis in living cells. *ACS nano*, 5(6):5067–5071, 2011.

[98] Fiorenzo Vetrone, Rafik Naccache, Alicia Zamarrón, Angeles Juarranz de la Fuente, Francisco Sanz-Rodríguez, Laura Martinez Maestro, Emma Martin Rodriguez, Daniel Jaque, Jose Garcia Sole, and John A Capobianco. Temperature sensing using fluorescent nanothermometers. *ACS nano*, 4(6):3254–3258, 2010.

[99] Jon S Donner, Sebastian A Thompson, Mark P Kreuzer, Guillaume Baffou, and Romain Quidant. Mapping intracellular temperature using green fluorescent protein. *Nano letters*, 12(4):2107–2111, 2012.

[100] Laura Martinez Maestro, Qiming Zhang, Xiangping Li, Daniel Jaque, and Min Gu. Quantum-dot based nanothermometry in optical plasmonic recording media. *Applied Physics Letters*, 105(18), 2014.

[101] Laura Martinez Maestro, Emma Martin Rodriguez, Francisco Sanz Rodríguez, MC Iglesias-de la Cruz, Angeles Juarranz, Fiorenzo Naccache, Rafik and, Daniel Jaque, John A Capobianco, and José García Solé. Cdse quantum dots for two-photon fluorescence thermal imaging. *Nano letters*, 10(12):5109–5115, 2010.

[102] Victor M. Acosta, Erik Bauch, Micah P. Ledbetter, Adam Waxman, Louis-S. Bouchard, and Dmitry Budker. Temperature dependence of the nitrogen-vacancy magnetic resonance in diamond. *Physical Review Letters*, 104(7):070801, 2010.

[103] Yan-Kai Tzeng, Pei-Chang Tsai, Hsiou-Yuan Liu, Oliver Y Chen, Hsiang Hsu, Fu-Goul Yee, Ming-Shien Chang, and Huan-Cheng Chang. Time-resolved luminescence nanothermometry with nitrogen-vacancy centers in nanodiamonds. *Nano letters*, 15(6):3945–3952, 2015.

[104] Ellen C Jensen. Use of fluorescent probes: their effect on cell biology and limitations. *The Anatomical Record: Advances in Integrative Anatomy and Evolutionary Biology*, 295(12):2031–2036, 2012.

[105] Taras Plakhotnik, Marcus W. Doherty, Jared H. Cole, Robert Chapman, and Neil B. Manson. All-optical thermometry and thermal properties of the optically detected spin resonances of the nv– center in nanodiamond. *Nano Letters*, 14(9):4989–4996, 2014. PMID: 25102035.

[106] Taras Plakhotnik, Hamed Aman, and Huan-Cheng Chang. All-optical single-nanoparticle ratiometric thermometry with a noise floor of 0.3 k $hz^{-1/2}$. *Nanotechnology*, 26(24):245501, may 2015.

[107] Min Li, Qi Zhang, Xi Kong, Zhijie Li, Zhiping Yang, Sheng Zhao, Zhuoyang Qin, Fei Kong, Sanyou Chen, Jia Su, Ke Ruan, Fazhan Shi, and Jiangfeng Du. All-optical thermometry monitoring biochemical kinetics with nv centers in diamond. *Advanced Quantum Technologies*, 7(3):2300293, 2024.

[108] Sumin Choi, V. Agafonov, V. Davydov, and Taras Plakhotnik. Ultrasensitive all-optical thermometry using nanodiamonds with a high concentration of silicon-vacancy centers and multiparametric data analysis. *ACS Photonics*, 6, 05 2019.

[109] Weina Liu, Md Noor A. Alam, Yan Liu, Viatcheslav N. Agafonov, Haoyuan Qi, Kaloian Koynov, Valery A. Davydov, Rustem Uzbekov, Ute Kaiser, Theo Lasser, Fedor Jelezko, Anna Ermakova, and Tanja Weil. Silicon-vacancy nanodiamonds as high performance near-infrared emitters for live-cell dual-color imaging and thermometry. *Nano Letters*, 22(7):2881–2888, 2022. PMID: 35289621.

[110] Ilya V. Fedotov, Maxim A. Solotenkov, Matvey S. Pochechuev, Olga I. Ivashkina, Sergei Ya. Kilin, Konstantin V. Anokhin, and Aleksei M. Zheltikov. All-optical brain thermometry in freely moving animals. *ACS Photonics*, 7(12):3353–3360, 2020.

[111] James B. Pawley, editor. *Handbook of Biological Confocal Microscopy*. Springer, New York, 3 edition, 2006.

[112] I. J. Cox, C. J. R. Sheppard, and T. Wilson. Improvement in resolution by nearly confocal microscopy. *Applied Optics*, 21(5):778–781, 1982.

[113] Tony Wilson and Colin J. R. Sheppard. *Theory and Practice of Scanning Optical Microscopy*. Academic Press, London, 1984.

[114] Multi Channel Systems MCS GmbH. *MEA2100-System User Manual*. Multi Channel Systems, 2022. Publication date: July 14, 2022.

[115] M. E. J. Obien, K. Deligkaris, T. Bullmann, D. J. Bakkum, and U. Frey. Revealing neuronal function through microelectrode array recordings. *Frontiers in Neuroscience*, 8:423, 2015.

[116] Pietro Aprà, Gabriele Zanelli, Elena Losero, Nour-Hanne Amine, Greta Andrini, Mario Barozzi, Ettore Bernardi, Adam Britel, Roberto Canteri, Ivo Pietro Degiovanni, et al. Effects of thermal oxidation and proton irradiation on optically detected magnetic resonance sensitivity in sub-100 nm nanodiamonds. *ACS Applied Materials & Interfaces*, 17(14):21589–21600, 2025.

[117] Elena Nieto Hernández, Elisa Redolfi, Claudia Stella, Greta Andrini, Emilio Corte, Selene Sachero, Sviatoslav Ditalia Tchernij, Fabio Picariello, Tobias Herzig, Yuri M Borzdov, et al. Efficiency optimization of ge-v quantum emitters in single-crystal diamond upon ion implantation and hpht annealing. *Adv Quantum Technol*, 6(8), 2023.

[118] Mahdi Ghavami, Meisam Rezaei, Reza Ejtehadi, Mina Lotfi, Mohammad A Shokrgozar, Baharak Abd Emamy, Jens Raush, and Morteza Mahmoudi. Physiological temperature has a crucial role in amyloid beta in the absence and presence of hydrophobic and hydrophilic nanoparticles. *ACS chemical neuroscience*, 4(3):375–378, 2013.

[119] M Monti, L Brandt, J Ikomi-Kumm, and H Olsson. Microcalorimetric investigation of cell metabolism in tumour cells from patients with non-hodgkin lymphoma (nhl). *Scandinavian journal of haematology*, 36(4):353–357, 1986.

[120] Claudia Stella, Ekaterina Moreva, Ettore Bernardi, Elena Losero, Paolo Traina, Ivo Pietro Degiovanni, Giulia Tomagra, Valentina Carabelli, Petr Cígler, and Marco Genovese. Characterization of nanodiamond samples for intracellular temperature sensing. *Measurement: Sensors*, page 101650, 2025.

[121] Philip Sedgwick. Pearson's correlation coefficient. *Bmj*, 345, 2012.